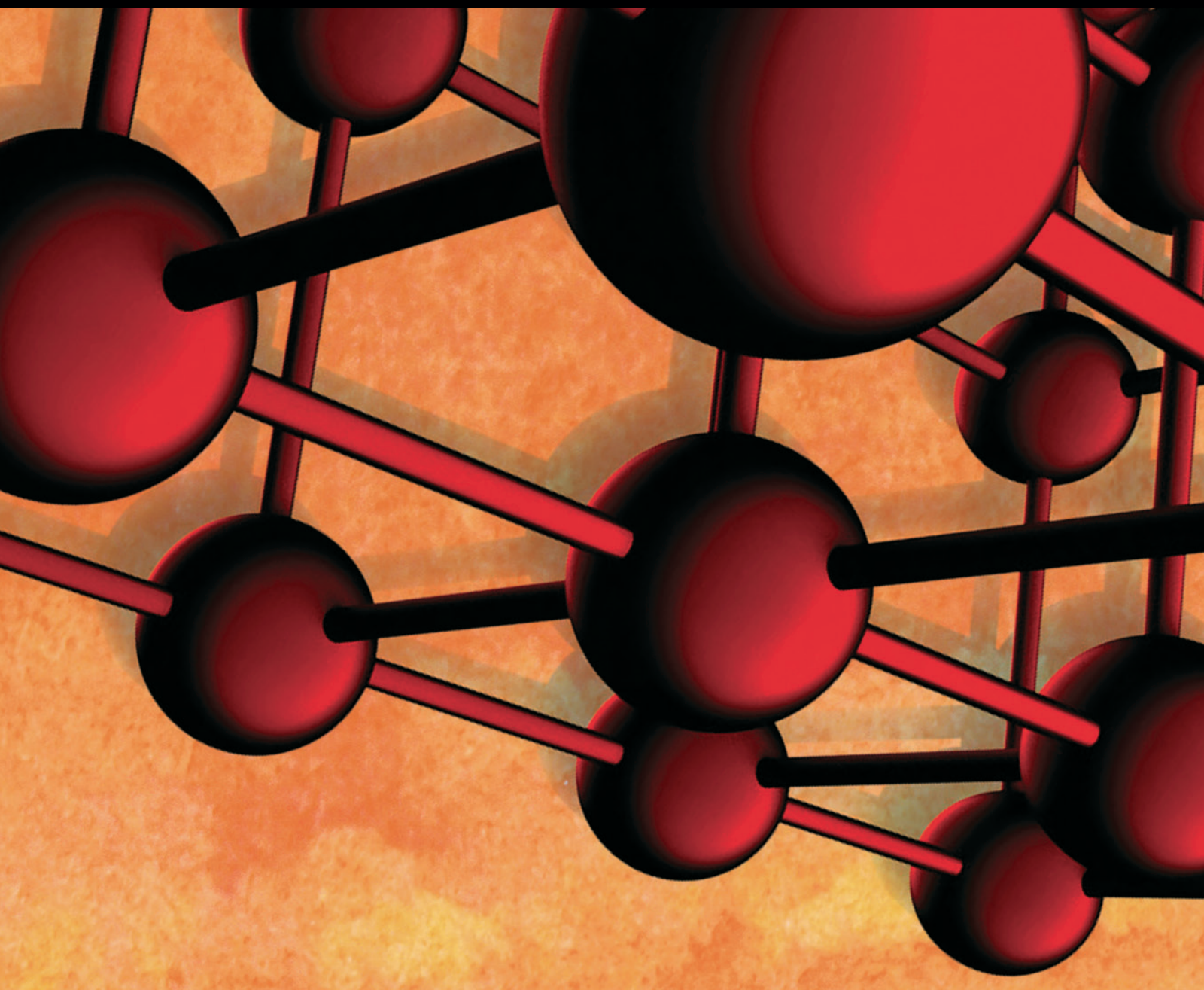


Advances in Materials Science and Engineering

Modern Engineered Materials and Technologies for Metal Forming Applications

Guest Editors: Sutasn Thipprakmas, Man S. Joun, and Lars-Erik Lindgren





Modern Engineered Materials and Technologies for Metal Forming Applications

Advances in Materials Science and Engineering

Modern Engineered Materials and Technologies for Metal Forming Applications

Guest Editors: Sutasn Thipprakmas, Man S. Joun,
and Lars-Erik Lindgren



Copyright © 2017 Hindawi Publishing Corporation. All rights reserved.

This is a special issue published in “Advances in Materials Science and Engineering.” All articles are open access articles distributed under the Creative Commons Attribution License, which permits unrestricted use, distribution, and reproduction in any medium, provided the original work is properly cited.

Editorial Board

Michael Aizenshtein, Israel
Jarir Aktaa, Germany
K. G. Anthymidis, Greece
Santiago Aparicio, Spain
Renal Backov, France
Markus Bambach, Germany
Amit Bandyopadhyay, USA
Massimiliano Barletta, Italy
Mikhael Bechelany, France
Bernd-Arno Behrens, Germany
Avi Bendavid, Australia
Jamal Berakdar, Germany
Jean-Michel Bergheau, France
Giovanni Berselli, Italy
Patrice Berthod, France
Susmita Bose, USA
H.-G. Brokmeier, Germany
Steve Bull, UK
Peter Chang, Canada
Daolun Chen, Canada
Gianluca Cicala, Italy
Gabriel Cuello, France
Narendra B. Dahotre, USA
João P. Davim, Portugal
Angela De Bonis, Italy
Francesco Delogu, Italy
Seshu B. Desu, USA
A. M. Díez-Pascual, Spain
Guru P. Dinda, USA
Yong Ding, USA
N. Tzankova Dintcheva, Italy
Frederic Dumur, France
Kaveh Edalati, Japan
Philip Eisenlohr, USA
Claude Estournès, France
Paolo Ferro, Italy
Massimo Fresta, Italy
G. Garcia-Belmonte, Spain
S. Garcia-Granda, Spain
Carlos Garcia-Mateo, Spain
Daniel Guay, Canada
Gianluca Gubbiotti, Italy

Hiroki Habazaki, Japan
David Holec, Austria
Satoshi Horikoshi, Japan
David Houivet, France
Rui Huang, USA
Michele Iafisco, Italy
Ilia Ivanov, USA
Katsuyuki Kida, Japan
Akihiko Kimura, Japan
Soshu Kirihara, Japan
Hongchao Kou, China
Luciano Lamberti, Italy
Marino Lavorgna, Italy
P. Lejcek, Czech Republic
Cristina Leonelli, Italy
Ying Li, USA
Jun Liu, China
Meilin Liu, Georgia
Yunqi Liu, China
Manuel Lopez-Amo, Spain
F. Lusquiños, Spain
Eric Maire, France
Peter Majewski, Australia
Bobby Kannan Mathan, Australia
Philippe Miele, France
A. E. Miroshnichenko, Australia
Hossein Moayed, Iran
Jose M. Monzo, Spain
Alfonso Muñoz, Spain
Rufino M. Navarro, Spain
Miguel Navarro-Cia, UK
Luigi Nicolais, Italy
Hiroshi Noguchi, Japan
Chérif Nouar, France
Tsutomu Ohzuku, Japan
Olanrewaju Ojo, Canada
Gianfranco Palumbo, Italy
A. Maria Paradowska, Australia
Matthew Peel, UK
Gianluca Percoco, Italy
Claudio Pettinari, Italy
Giorgio Pia, Italy

Candido Fabrizio Pirri, Italy
Simon C. Potter, Canada
Francisca Puertas, Spain
Manijeh Razeghi, USA
Yuri Ribakov, Israel
Anna Richelli, Italy
Antonio Riveiro, Spain
Marco Rossi, Italy
Pascal Roussel, France
Francesco Ruffino, Italy
Antti Salminen, Finland
Paolo Samorì, France
H. A. Santos, Finland
Carlo Santulli, Italy
Fabrizio Sarasini, Italy
Fridon Shubitidze, USA
Donato Sorgente, Italy
Charles C. Sorrell, Australia
Andres Sotelo, Spain
Costas M. Soukoulis, USA
Damien Soulat, France
Antonino Squillace, Italy
Manfred Stamm, Germany
Sam-Shajing Sun, USA
Kohji Tashiro, Japan
Miguel Angel Torres, Spain
Laszlo Toth, France
Achim Trampert, Germany
Luca Valentini, Italy
Hanoeh Daniel Wagner, Israel
Rui Wang, China
Lu Wei, China
Jörg M. K. Wiezorek, USA
Wei Wu, USA
H. S. Yathirajan, India
Wenbin Yi, China
B. F. Yousif, Australia
M. Zappalorto, Italy
Li Zhang, China
Ming-Xing Zhang, Australia
Wei Zhou, China

Contents

Modern Engineered Materials and Technologies for Metal Forming Applications

Sutasn Thipprakmas, Man S. Joun, and Lars-Erik Lindgren

Volume 2017, Article ID 3196509, 2 pages

Numerical and Experimental Research on Cold Compression Deformation Method for Reducing Quenching Residual Stress of 7A85 Aluminum Alloy Thick Block Forging

Cui Jin-dong, Yi You-ping, and Luo Guo-yun

Volume 2017, Article ID 7059389, 6 pages

Development of a Master Sintering Curve for Al-Mg Alloy

Yong-Shin Lee, Sang-Jun Lee, Sangmok Lee, Eung-Zu Kim, and Duck Jae Yoon

Volume 2016, Article ID 5607386, 7 pages

Investigation of Thermostressed State of Coating Formation at Electric Contact Surfacing of “Shaft” Type Parts

Olena V. Berezshnaya, Eduard P. Gribkov, and Valeriy D. Kuznetsov

Volume 2016, Article ID 6597317, 14 pages

Inverse Strategies for Identifying the Parameters of Constitutive Laws of Metal Sheets

P. A. Prates, A. F. G. Pereira, N. A. Sakharova, M. C. Oliveira, and J. V. Fernandes

Volume 2016, Article ID 4152963, 18 pages

Modeling of Flow Stress of 2026 Al Alloy under Hot Compression

Zheng-bing Xiao, Yuan-chun Huang, and Yu Liu

Volume 2016, Article ID 3803472, 8 pages

Editorial

Modern Engineered Materials and Technologies for Metal Forming Applications

Sutasn Thipprakmas,¹ Man S. Joun,² and Lars-Erik Lindgren³

¹*Department of Tool and Materials Engineering, King Mongkut's University of Technology Thonburi, Bangkok 10140, Thailand*

²*School of Mechanical Engineering, Engineering Research Institute, Gyeongsang National University, No. 501, Jinju-daero, Jinju-si, Gyeongsangnam-do, Republic of Korea*

³*Luleå University of Technology, Luleå, Sweden*

Correspondence should be addressed to Sutasn Thipprakmas; sutasn.thi@kmutt.ac.th

Received 7 November 2016; Accepted 7 November 2016

Copyright © 2017 Sutasn Thipprakmas et al. This is an open access article distributed under the Creative Commons Attribution License, which permits unrestricted use, distribution, and reproduction in any medium, provided the original work is properly cited.

During the last decades the development of modern engineered materials and technologies for metal forming applications to new and existing processes, products, and tool represents an emerging issue both from an industry and from an academic viewpoint. Nowadays, a lot of research activities in the field of metal forming have been accomplished and there are a wide range of applications where the modern engineered materials are used.

The objective of this special issue was to provide a wide spectrum of new information on modern engineered materials and technologies for metal forming applications as well as to provide readers with a representative outlook of the latest achievements in this field. The topics focused on the understanding of the interaction between materials of work-piece and the tool as well as the effect of process parameters and so forth when improving efficiency of process, product quality, and tool life.

This special issue offers a selected and articulated overview of the examined topics. It contains five papers and the details were listed as follows.

Z.-b. Xiao et al. revised the constitutive equation of 2026 Al alloy under hot compression which was done by compensation of temperature considering the impact of the second phase on true stress. It indicated that the revised constitutive equation can give an accurate prediction of the peak stress for 2026 Al alloy and can be used in the hot processing of 2026 Al alloy.

Jindong et al. investigated the cold compression deformation method to reduce the quenching residual stress of 7A85 aluminum alloy thick block forging. It was found that this method has a significant effect on reducing stress if an appropriate amount of compression deformation is chosen. The optimal compression deformation value is about 1%-2%, reducing 70% residual stress for 7A85 aluminum alloy specimens sized 100 × 60 × 40 mm.

Y.-S. Lee et al. in their article titled "Development of a Master Sintering Curve for Al-Mg Alloy," to help an engineer to design pressure assisted sintering process for Al-Mg alloy, developed the master sintering curve for Al-Mg alloy which was investigated for suitable design of pressing pressure for this Al-Mg alloy.

O. V. Berezshnaya et al. investigated the thermostressed state of coating formation at electric contact surfacing of "shaft" type parts. It showed that, owing to the increases in friction coefficient, the change of the speed asymmetry factor has a significant influence on the forming of the coating. The nomograms for determination of the stress on the roller-electrode are illustrated, as well as the finite thickness of the coating as the function of the initial thickness of the compact material and the deformation degree are shown.

P. A. Prates et al. in their article titled "Inverse Strategies for Identifying the Parameters of Constitutive Laws of Metal Sheets" showed a great development of inverse strategies coupled with finite element simulations, namely, in FEMU

strategies for the identification of parameters of constitutive laws describing the plastic behavior of metal sheets. These strategies should be directed towards the simultaneous identification of parameters of any constitutive law, including isotropic and kinematic hardening, and any anisotropic yield criterion.

Acknowledgments

The guest editors hope the information provided in this special issue is useful and offers stimulation to the new development of modern engineered materials and technologies for metal forming applications. Finally, we would like to thank the authors for an excellent contribution of their research works and we also very warmly acknowledged the reviewers for an excellent contribution of their valuable review results.

Sutasn Thipprakmas
Man S. Joun
Lars-Erik Lindgren

Research Article

Numerical and Experimental Research on Cold Compression Deformation Method for Reducing Quenching Residual Stress of 7A85 Aluminum Alloy Thick Block Forging

Cui Jin-dong, Yi You-ping, and Luo Guo-yun

School of Materials Science and Engineering, Central South University, Changsha 410083, China

Correspondence should be addressed to Yi You-ping; ypyp@mail.csu.edu.cn

Received 24 May 2016; Revised 31 July 2016; Accepted 8 March 2017; Published 19 March 2017

Academic Editor: Sutasn Thipprakmas

Copyright © 2017 Cui Jin-dong et al. This is an open access article distributed under the Creative Commons Attribution License, which permits unrestricted use, distribution, and reproduction in any medium, provided the original work is properly cited.

In aeronautical machining industry, the most difficult problem to deal with is the distortion of aviation integral component, one main cause of which is the existence of quenching residual stress of forgings, especially for large-sized ones. Therefore, it is important to study the methods that can reduce the quenching residual stress. In this work, the distribution of quenching residual stress of 7A85 aluminum alloy thick block forging, as well as the effect of cold compression deformation method on reducing quenching residual stress, has been investigated by simulation. The results show that, in length direction of 7A85 aluminum alloy thick block with a large size of 260 (*H*) × 1150 (*W*) × 5300 (*L*) mm, quenching residual stress can be significantly reduced by about 2.5% cold compression deformation along the direction of highness, with residual stress in length direction ranging from −65 MPa to 60 MPa, compared with its counterpart after quenching from −170 MPa to 140 MPa. Then a cold compression experiment was carried out, in which the forging residual stress on the surface was measured by X-ray diffraction device. The experimental results indicate that the optimal compression deformation value is 1%-2%, reducing 70% residual stress for 7A85 aluminum alloy specimens in size of 100 (*L*) × 60 (*W*) × 40 (*H*) mm.

1. Introduction

Aluminum alloys are the primary material for structural components of military aircrafts, helicopters, amphibious warships, and so forth for several decades. This is because of the low specific gravity of aluminum which favors the selection of aluminum alloys in weight-critical applications [1]. 7A85 aluminum alloy developed in China in recent years is a new type of high-strength aluminum alloys, whose performance is similar to 7085 aluminum alloy that has been developed by Alcoa company since 2002. In order to gain high-strength performance, a series of heat treatment processes must be carried out including a severe quenching operation which introduces a very high level of residual stress in these aluminum alloys forgings. Quenching residual stress not only results in unexpected machining distortion, but also increases the possibility of unpredicted fatigue failures and stress corrosion cracks (SCC) [2, 3]. Therefore, it is of

great significance to investigate quenching residual stress prediction and reduction methods in aircraft aluminum parts.

A lot of research on quenching residual stress has been carried out by researchers. Particularly with development of computer technology in recent years, numerical simulation technology has become an effective way to simulate the generation and distribution of residual stress during quenching process. Koç et al. used the finite element method to simulate the quenching and prestretching process to predict residual stress value of quenched and prestretched aluminum blocks [4–6]. Wu et al. studied the residual stress in aluminum blocks with different quenching processes [7–9]. Prime and Hill used the crack compliance method to measure the residual stress value in products of Alcoa and obtained residual stress distribution of quenched aluminum block and the corresponding prestretched block [10, 11]. Muammer et al. studied the residual stresses in quenched aluminum blocks

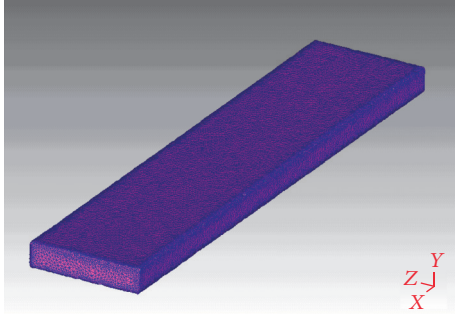


FIGURE 1: Finite element model.

TABLE 1: Heat transfer coefficient of 7A85 aluminum alloy.

Temperature (°C)	20	100	200	300	400	500
Transfer coefficient (W/m ² ·C)	2500	5000	13857	10000	3000	700

and their reduction through cold working processes [12, 13]. In this work, the effect of cold compression deformation on reducing quenching residual stress was studied through numerical simulation and experiment.

2. Simulation

2.1. Finite Element Model and Simulation Parameters. A thick block forging of 7A85 aluminum alloy with a large size of 260 (H) × 1150 (W) × 5300 (L) mm was chosen as the test component for the numerical analysis. The quenching and cold compression processes were subjected to numerical simulation in this study. The block was quenched in water of 20°C from initial 470°C and then 1%–5% cold compression deformation was conducted on the block along the highness direction. Finite Element Code Deform-3D was used to simulate the two processes. The shape and finite element model are shown in Figure 1.

Heat transfer coefficient between 7A85 aluminum alloy block and water which is the most important parameter in quenching process is given in Table 1 [14]. The heat capacity of 7A85 aluminum alloy obtained through DSC method by using the instrument NETZSCH STA 449 C is shown in Table 2. Flash method was used to get the thermal conductivity coefficient of 7A85 aluminum alloy by JR-3 machine. The measurement of thermal expansion coefficient was completed through NETZSCH DIL402C device. Both of them are given in Table 2.

2.2. Quenching Simulation Results and Discussion. Figure 2 shows the simulated results of temperature profile for the cooling time 10 s. Obviously, the temperature of edge at the block is the lowest and the temperature difference between the edge and the highest temperature of the block is about 400°C. This is due severely to heat convection at the edge along any two axis directions. The temperature gradient and temperature difference gradually decrease with prolonging cooling time. Two characteristic points 1 (surface) and 2

TABLE 2: Thermal conductivity and thermal expansion coefficient of 7A85 aluminum alloy.

Temperature (°C)	15	100	200	300	400	550
Heat capacity (J/g·°C)	1.02	0.95	1.1	1.07	1.24	1.07
Conductivity (W/m·°C)	185.3	182.0	217.3	218.2	228.1	187.2
Expansion (10 ⁻⁶ /°C)	*	24.3	25.9	26.7	28.2	*

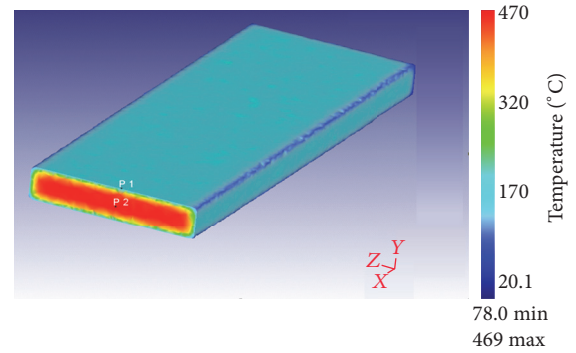


FIGURE 2: Results of temperature after cooling time 10 s.

(core) of the block shown in Figure 2 were employed for observing the temperature (T) change with cooling time (t) from 470°C to 20. Figure 3 gives the relative calculated results. The largest temperature difference between points 1 and 2 occurs in range of cooling time 10 to 15 s. The temperature difference produces the thermal stress in the internal, which leads to the deformation of the block. At the same time, the release of phase transition latent heat results in a decrease in the slope of T - t curves. Because the quenching process is very severe, the effect of the phase transition latent heat release on the temperature could be ignored. After quenching for about 350 seconds, the temperature distribution in the block evolves to be uniform and the magnitude is close to the water temperature. With increasing time, the temperature of the two points gradually reduces; it takes about 650 s for them to be cooled to the target temperature 20°C.

The final residual stress distribution of quenched block in length direction is shown in Figure 4. Figure 5 gives stress (X)-time curves for points 1 (surface) and 2 (core) of the block. In the initial stage of quenching, the normal stress was tensile at the surfaces and compressive in the core. Because of the sudden contraction of the surfaces and the great temperature gradient in the vicinity of the surface, the normal stress at surface point 1 increases sharply to about 70 MPa and then decreases slowly with the decreasing temperature gradient. At the same time, the compressive normal stress at the center point 2 gradually increases. During this process, the block undergoes plastic deformation. The plastic deformation finally results in the fact that the surface tensile residual stress shifts to compressive and the core

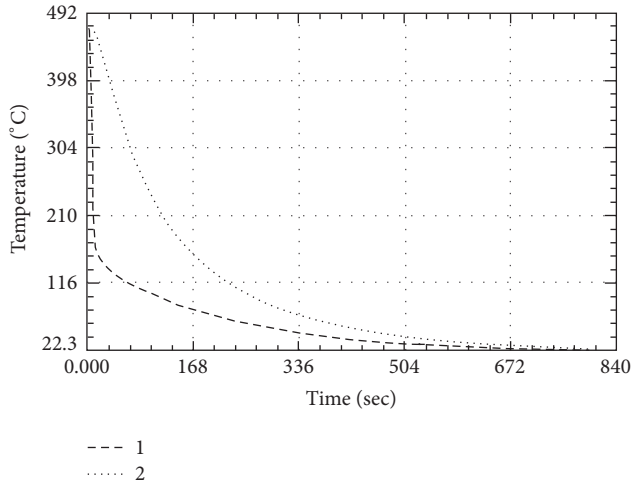


FIGURE 3: Temperature-time curves for points 1 and 2 in Figure 2.

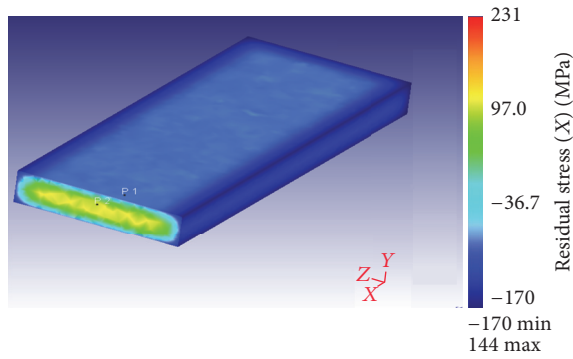


FIGURE 4: Results of residual stress (X) after quenching.

compressive stress switches into tensile stress at the later stage of quenching.

2.3. Compression Simulation Results and Discussion. Figure 6 shows the simulated results of residual stress distribution of the block for different cold compression values 0%, 1%, 2.5%, 4%, and 5%. The x - and y -axes stand for residual stress value and percentage of the block forging, respectively. It can be seen that the residual stress in length direction ranged from -170 MPa to 140 MPa when the quenching process was completed (Figure 6(a)). After conducting 1% cold compression deformation on the block along the direction of highness, the distribution range of residual stress in length direction significantly reduced that ranged from -110 MPa to 120 MPa (Figure 6(b)). This is due to the plastic deformation that redistributed the residual stress of the block. The range of residual stress in length direction of the block sharply reduces to the range from -65 MPa to 60 MPa as the compression deformation value runs up to 2.5%, and the uniformity was better than before (Figure 6(c)). However, when the deformation continued to come up to 4% and 5%, the ranges of residual stress in length direction of the block sharply widened which are from -90 MPa to 100 MPa and from -110 MPa to 120 MPa, respectively (Figures 6(d) and 6(e)).

TABLE 3: Cold compression deformation scheme.

Percentage	1%	2%	3%	4%	5%
Plastic deformation (mm)	0.4	0.8	1.2	1.6	2.0
Experimental deformation (mm)	0.9	1.2	1.6	2.0	2.4

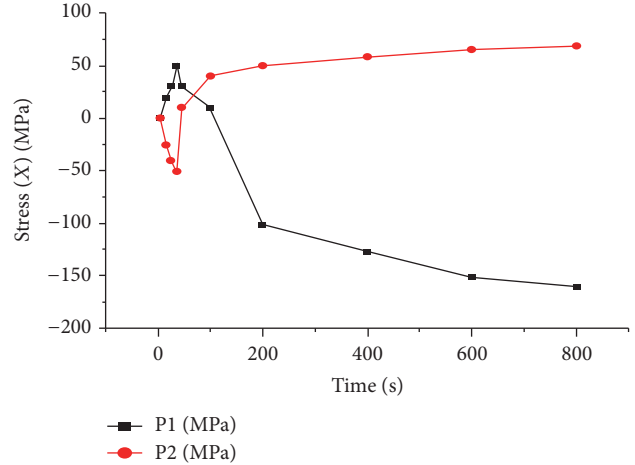


FIGURE 5: Stress (X)-time curves for points 1 and 2 in Figure 4.

This phenomenon can be explained by the fact that if the cold compression deformation continues to increase, it will produce much more elastic deformation in the block which is the main cause of the increase of residual stress. Therefore, for this simulation, it can be concluded that the optimal compression deformation value is about 2.5% for this large-sized block forging.

3. Cold Compression Experiment

Figure 7 shows the cold compression experimental specimens of 7A85 aluminum alloy forging with the size of 100 (L) \times 60 (W) \times 40 (H) mm provided by Southwest Aluminum Company and equipment of Central South University including X-ray diffraction device, and 4000t CNC hydraulic press machine. The entire experimental course was subdivided into four operations, which are quenching, measuring residual stress for the first time, cold compression deformation along the highness direction of specimens, and measuring residual stress for the second time. 1%–5% cold compression deformation was conducted on the quenched specimens along highness direction, respectively. The data of plastic deformation is shown in Table 3. Compression speed was 0.1 mm/s, which can be accurately controlled by the hydraulic control system. The residual stress of the same points on the surface of compressed specimens was measured by X-ray diffraction device in X, Y, and Z directions.

The results of cold compression deformation experiment are shown in Table 4 and Figure 8. The average values of residual stress for quenched specimens are -174.9 MPa,

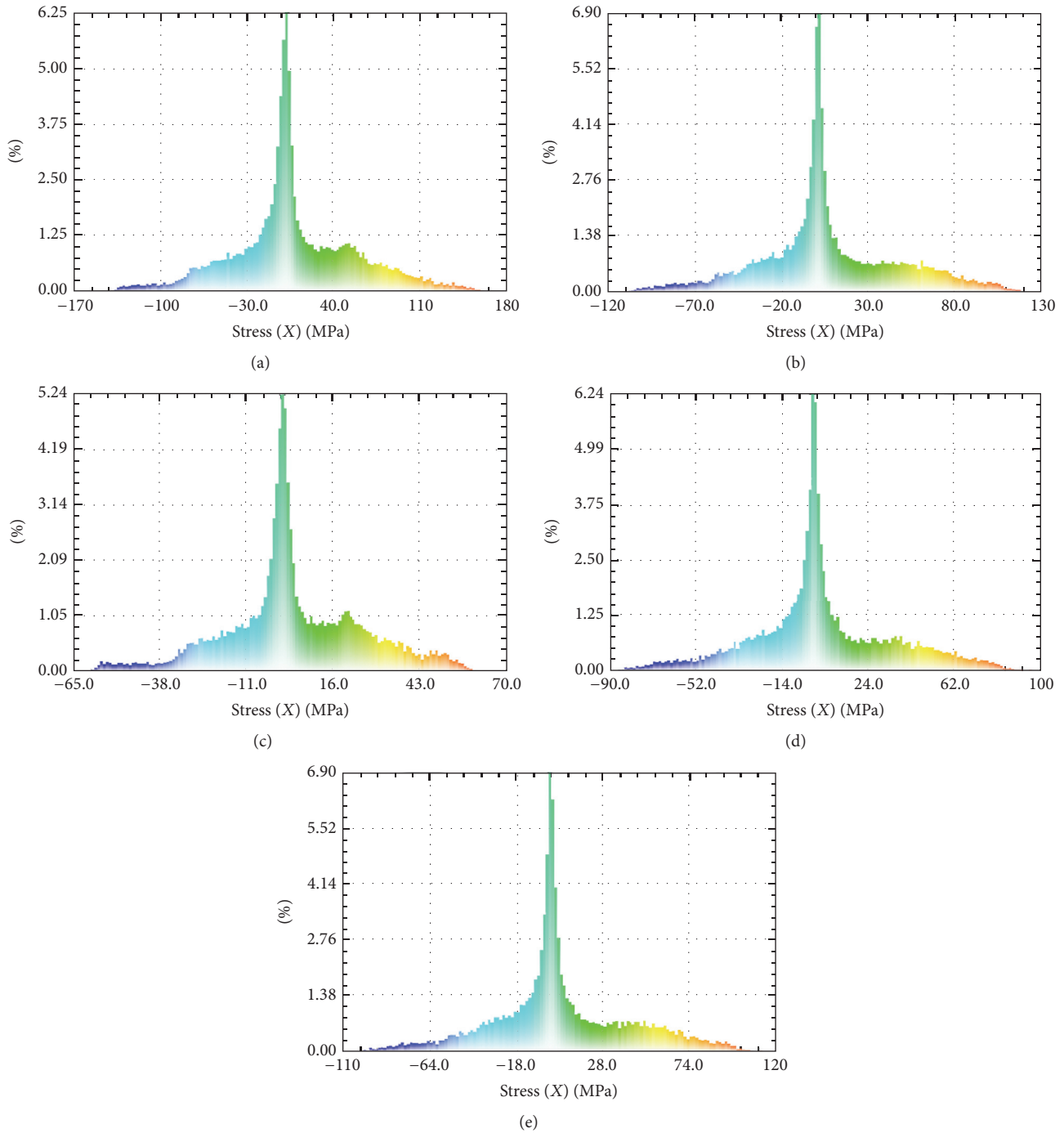


FIGURE 6: Results of residual stress (X) distribution for different compression value: (a) quenched; (b) 1%; (c) 2.5%; (d) 4%; (e) 5%.

-156.7 MPa, and -150.6 MPa, in X, Y, and Z directions, respectively. After conducting 1% compression deformation, the values of them reduced to 7 MPa, 53.4 MPa, and -5.9 MPa, respectively. When compression deformation exceeded 2%, the level of residual stress in three directions both obviously increased. It can be concluded that 1%-2% is the optimal compression deformation value which can reduce

70% residual stress for these 7A85 aluminum alloy specimens sized 100 (L) × 60 (W) × 40 (H) mm.

4. Conclusions

- (1) Physical property parameters of 7A85 aluminum alloy such as heat capacity, thermal conductivity,

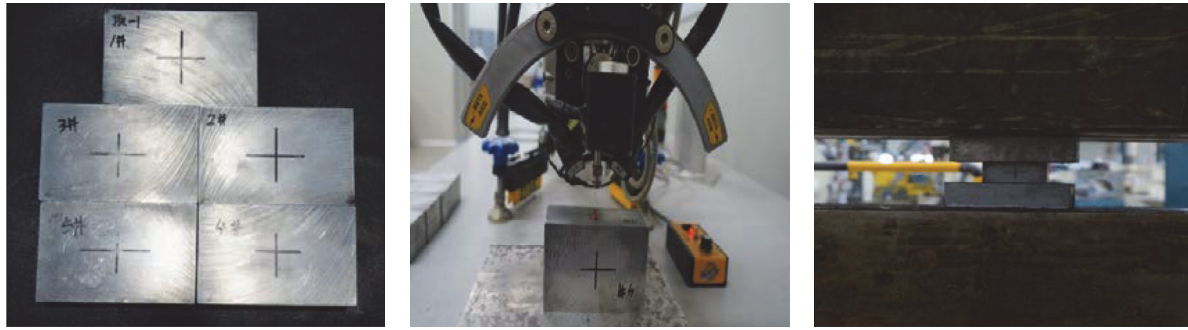


FIGURE 7: Experimental specimens and equipment.

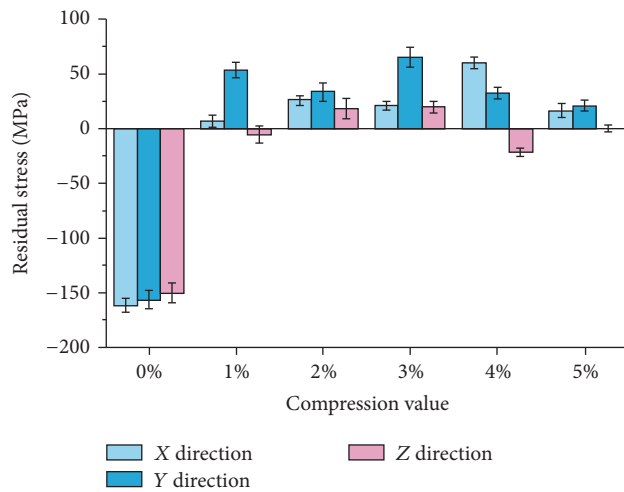


FIGURE 8: The error for measurement data.

TABLE 4: Residual stress of quenched and compressed specimens.

Compression value	X direction (MPa)	Y direction (MPa)	Z direction (MPa)
0%	-174.9	-156.7	-150.6
1%	7.0	53.4	-5.9
2%	28.2	33.7	18.3
3%	22.4	65.3	19.1
4%	64.9	32.4	-22
5%	17.8	20.8	-0.1

and expansion coefficient were obtained through experiments, which are the foundation of subsequent simulative and experimental research.

- (2) Cold compression deformation method has a significant effect on reducing quenching residual stress if an appropriate amount of compression deformation is chosen. The simulation results show that, in length direction of 7A85 aluminum alloy thick block with a large size of $260 \times 1150 \times 5300$ mm, quenching residual stress can be significantly reduced by about 2.5% cold compression deformation along the direction of highness, with residual stress in

length direction ranging from -65 MPa to 60 MPa, compared with that from -170 MPa to 140 MPa after quenching. The experimental results indicate that the optimal compression deformation value is about 1%-2%, reducing 70% residual stress for 7A85 aluminum alloy specimens sized $100 \times 60 \times 40$ mm.

Competing Interests

The authors declare that they have no competing interests.

Acknowledgments

The authors would like to thank The State Key Laboratory of High Performance and Complex Manufacturing (zzyjkt2014-02) and the National Basic Research Program of China (Grant 2012CB619504) for their financial support.

References

- [1] E. A. Starke Jr. and J. T. Staley, "Application of modern aluminum alloys to aircraft," *Progress in Aerospace Sciences*, vol. 32, no. 2-3, pp. 131-172, 1996.
- [2] P. Jeanmart and J. Bouvaist, "Finite element calculation and measurement of thermal stress in quenched plates of high strength 7075 aluminum alloy EJ," *Materials Science and Technology*, vol. 1, no. 3, p. 765, 1985.
- [3] D. J. Smith, C. G. C. Poussard, and M. J. Pavier, "An assessment of the Sachs method for measuring residual stresses in cold worked fastener holes," *Journal of Strain Analysis for Engineering Design*, vol. 33, no. 4, pp. 263-274, 1998.
- [4] M. Koç, J. Culp, and T. Altan, "Prediction of residual stresses in quenched aluminum blocks and their reduction through cold working processes," *Journal of Materials Processing Technology*, vol. 174, no. 1-3, pp. 342-354, 2006.
- [5] H. F. Wang, D. W. Zuo, and L. T. Wang, "Numerical analysis of surface residual stress of NC milling 7075-T7451 aluminum alloy," *Key Engineering Materials*, vol. 40, no. 7, pp. 718-722, 2009.
- [6] A. Arcari, R. De Vita, and N. E. Dowling, "Mean stress relaxation during cyclic straining of high strength aluminum alloys," *International Journal of Fatigue*, vol. 31, no. 11-12, pp. 1742-1750, 2009.

- [7] H. Gong, Y.-X. Wu, and K. Liao, "Influence of pre-stretching on residual stress distribution in 7075 aluminum alloy thick-plate," *Transactions of Materials and Heat Treatment*, vol. 30, no. 6, pp. 201–205, 2009.
- [8] C.-Y. Yao, *Numerical Simulation of Quench Temperature Field and Internal Stress Field of Aluminum Alloy 7050 Thick Plate*, Central South University, Changsha, China, 2007.
- [9] K. Liao, Y.-X. Wu, H. Gong, and S.-Y. Zhang, "Application of integral method on residual stress calculation along depth in aluminium alloy thick plate," *The Chinese Journal of Nonferrous Metals*, vol. 19, no. 6, pp. 1006–1011, 2009.
- [10] M. B. Prime and M. R. Hill, "Residual stress, stress relief, and inhomogeneity in aluminum plate," *Scripta Materialia*, vol. 46, no. 1, pp. 77–82, 2002.
- [11] M. B. Prime, "Residual stress measurement by successive extension of a slot: the crack compliance method," *Applied Mechanics Reviews*, vol. 52, no. 2, pp. 75–96, 1999.
- [12] K. Muammer, "Prediction of residual stresses in quenched aluminum blocks and their reduction through cold working processes," *Journal of Materials Processing Technology*, vol. 174, pp. 342–354, 2006.
- [13] D. A. Tanner and J. S. Robinson, "Modelling stress reduction techniques of cold compression and stretching in wrought aluminium alloy products," *Finite Elements in Analysis and Design*, vol. 39, no. 5-6, pp. 369–386, 2003.
- [14] S. Wang, *Analysis of Quenching Residual Stress and Its Reduction Process of 7A85 Aluminum Alloy Component*, Central South University, ChangSha, China, 2011.

Research Article

Development of a Master Sintering Curve for Al-Mg Alloy

Yong-Shin Lee,¹ Sang-Jun Lee,² Sangmok Lee,³ Eung-Zu Kim,³ and Duck Jae Yoon³

¹School of Mechanical Engineering, Kookmin University, 77 Jeongneung-ro, Seongbuk-gu, Seoul 02707, Republic of Korea

²Patent Information Promotion Center, 48 Munjeong-ro, 48-Beon-gil, Seo-gu, Daejeon 35262, Republic of Korea

³Metal Forming R&D Group, Korea Institute of Industrial Technology, Incheon 21999, Republic of Korea

Correspondence should be addressed to Yong-Shin Lee; yslee@kookmin.ac.kr

Received 27 June 2016; Accepted 25 August 2016

Academic Editor: Sutasn Thipprakmas

Copyright © 2016 Yong-Shin Lee et al. This is an open access article distributed under the Creative Commons Attribution License, which permits unrestricted use, distribution, and reproduction in any medium, provided the original work is properly cited.

A new master sintering curve (MSC) is proposed for Al-Mg alloy in order to effectively design the pressure-assisted sintering process. In this work, hot pressing experiments of Al-Mg alloy powders are performed. The changes of relative density during hot pressing are measured for the various heating rates of 5°C/min, 10°C/min, and 20°C/min at the fixed pressure of 50 MPa. A work of sintering, designated as Θ , is introduced and defined as $\Theta(t, T) = \int_0^t (1/T) \exp(-Q/RT) dt$. A work of sintering, Θ , could be interpreted as a measure for the amount of sintering work. The MSC in this work defines the relation between the apparent density and a work of sintering, Θ . Since the measurement of an apparent activation energy, Q , is very difficult, the correct value of Q is obtained numerically using a mean residual square method. Then, the master sintering curves for sintering of Al-Mg alloy powders are proposed for the sintering temperatures of 400°C and 500°C through scaling procedures. It is expected that the master sintering curves proposed in this work could help an engineer to design pressure-assisted sintering process for Al-Mg alloy.

1. Introduction

The demand for more light weight, fuel efficient, and enhanced performance automobiles has stimulated research and development in high-strength and high formability aluminum alloys. The Al-Mg alloys have medium to high strength, excellent formability, and good corrosion resistance [1]. However, it has been well known that sintering with the powder of Al-Mg alloys is not easy.

In the conventional design procedure of sintering, the parameters such as time and temperature of the sintering are decided mainly on the “trial and error” basis [2]. If the densification during sintering could be predicted from the sintering data that are really available, it would be helpful for engineers to design a new sintering process. Then, the sintering strategy could be established on that basis, which leads to the production of pellets of good quality and less number of defects. Therefore, there is a need for better understanding of a whole sintering procedure. The theory of master sintering curve (MSC) provides a new insight into the understanding of sintering process [3–5].

The master sintering curve enables engineers to predict the densification behavior under arbitrary time-temperature

schedules with the help of a minimum of preliminary experiments. However, this curve has been known as sensitive to the factors such as starting morphology of the powder, fabrication route, dominant diffusion mechanism, and heating condition used for sintering [6]. Thus, one may need a new MSC according to the changes of such factors if any of them is changed when designing a sintering process. A MSC can also be used as an aid to compare the sinterability of different powders and to examine the effects of additives, atmosphere, and fabrication procedure of sintering. Recent study could incorporate the effects of pressure on densification during sintering into one MSC such that the final density at any applied pressure in a pressure-assisted sintering can be predicted [2]. The concept of MSC, which was originally developed for the sintering of ceramic powders, has been successfully extended to the sintering with metallic powders such as Al_2O_3 , XnO , rhenium, and nickel powders [2–7]. More recently, pressure-assisted sintering of hard metallic powders such as tungsten alloys and WC alloys has been reported [8, 9]. For instance, An [9] constructed the master sintering curves for the mixture of WC, Cu, and Ni powders to understand densification behaviors during the resistance

heating. However, the extension of the concept of MSC to sintering with various metallic powders is still in early stage. The motivation for the present study is to extend the concept of the master sintering curve into the realm of hot pressing with metallic powders and to establish the pressure-assisted master sintering curve of Al-Mg alloy.

2. Theory of a Master Sintering Curve

Sintering of particulate materials is a thermally activated process involving the mass-transport phenomena that would result in particle bonding [10]. These mass-transport phenomena are generally to reduce the free surface area in the compact of particles. On the other hand, the surface transport mechanisms are to only grow the sinter bonding between particles. Thus, it is the bulk transport mechanisms that increase the density of porous body by gathering the particle together in order to reduce the free surface energy. Associated with this sintering densification is a decrease in volume, so the changes of density can be monitored by measuring dimensional changes of a compact during sintering. Hansen et al. [11] developed a *combined-stage sintering model* with the extensive studies on the mass-transport mechanisms during sintering, which is able to predict both the dimensional and density changes that take place during sintering. In their work, the compact densification is related to the dominant diffusional events such as grain boundary and volume diffusion, resulting in the following combined-stage sintering equation:

$$-\frac{dL}{Ldt} = \frac{\gamma\Omega}{kT} \left[\frac{\Gamma_v D_v}{G^3} + \frac{\Gamma_b D_b}{G^4} \right], \quad (1)$$

where L is a representative dimension of the compact, t is time, γ is the surface energy, Ω is the atomic volume, k is Boltzmann's constant, T is the temperature, Γ is a lumped scaling factor, D is the diffusivity, G is the grain size, and the subscripts v and b refer to volume diffusion and grain boundary diffusion, respectively.

For an isotropic shrinkage, the sintering shrinkage rate can be linked to the densification rate by considering the conservation of mass. Then, the following approximate relationship could be obtained:

$$-\frac{dL}{Ldt} = \frac{d\rho}{3\rho dt}. \quad (2)$$

Combining (1) and (2) provides a link between the densification rate and the diffusional sintering phenomena. However, the lumped scaling factors, Γ_v and Γ_b , are arbitrary parameters containing the density-dependent geometric terms. Furthermore, the diffusivities for grain boundary and volume diffusion, D , vary significantly between the studies [12]. These are the main reasons why no reliable value can be assigned confidently to a particular material. Thus, determination of the shrinkage and densification rates from the combined-stage sinter model requires experimental characterization of the lumped scaling factors and diffusivities for specific sintering systems. In order to overcome this difficult work, Su and Johnson [3, 6] tried to rearrange the

combined-stage sintering equation by grouping all of the density-dependent material parameters on one side, while the known process-dependent parameters, with the exception of the apparent activation energy Q , grouped on the other side:

$$\frac{k}{\gamma\Omega_a D_0} \int_{\rho_0}^{\rho} \frac{(G(\rho))^n}{3\rho\Gamma(\rho)} d\rho = \int_0^t \frac{1}{T} \exp\left(-\frac{Q}{RT}\right) dt. \quad (3)$$

Here, D_0 is the diffusivity preexponent. D_0 and n depend on the dominant sintering mechanism. The diffusivities as given in (1) follow Arrhenius temperature dependence and have been broken up into their preexponential and exponential terms in (3). Since the grain boundary and volume diffusion have diverse influences on the densification response of a sintering system, they have been lumped together as an apparent diffusivity in (3) to create a master sintering curve. Here, D_0 and n are determined as $D_0 = (D_b)_0$ and $n = 4$ for grain boundary diffusion and $D_0 = (D_v)_0$ and $n = 3$ for volume diffusion. The rearranged combined-stage sintering model would be integrated from the initial time to the current time for the right-hand side. Similarly, the left-hand side could be evaluated by integrating the function represented in terms of a density from the initial density to the current density which can be obtained at any state of (t, T, ρ) during thermal processing. The right-hand side of (3) could be interpreted as a measure of the energy supplied to the system during nonisothermal sintering. Correspondingly, the left-hand side might be interpreted as the increase of internal energy due to the changes of density during sintering.

Now, the term Θ , called a work of sintering in this work, is introduced as follows:

$$\Theta(t, T) = \int_0^t \frac{1}{T} \exp\left(-\frac{Q}{RT}\right) dt. \quad (4)$$

The apparent activation energy for sintering in (4) could be found through a numerical analysis, such as mean square residual method, the detailed procedure of which will be shown in the following section. Now it is clear that there must be an apparent density corresponding to a work of sintering, Θ , at a given time t . Once the relationship between the work of sintering and the relative density is established, a master sintering curve describing this relationship could be constructed using a scaling procedure or curve fitting.

3. Numerical Procedure to Construct a MSC

As mentioned previously, the MSC model is derived from the final equation of the combined-stage sintering model which is known as an even earlier attempt at the quantitative prediction of sintering behavior known. However, the MSC model offers a simpler method to predict the final density of a sintered product. The value of apparent activation energy is necessary to evaluate a work of sintering (Θ) in (4). But the accurate value of apparent activation energy (Q) is not known for many cases. Su and Johnson introduced the fitting procedure to obtain the proper value of apparent activation energy (Q) using the relationships between a work of sintering and density for at least three different heat

rates in sintering [6]. This procedure starts with an initially assumed value of Q . Then, the values of Θ and the density at the time t during sintering are evaluated with the assumed value of Q and they are plotted on the domain of ρ - Q . When the assumed values of Q are appropriate, then all the points corresponding to (ρ, Q) could be merged onto one curve. In this study, the proper value of apparent sintering activation energy is found out by minimizing the normalized dimensionless mean residual square, defined as the following equation as suggested by Su and Johnson [6]:

$$\text{Mean residual square} = \sqrt{\frac{1}{\rho_f - \rho_o} \int_{\rho_o}^{\rho_f} \frac{\sum_{i=1}^N (\Theta_i / \Theta_{\text{avg}} - 1)^2}{N} d\rho}, \quad (5)$$

where N is the number of experimental data, Θ_i is the work of sintering at i th experimental measurement, Θ_{avg} is the average value of all Θ_i over N , and ρ_f and ρ_o are the final density and initial density, respectively.

When the activation energy obtained here would be compared to those reported in the literatures for the activation energies associated with specific diffusional paths, that is, volume, surface, or grain boundary diffusion, the primary diffusional mechanisms in this sintering would be identified as explained in the others [10, 13]. Now, a MSC can be constructed by plotting the relative density, which would be extracted from experimental dilatometry data, against the natural logarithm of the work of sintering represented by (4). Again, all data points of (ρ, Θ) obtained with the accurate activation energy are merged onto one master curve or a master sintering curve. The sintering activation energy used in this calculation is temperature-dependent. There have been several tries to represent such complicated shape of a MSC with various functions. Su and Johnson invoked a polynomial function to describe the master sintering curve relationship [6]. However, a polynomial function generally requires many coefficients to precisely represent the complicated shape of a MSC. In order to reduce the material constant needed for a given MSC, it is a better way to invoke the function similar to the complicated curve shape. Teng et al. [14] and Blaine et al. [15] developed the new functions which can represent a sigmoidal shape. Teng et al. used three unknown parameters, but Blaine et al. used only two unknown parameters. In this study, we used Teng's sigmoidal function to better match the complicated master sintering curve of Al-Mg alloy, defined as the following equation:

$$\rho = \rho_o + \frac{a}{[1 + \exp(-(\ln \Theta - \ln \Theta_o)/b)^c]}, \quad (6)$$

where a , b , and c are the material constants. It should be mentioned that the material constants a and c coincide with the point of inflection of the curve while the constant b is the slope of the linearized portion. The overall procedure for the construction of master sintering curve is summarized in Figure 1.

TABLE 1: Chemical compositions of the Al-Mg alloy in weight percent.

Alloy	Mg	Mn	Zn	Si	Cu	Ni	Fe	Al
Al-Mg	4.00	0.59	0.03	0.15	0.39	0.02	0.24	Bal.

TABLE 2: Experimental schedules for hot pressing of Al-Mg alloy powders.

(a) 1st schedule.								
Sintering temperature [°C]								400
Holding time [min]								30
Sintering pressure [MPa]								50
Heating rate [°C/min]				5			10	20
Lubricant								Graphite foil
(b) 2nd schedule.								
Sintering temperature [°C]								500
Holding time [min]								0
Sintering pressure [MPa]								50
Heating rate [°C/min]				5			10	20
Lubricant								Graphite foil

4. Hot Pressing Experiments of Al-Mg Alloy

In order to develop a MSC of Al-Mg alloy, hot pressing experiments are carried out. The chemical compositions of the Al-Mg alloy used in experiments are given in Table 1. Al-Mg alloy powder having an average particle size of 45 μm filled a graphite mold in glove box for a hot pressing. The pellet was preformed at room temperature and under the uniaxial compression of 10 MPa. Its diameter and height are 20 mm and 13.5 mm, respectively. Each sample was pressed using Al-Mg alloy powders which weighted about 8 grams. The average density of a bulk body was calculated as $\rho = m/V$, where m is the mass and V is the volume. It must be mentioned that the densities in a bulk body are assumed as distributed uniformly. The experimental schedules for hot pressing experiments are summarized in Table 2. In order to properly construct a MSC, various experimental conditions were considered. The most important parameters in hot pressing are the peak temperature and its holding time. In this work, two schedules are considered: (1) peak temperature 400°C and holding time 30 min and (2) peak temperature 500°C and no holding time. Experiments with the above two schedules are performed under the various heating rates and pressures. The constant heating rates considered in this work are 5°C/min, 10°C/min, and 20°C/min. The sintering pressure of 50 MPa is examined. In experiments, the cooling was done in the furnace until the room temperature. The experimental apparatus of hot pressing in this work is newly developed and is schematically shown in Figure 2.

5. Construction of Master Sintering Curves for Al-Mg Alloy

First, the relative density could be evaluated based on the punch advancement in experiments and would be plotted

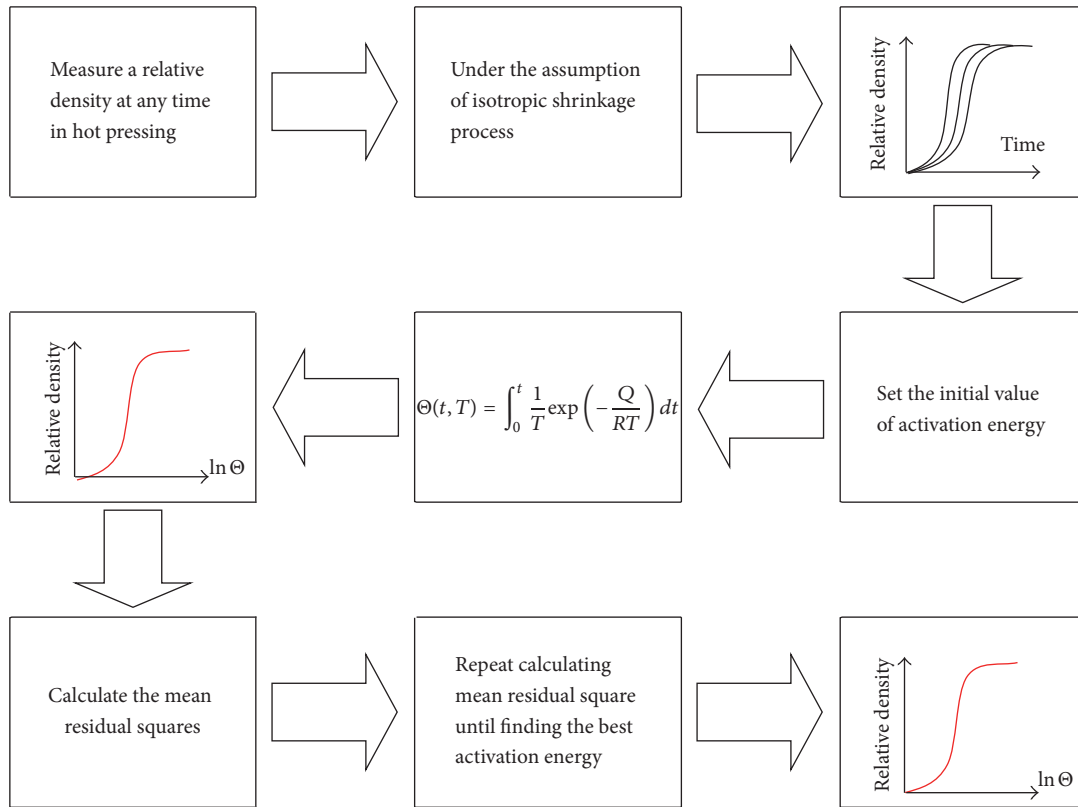


FIGURE 1: The overall procedure for the construction of a master sintering curve.

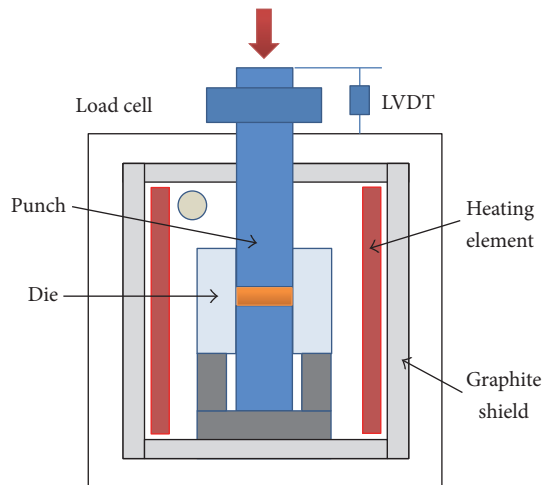


FIGURE 2: Schematic drawing of the hot press apparatus.

with respect to time during sintering. The densification curves, which represents the relative density changes during sintering, allow engineers to understand the characteristics of densification during sintering. Figure 3 shows various densification curves for various hot pressing conditions. Those are Case (a) sintering temperature of 400°C, pressure of 50 MPa, and holding time of 30 min and Case (b) sintering temperature of 500°C, pressure of 50 MPa, and no holding time. Three different heating rates of 5, 10, and 20°C/min

are examined. As shown in Figure 3, a densification curve may be divided into three sections. In the first section, the initial relative density holds until densification is activated. In the second section, the densification starts with the high rate of densification and this rate holds until the relative reaches about 95%. In the third section, the rate of densification becomes slow. Two intersection points are observed between 1st and 2nd sections and between 2nd and 3rd sections. It is observed that the first intersection point, the temperature for the initiation of visible densification, varies for three heating rates. Although the effect of pressure on the sintering process is not given specifically, sintering pressure of 20 MPa was examined in experiments. As expected, the pressure is shown to facilitate sintering by showing the fast appearance of the above intersection points. In experiments, temperature holding time is used as a parameter since it affects the sintering time. However, it should be noted that the important factor is not a temperature holding time but an exposure time to thermal activation or sintering time, which can induce the densification during sintering process. In high heating rate of 20°C/min, the exposure time without temperature holding time is much shorter than that with temperature holding time. Thereby, the final densification without temperature holding time in Figure 3(b) does not reach that with temperature holding time in Figure 3(a). In slow heating rate of 5°C/min, the sintering time with high peak temperature of 500°C is slightly shorter than that with temperature holding time at the low peak temperature of 400°C. As shown in Figure 3 for heating rate of 5°C/min, their densification

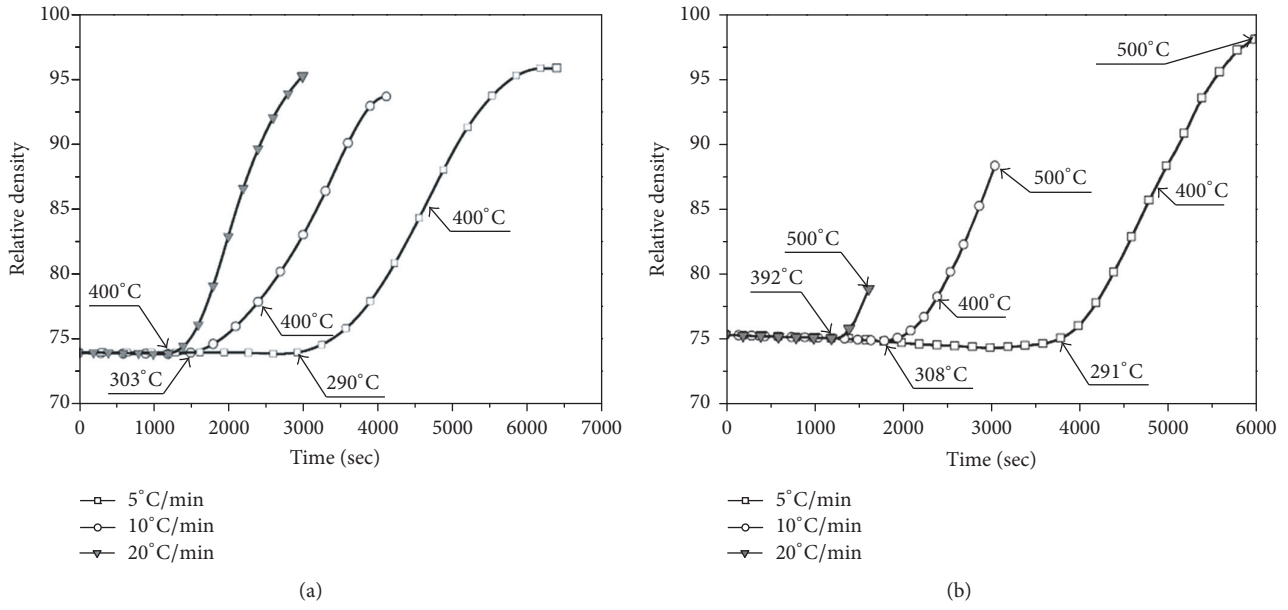


FIGURE 3: Density curves: (a) sintering temperature of 400°C, pressure of 50 MPa, and holding time of 30 min; (b) sintering temperature of 500°C, pressure of 50 MPa, and no holding time.

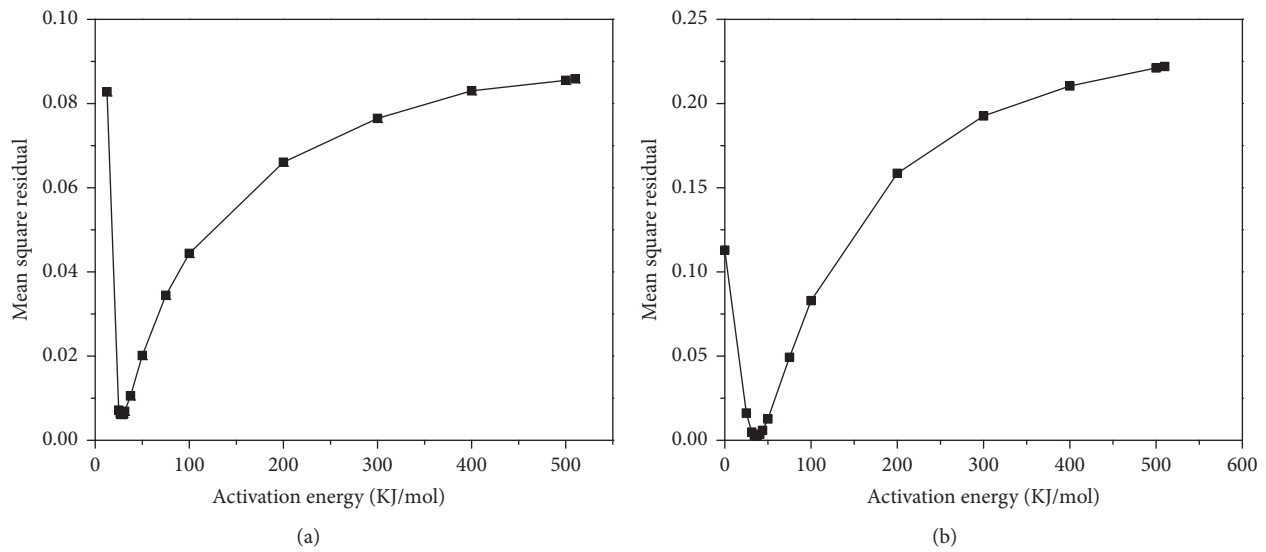


FIGURE 4: Mean square residual versus apparent activation energy: (a) sintering temperature of 400°C, pressure of 50 MPa, and holding time of 30 min; (b) sintering temperature of 500°C, pressure of 50 MPa, and no holding time.

behaviors are similar because the difference in the sintering time or exposure time to thermal activation between them is not so long. But the final density with the peak temperature of 500°C is slightly higher than that with the peak temperature 400°C although the exposure time with the peak temperature of 500°C is shorter. Thereby, one may say that the higher peak temperature could result in higher densification rate. Now, it may be concluded that the important factors in pressure-assisted sintering of Al-Mg alloy are the exposure time to thermal activation and the peak temperature.

In order to find a correct activation energy Q , an initial estimate for Q must be made. In this work, 500 KJ/mol is used as initial guess, which is much bigger than the correct values

given in the literatures. Then, the work of sintering (Θ) at the time, when the relative density was measured in experiments, can be computed using (4) for three heating rates of 5, 10, and 20°C/min. This procedure is repeated with the new value of activation energy Q , smaller than the current one, until Q reaches the value, close to zero such as 1. In this work, more than 50 values of Q are examined. The mean square residuals corresponding to those values of Q are calculated according to (5). Then, the variations of mean square residual corresponding to Q are plotted as given in Figures 4(a) and 4(b). It should be mentioned that the correct value of Q is obtained at the minimum of the mean square residual.

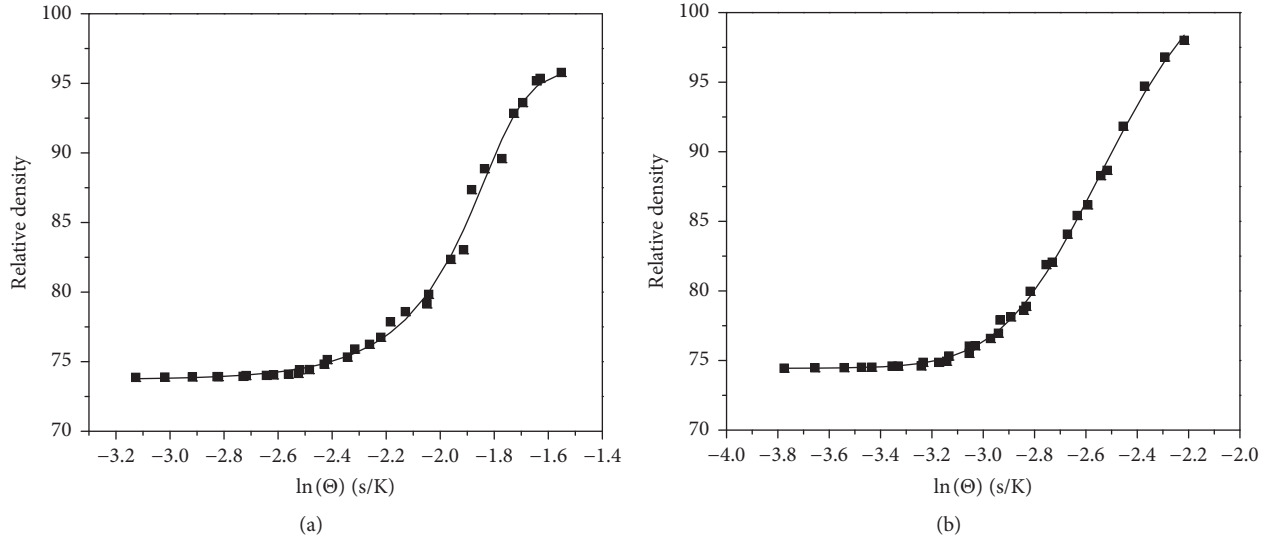


FIGURE 5: Master sintering curves: (a) sintering temperature of 400°C, pressure of 50 MPa, and holding time of 30 min; (b) sintering temperature of 500°C, pressure of 50 MPa, and no holding time.

Once the correct value of Q is given, then a master curve could be obtained that represents the relationship between the relative density at any time during sintering and the work of sintering until that time, defined by (4). When the relative density during sintering is plotted against the logarithm of a sintering work or $\ln(\Theta)$, it appears in a form of sigmoidal function given in (6).

As for Case (a) with three heating rates of 5, 10, and 20°C/min, the minimum of Q is found out as 28 KJ/mol as shown in Figure 4(a). Now, the other densification curve shown in Figure 3(a) could be merged into one master curve as shown in Figure 5(a). As shown in Figure 4(b), the minimum of Q is 36.4 KJ/mol for Case (b). The corresponding master sintering curve is given in Figure 5(b). The maximum errors between the predicted relative density by a master sintering curve and the measured density in experiments are less than 1% as shown in Figure 5. This implies that the concept of a master sintering curve can be successfully extended into the realm of hot pressing of Al-Mg alloy.

It should be noted that the values of activation energy obtained in this study are slightly bigger than that ($Q = 25.0$ KJ/mol) by Witkin et al. [16], although those values are generally below the activation energies of aluminum lattice with the main grain boundary self-diffusion mechanism reported in the literatures [17, 18]. In fact, the activation energy is very sensitive to the sintering conditions such as the preparing procedure of green compacts, the sintering procedure, applied pressure, peak temperature, and its holding time, even for the same material.

Now, the coefficients of the master sintering curves as represented in (6) are summarized in Table 3. The individual sintering points converged reasonably close to single curve. This indicates that there should have been a general curve, master sintering curve, which is independent of the sintering path or heating rates. It suggests that integration of a proposed sintering time-temperature profile yields a point on the

TABLE 3: The coefficients in the master sintering curves for Al-Mg alloy powders.

Condition	$\rho_s = \rho_0 + \frac{a}{[1 + \exp(-(\ln\Theta - \ln\Theta_0)/b)^c]}$			
	ρ_0	a	b	c
$P = 50$ MPa				
Temperature 400°C	73.72	22.38	0.07	0.32
Holding time 30 min				
$P = 50$ MPa				
Temperature 500°C	74.43	31.09	0.26	2.26
No holding time				

master sintering curve. The expected density can be obtained by finding the ordinate value at that point. On the other hand, if the final desired density is known, it is possible to obtain the corresponding Θ value from the abscissa of the master sintering curve and therefore to design the sintering schedule.

6. Conclusions

This study is concerned with the development of master sintering curves for Al-Mg alloy, which can provide a useful method to quantify the densification behavior during sintering. Hot pressing of Al-Mg alloy powders is performed under the constant heating rate at 5, 10, and 20°C/min for two schedules: (1st schedule) peak temperature 400°C and holding time 30 min; (2nd schedule) peak temperature 500°C and no holding time. The activation energy, Q , is obtained as 28.0 KJ/mol for the 1st schedule, while $Q = 36.4$ KJ/mol for the 2nd schedule. It is shown that the concept of master sintering curve could be successfully extended into the realm of hot pressing of Al-Mg alloy by constructing a master sintering curve for Al-Mg alloy. The constructed master sintering curves according to $Q = 28.0$ and 36.4 KJ/mol for the sintering

temperatures of 400°C and 500°C, respectively, show the maximum error of less than 1%. Finally, it is concluded that the master sintering curves presented in this work would be helpful for engineers to design a new sintering process of Al-Mg alloy.

Competing Interests

The authors declare that they have no competing interests.

References

- [1] L. Zhen and S. B. Kang, "The effect of pre-aging on microstructure and tensile properties of Al-Mg-Si alloys," *Scripta Materialia*, vol. 36, no. 10, pp. 1089–1094, 1997.
- [2] D. L. Johnson and H. Su, "A practical approach to sintering," *American Ceramic Society Bulletin Journal*, vol. 76, p. 72, 1997.
- [3] D. L. Johnson and H. Su, "The master sintering curve," *Advances in Powder Metallurgy and Particulate Materials*, vol. 2, p. 115, 1997.
- [4] D. L. Johnson, M. Henrichsen, J. Hwang, and V. P. Dravid, "Ultra rapid phase conversion in β " -alumina tubes," *Journal of the American Ceramic Society*, vol. 83, no. 11, pp. 2861–2862, 2000.
- [5] M. Stöcker, "From rapid prototyping to rapid manufacturing," *Auto Technology*, vol. 2, p. 38, 2002.
- [6] H. Su and D. L. Johnson, "Master sintering curve: a practical approach to sintering," *Journal of the American Ceramic Society*, vol. 79, no. 12, pp. 3211–3217, 1996.
- [7] W. Q. Shao, S. O. Chen, D. Li, H. S. Cao, T. C. Zhang, and S. S. Zhang, "Prediction and control of microstructure evolution for sub-microscale α -Al₂O₃ during low-heating-rate sintering based on the master sintering curve theory," *Journal of the European Ceramic Society*, vol. 29, no. 1, pp. 201–204, 2009.
- [8] S. J. Park, J. L. Johnson, Y. Wu, Y.-S. Kwon, S. Lee, and R. M. German, "Analysis of the effect of solubility on the densification behavior of tungsten heavy alloys using the master sintering curve approach," *International Journal of Refractory Metals and Hard Materials*, vol. 37, pp. 52–59, 2013.
- [9] K. J. An, "Application of the pressure-assisted master sintering surface," *Metals and Materials International*, vol. 20, no. 1, pp. 113–118, 2014.
- [10] R. M. German, *Sintering Theory and Practice*, John Wiley & Sons, New York, NY, USA, 1996.
- [11] J. D. Hansen, R. P. Rusin, M. -H. Teng, and D. L. Johnson, "Combined-stage sintering model," *Journal of the American Ceramic Society*, vol. 75, no. 5, pp. 1129–1135, 1992.
- [12] I. Kaur, W. Gust, and L. Kozma, *Handbook of Grain and Interphase Boundary Diffusion Data*, 1, University of Stuttgart, 1996.
- [13] J. Wang and R. Raj, "Estimate of the activation energies for boundary diffusion from rate-controlled sintering of pure alumina, and alumina doped with zirconia or titania," *Journal of the American Ceramic Society*, vol. 73, no. 5, pp. 1172–1175, 1990.
- [14] M. H. Teng, Y. C. Lai, and Y. T. Chen, "A computer program of master sintering curve model to accurately predict sintering results," *Western Pacific Earth Sciences*, vol. 2, no. 2, pp. 171–180, 2002.
- [15] D. C. Blaine, S. Park, and R. M. German, "Master sintering curve for a two-phase material," in *Proceedings of the 4th International Conference on Science, Technology and Applications of Sintering*, Grenoble, France, August 2005.
- [16] D. Witkin, B. Q. Han, and E. J. Lavernia, "Mechanical behavior of ultrafine-grained cryomilled Al 5083 at elevated temperature," *Journal of Materials Engineering and Performance*, vol. 14, no. 4, pp. 519–527, 2005.
- [17] Y. Sohn, "Diffusion in metals," in *Smithells Metals Reference Book*, W. F. Gale and T. C. Totemeier, Eds., chapter 13, Elsevier Butterworth-Heinemann, Oxford, UK, 8th edition, 2004.
- [18] H. J. Frost and M. F. Ashby, *Deformation-Mechanism Maps*, vol. 1, Pergamon Press, New York, NY, USA, 1982.

Research Article

Investigation of Thermostressed State of Coating Formation at Electric Contact Surfacing of “Shaft” Type Parts

Olena V. Berezshnaya,¹ Eduard P. Gribkov,² and Valeriy D. Kuznetsov¹

¹Department of Surface Engineering, National Technical University of Ukraine “Kyiv Polytechnic Institute” (NTUU “KPI”), Prospect Peremohy 37, Kyiv 03056, Ukraine

²Automated Metal Forming Process and Machinery Department, Donbass State Engineering Academy, Shkadinova 72, Donetsk Region, Kramatorsk 84313, Ukraine

Correspondence should be addressed to Olena V. Berezshnaya; elena.kassova07@gmail.com

Received 14 March 2016; Revised 28 July 2016; Accepted 6 September 2016

Academic Editor: Sutasn Thipprakmas

Copyright © 2016 Olena V. Berezshnaya et al. This is an open access article distributed under the Creative Commons Attribution License, which permits unrestricted use, distribution, and reproduction in any medium, provided the original work is properly cited.

The forming of coating at electric contact surfacing is considered. The mathematical model of the coating formation is developed. The method of numerical recurrent solution of the finite-difference form of static equilibrium conditions of the selected elementary volume of coating is used. This model considers distribution of thermal properties and geometric parameters along the thermal deformation zone during the process of electric contact surfacing by compact material. It is found that the change of value of speed asymmetry factor leads to increasing of the friction coefficient in zone of surfacing. This provides the forming of the coating of higher quality. The limitation of the technological capabilities of equipment for electric contact surfacing is related to the size of recoverable parts and application of high electromechanical powers. The regulation of the speed asymmetry factor allows for expanding the technological capabilities of equipment for electric contact surfacing. The nomograms for determination of the stress on the roller electrode and the finite thickness of the coating as the function of the initial thickness of the compact material and the deformation degree are shown.

1. Introduction

The creation of a coating with the necessary operating characteristics is a perspective direction in the reconditioning of worn parts as well as improvement of their service life [1–5]. This allows for providing a wide range of surface characteristics for various operating conditions.

One of the most common technological processes of the reconditioning of the worn parts is arc welding, which achieves the desired working layer on the surface of the product but has a number of disadvantages too. Those include a significant change in the initial phase state of coating material and substantial thermal effect in material of a part [6–8]. At such technological reconditioning, the magnitude of the heat-affected zone causes the development of residual stresses in the material of which the part is made. This has a negative impact on its durability even though force or heat is not applied to it. During the exploitation of the

parts reconditioned this way, the residual stresses are converted into exploitative residual stresses, which are the major cause of endurance reduce, cracks, and splits formation on the surface of product as well as of its deformation during production and exploitation. The coating technology based on the short-term heat influence allows avoiding the formation of the heat-affected zone of considerable size and thus the subsequent occurrence of the internal stresses. Such technologies include the electric contact method of surfacing of the coating with the specified operating characteristics, applied to the worn surfaces.

This method is a combination of short-term thermal and mechanical effects on the surfaced material located on the surface of a renewed rotating axisymmetric part, which allows for providing a tough coating. The conjoint plastic deformation of a renewed part together with adding material results in combination of the coating with the base metal. Currently, there are a lot of studies on the selection

of the recommended composition of the compact material, providing the desired performance characteristics of the coating. However, because of the short duration of the electric contact surfacing, there are some difficulties in predicting the quality of the coating and its compliance with basic operation characteristics. That is why it is necessary to use the mathematical apparatus for analytical design of electric contact surfacing in order to optimize the basic parameters of this process to obtain the coating that best meets the specified requirements.

Authors in [9] proposed the mathematical model of the coating formation on the surface of cylindrical parts with electric contact wire surfacing. In the work of [10], there is a mathematical model of forming of sintered tape reinforced by metal grid for increasing mechanical properties using the electric contact seam welding. Normal contact stresses in thermal deformation zone are determined. In the work of [11], an adhesive strength of surfaced layer with amorphous underlayer is considered. Regression equations for determining of adhesive strength are received. Coefficient of welded spots overlapping is represented. The mathematical models of the stress-strain state of the material on the basis of the conjoint finite-difference solutions of the equations of static equilibrium and conditions of plasticity in the works [12–14] are developed. This method is confirmed experimentally and widely used for solving this type of tasks. However, represented mathematical models are insufficiently reliable because of lack of consideration of the thermal state of material in thermal deformation zone.

The short-term thermomechanical exposure during the electric contact surfacing allows decreasing thermal influence on the coating and part material on the one hand and decreases the quality forecasting accuracy of the coating on the other hand. The adhesive strength of the coating to the part surface during the electric contact surfacing is an important quality indicator; thus, the task of developing technological methods to improve the adhesive strength is an actual problem.

2. Prime Novelty Statement

The formation of coating at electric contact surfacing of “shaft” type parts is investigated. The influence of the thermomechanic operating parameters on the coating formation on the surface of cylindrical part with predicted geometric parameters is investigated.

Based on the numerical recurrent solution of the finite-difference form of the static equilibrium conditions of selected elementary volume of the coating, mathematical model of coating formation was developed. Its peculiarity is the proper record of actual distribution of the thermal properties and geometric parameters on the length of thermal deformation zone during the process of electric contact surfacing by compact material. The problem of automated design of technological modes of electric contact surfacing is formulated and solved by using the developed mathematical model.

The method to improve the adhesive strength of the coating to the part surface by creation of the speed asymmetry

during the electric contact surfacing by the compact material is proposed.

The influence of the speed asymmetry factor on the friction coefficient changing in thermal deformation zone in the zone of contact of part with compact material is investigated.

The impact of the speed asymmetry factor on the energy-power and thermal operating parameters' changing is proved.

Results of research can be used in the designing of equipment for electric contact surfacing, as well as in selection of optimal operating parameters of surfacing process.

3. Theoretical Studies

The mathematical model of electric contact surfacing of “shaft” type parts is developed on the basis of the numerical recurrence solution of the finite-difference form of static equilibrium conditions of selected elementary volumes [15–18]. The plastic deformation zone $a_1c_1c_2a_2$ is divided on the finite set of elementary volumes (Figure 1).

Due to the specific realization conditions of considered technology, we should point out that the circumferential speed of part 1 and compact material 2 at the outlet from the plastic deformation zone are equal; that is, $V_2 = V_1$. That is why there is only a zone of the lag $L_{lg1} = L_{pl}$ on the surface of the part. The tangential contact stresses τ_{x1} have the same direction with the surfacing process at this zone. The circumferential speed of the roller electrode V_2 is a bit lower than surface speed V_1 . The speed asymmetry factor is characterized by the ratio of $V_2 = V_1/K_v$. This causes the formation of the zone of lag L_{lg2} on the roller electrode. There is also a mixed zone L_m , in which tangential contact stresses τ_{x2} are contradirectional with surfacing process (see Figure 1).

In addition to the abovementioned, a number of assumptions were adopted. The most important of them are the following.

(i) Deformation of compact material 2 (see Figure 1) is flat and set in time. The kinematics of plastic flow of the material obey hypothesis of flat sections. The normal axial stresses σ_{xi} and performances of the double shift resistance $2K_{xi}$ are changed only along the zone of plastic deformation.

(ii) On the length of each selected i th elementary volume (Figure 2), the current values of the thicknesses $h_{xi} = h_{xi1} \cdots h_{xi2}$, normal contact $p_{xi} = p_{xi1} \cdots p_{xi2}$, and tangential contact stresses $\tau_{x2i1} = \tau_{x2i1} \cdots \tau_{x2i2}$ are changed linearly.

(iii) Analytical descriptions of tangential contact stresses τ_{xi1}, τ_{xi2} are subordinate to plastic friction law proposed by Siebel and running as follows:

$$\begin{aligned}\tau_{x1} &= 2K_x \mu_{x1}; \\ \tau_{x2} &= 2K_x \mu_{x2}.\end{aligned}\tag{1}$$

The value of double shift resistance of the compact material is determined with considering current values of degree, speed, and temperature of deformation. The current value

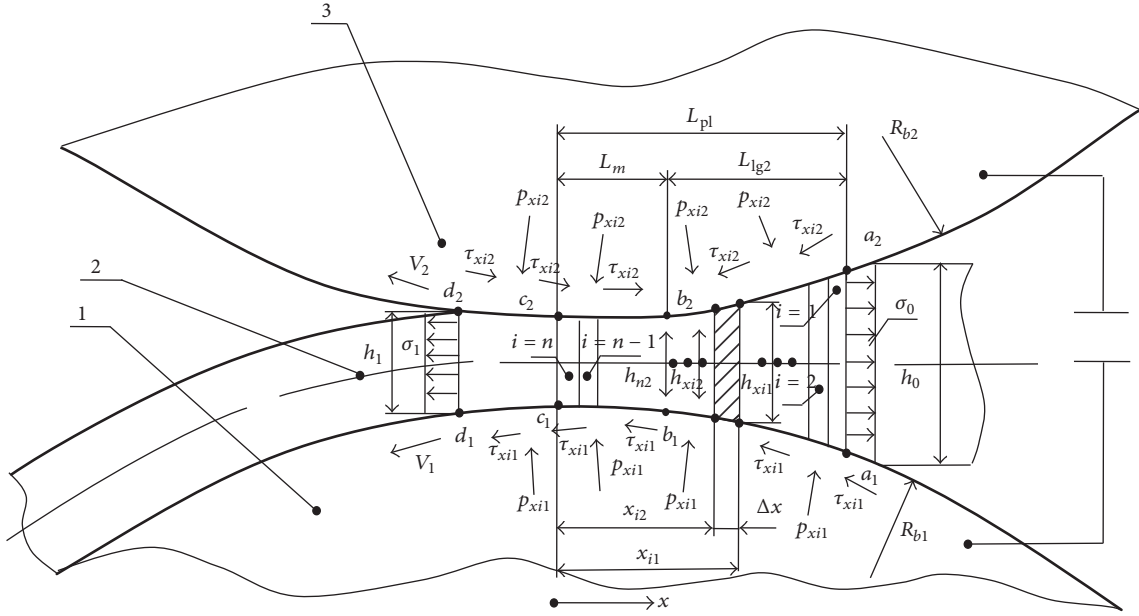


FIGURE 1: Design model for process of "shaft" type parts surfacing (1: part to be surfaced, 2: compact material, and 3: roller electrode).

of the plastic friction coefficients depends on the geometric coordinate x as follows:

$$\mu_{x1} = \mu_{01} \left(\frac{x}{L_{pl}} \right)^{a_{\mu 1}}. \quad (2)$$

$$\mu_{x2} = \mu_{02} \left[\frac{(x - L_m)}{(L_{pl} - L_m)} \right]^{a_{\mu 2}} \quad \text{at } L_m \leq x \leq L_{pl}; \quad (3)$$

$$\mu_{x2} = -\mu_{02} \left[\frac{(L_m - x)}{L_m} \right]^{a_{\mu 2}} \quad \text{at } 0 \leq x \leq L_m; \quad (4)$$

(iv) We neglect the presence of an elastic compression zone of surfaced compact material in sections at the inlet of the deformation zone, as well as the presence of the inertial components of the equilibrium conditions, due to their very low influence.

(v) Analytical description of the current thicknesses value h_x of the coating along the zone of plastic deformation L_{pl} can be represented by a dependence:

$$h_x = h_1 + (h_0 - h_1) \left(\frac{x}{L_{pl}} \right)^{a_h}, \quad a_h \approx 2. \quad (5)$$

(vi) The total length of zone of the plastic deformation L_{pl} , the volume of its partition step Δx , geometric coordinates of initial x_{i1} , finite x_{i2} boundary sections for selected i th elementary volume, and also the length of the mixed zone L_m can be defined as

$$L_{pl} = \sqrt{2R_{b1}R_{b2} \frac{(h_0 - h_1)}{(R_{b1} + R_{b2})} - \frac{(h_0 - h_1)^2}{4}};$$

$$\Delta x = \frac{L_{pl}}{n};$$

$$x_{i1} = L_{pl} - \Delta x (i - 1);$$

$$x_{i2} = x_{i1} - \Delta x;$$

$$h_{n2} = \frac{h_1 V_{b1}}{V_{b2}} = h_1 K_v;$$

(6)

$$L_m = \sqrt{2R_{b1}R_{b2} \frac{(h_{n2} - h_1)}{(R_{b1} + R_{b2})} - \frac{(h_{n2} - h_1)^2}{4}}. \quad (7)$$

Given the nature of the assumptions and finite-difference record forms of the main components of the stress-strain state (see Figure 2), the condition of static equilibrium for selected i th elementary volume in the axle projection of all the forces on the axis x runs as follows:

$$\begin{aligned} \sum F_x = & \sigma_{xi2} h_{xi2} - \sigma_{xi1} h_{xi1} \\ & + \frac{(p_{xi1} + p_{xi2})(h_{xi1} - h_{xi2})}{2} \\ & + \frac{(2K_{xi1}\mu_{x1i1} + 2K_{xi2}\mu_{x1i2}) \Delta x}{2} \\ & + \frac{(2K_{xi1}\mu_{x2i1} + 2K_{xi2}\mu_{x2i2}) \Delta x}{2} = 0, \end{aligned} \quad (8)$$

where the positive values of the normal components for the stress tensors σ_{xi2} , σ_{xi1} and p_{xi2} , p_{xi1} correspond to the compression stresses. The opposite direction of tangential contact stresses τ_{x2} is accounted by signs in analytical descriptions

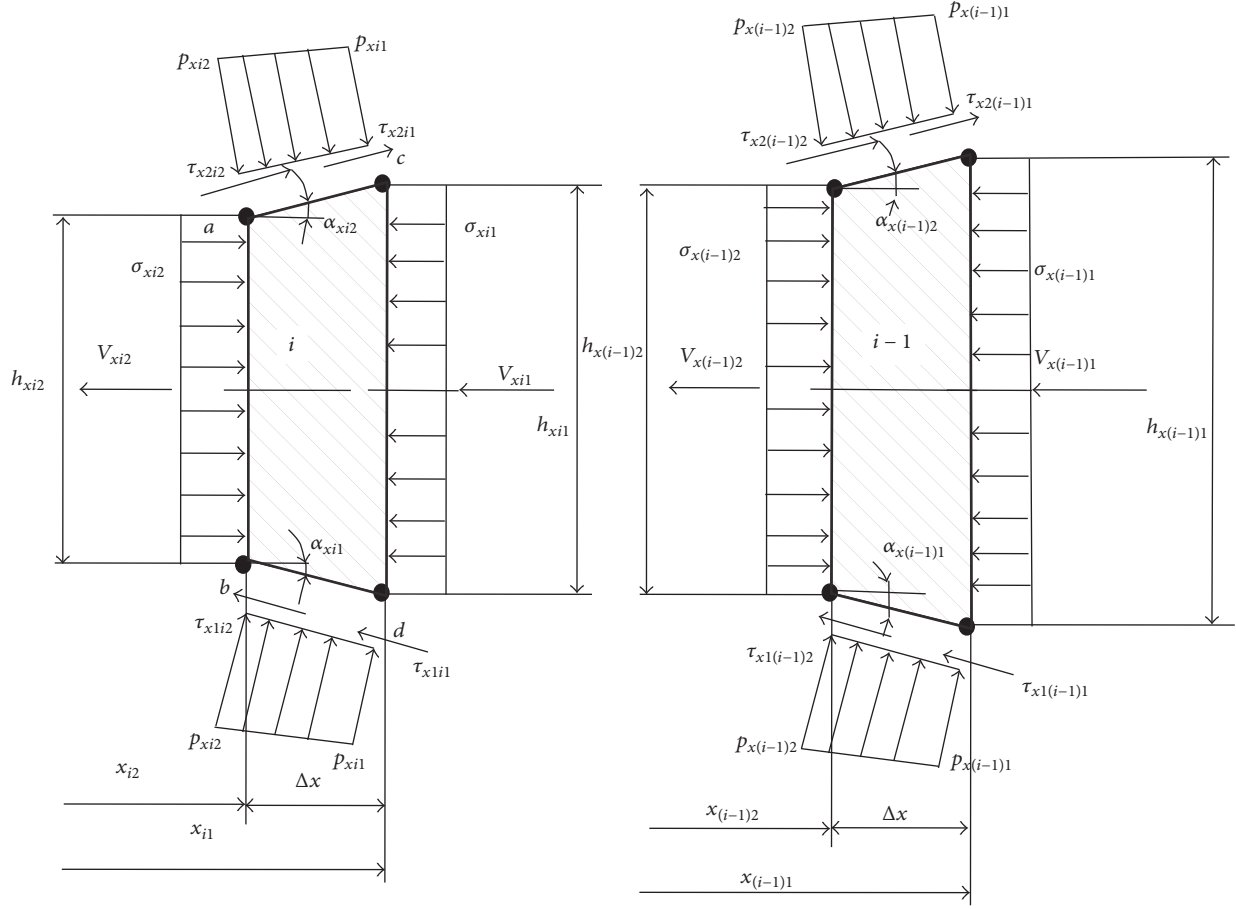


FIGURE 2: Design diagrams of elementary volumes of mathematical modeling of stress-strain state of the compact material.

(3)-(4) of current values for plastic friction coefficient values μ_{x2} .

The current levels of double shift resistance $2K_{xi1}$ and K_{xi2} are defined using the conventional methods. The values of the components $\Delta x, h_{xi1}, h_{xi2}, \mu_{x1i1}, \mu_{x1i2}, \mu_{x2i1}, \mu_{x2i2}$ are calculated according to (2)–(7). Due to the recurrent scheme of solutions, the components of the stress states σ_{xi1} and p_{xi1} are known according to calculation results of the previous $(i-1)$ elementary volume (see Figure 2). Expression (8) is an equation with two unknown values σ_{xi2} and p_{xi2} , which, following the engineering version of the plasticity condition, can be transformed as

$$(p_{xi2} - 2K_{xi2})h_{xi2} - \sigma_{xi1}h_{xi1}$$

$$p_{xi2} = \frac{\{2(\sigma_{xi1}h_{xi1} + 2K_{xi2}h_{xi2}) - p_{xi1}(h_{xi1} - h_{xi2}) + [2K_{xi1}(\mu_{x1i1} + \mu_{x2i2}) + 2K_{xi2}(\mu_{x2i1} + \mu_{x2i2})]\Delta x\}}{(h_{xi1} + h_{xi2})}, \quad (10)$$

where normal axial stresses in the zone of plastic deformation, following the engineering version of plasticity conditions, can be defined as $\sigma_{xi2} = p_{xi2} - 2K_{xi2}$ [12].

$$\begin{aligned} & + \frac{(p_{xi1} + p_{xi2})(h_{xi1} - h_{xi2})}{2} \\ & - \frac{(2K_{xi1}\mu_{x1i1} + 2K_{xi2}\mu_{x1i2})\Delta x}{2} \\ & - \frac{(2K_{xi1}\mu_{x2i1} + 2K_{xi2}\mu_{x2i2})\Delta x}{2} = 0. \end{aligned} \quad (9)$$

Equation (9) can be solved only for the one unknown value p_{xi2} . In a final form, after the appropriate mathematical transformations, we obtain

As the directions of recurrent circuit of solutions, the direction of the compact material is used. Taking this into account, the initial conditions for the first $i = 1$ elementary

volume and condition of communication at the transition from the calculation of the i to the calculation $(i + 1)$ were adopted in the following form:

$$\begin{aligned}
 x_{i1}|_{i=1} &= L_{p1}; \\
 h_{xi1}|_{i=1} &= h_0; \\
 \mu_{x1i1}|_{i=1} &= \mu_{01}; \\
 \mu_{x2i1}|_{i=1} &= \mu_{02}; \\
 \sigma_{xi1}|_{i=1} &= -\sigma_0; \\
 p_{xi1}|_{i=1} &= 0.0; \\
 x_{(i+1)1} &= x_{i2}; \\
 h_{x(i+1)1} &= h_{xi2}; \\
 \mu_{x1(i+1)1} &= \mu_{x1i2}; \\
 \mu_{x2(i+1)1} &= \mu_{x2i2}; \\
 \sigma_{x(i+1)1} &= \sigma_{xi2}; \\
 p_{x(i+1)1} &= p_{xi2}.
 \end{aligned} \tag{11}$$

With the calculation of local characteristics for stress-strain state within zones of the plastic deformation of the compact material by numerical integration, there were certain forces P and moments M_1 and M_2 of electric contact surfacing:

$$\begin{aligned}
 P &= \left[\sum_{i=1}^n \frac{(p_{xi1} + p_{xi2}) \Delta x}{2} \right] b; \\
 M_1 &= \left[\sum_{i=1}^n \frac{(p_{xi1} \mu_{x1i1} + p_{xi2} \mu_{x1i2}) \Delta x}{2} \right] b R_{b1}; \\
 M_2 &= \left[\sum_{i=1}^n \frac{(p_{xi1} \mu_{x2i1} + p_{xi2} \mu_{x2i2}) \Delta x}{2} \right] b R_{b1}.
 \end{aligned} \tag{12}$$

Modeling of thermal state of compact material in thermal deformation zone at electric contact surfacing is performed with considering of the compact material as unlimited plate [19]. Heating process is calculated according to the theory of heat conduction. The compact material is in temperature equilibrium with environment; that is, the temperature of the compact material is equal to the environment temperature T_o . Heat transfer between the surfaces of compact material and superficial layer in the thermal deformation zone proceeds in accordance with Newton's law [15]. Let us suppose that the origin of coordinates is in the middle of compact material. Then, r is the half of the thickness of compact material; that is, $r = h_{xi1}/2$. To determine the heat distribution at any given moment, it is necessary to solve the differential Laplace equation of heat conduction:

$$\frac{\partial T_m(y, t)}{\partial t} = a \frac{\partial^2 T_m(y, t)}{\partial y^2}; \quad (t > 0; -r < y < r) \tag{13}$$

with the initial and boundary conditions

$$T_m(y, 0) = T_o; \tag{14}$$

$$\frac{\partial T_m(0, t)}{\partial y} = 0, \tag{15}$$

$$-\lambda \frac{\partial T_m(r, t)}{\partial y} + \alpha [T(t) - T_m(y, t)] = 0. \tag{16}$$

With considering that $T(t)$ is the linear function of time, the boundary condition (16) can be obtained as

$$-\frac{\partial T_m(r, t)}{\partial y} + \frac{\alpha}{\lambda} [T_o + gt - T_m(r, t)] = 0. \tag{17}$$

Equations (13)–(17) can be solved by operating method with Laplace transformation:

$$L \left[\frac{\partial T_m(y, t)}{\partial t} \right] = L \left[a \frac{\partial^2 T_m(y, t)}{\partial y^2} \right], \tag{18}$$

where

$$L [T_m(y, t)] = \int_0^\infty T_m(y, t) e^{-st} dt = T_L(y, s). \tag{19}$$

The differential equation of heat conductivity with considering of initial condition (14) after Laplace transformation can be solved as

$$T_L''(y, s) - \frac{s}{a} T_L(y, s) + \frac{T_o}{a} = 0. \tag{20}$$

The solution of (20) for image $T_L(y, s)$ can be defined as

$$T_L(y, s) - \frac{T_o}{s} = A \operatorname{ch} \left(\sqrt{\frac{s}{a}} y \right) + B \operatorname{sh} \left(\sqrt{\frac{s}{a}} y \right), \tag{21}$$

where A and B are constants, defined from boundary conditions (15) and (16).

According to symmetry condition (15),

$$\begin{aligned}
 T_L'(0, s) &= \left[A \sqrt{\frac{s}{a}} \operatorname{sh} \left(\sqrt{\frac{s}{a}} y \right) + B \sqrt{\frac{s}{a}} \operatorname{ch} \left(\sqrt{\frac{s}{a}} y \right) \right]_{y=0} \\
 &= B \sqrt{\frac{s}{a}} = 0,
 \end{aligned} \tag{22}$$

where $B = 0$.

Boundary condition (16) for image can be solved as

$$\begin{aligned}
 -T_L'(r, s) + \frac{\alpha T_o}{\lambda s} + \frac{\alpha g}{\lambda s^2} - \frac{\alpha}{\lambda} T_L(r, s) &= 0, \\
 L \left[\frac{\alpha}{\lambda} gt \right] &= \frac{\alpha g}{\lambda s^2}.
 \end{aligned} \tag{23}$$

With considering $B = 0$, (21) can be presented as

$$\begin{aligned}
 -A \sqrt{\frac{s}{a}} \operatorname{sh} \left(\sqrt{\frac{s}{a}} r \right) + \frac{\alpha T_o}{\lambda s} + \frac{\alpha g}{\lambda s^2} - \frac{\alpha T_o}{\lambda s} \\
 - A \frac{\alpha}{\lambda} \operatorname{ch} \left(\sqrt{\frac{s}{a}} r \right) = 0.
 \end{aligned} \tag{24}$$

Then, constant A can be defined from

$$A = \frac{g}{s^2 [ch(\sqrt{s/ar}) + (\lambda/\alpha) \sqrt{s/a} sh(\sqrt{s/ar})]}. \quad (25)$$

Thus, the solution for the image is

$$\begin{aligned} T_L(y, s) - \frac{T_o}{s} &= \frac{gch(\sqrt{s/a}y)}{s^2 [ch(\sqrt{s/ar}) + (\lambda/\alpha) \sqrt{s/a} sh(\sqrt{s/ar})]} \\ &= \frac{\Phi_1(s)}{\Phi_2(s)}. \end{aligned} \quad (26)$$

Solution (26) is the ratio of generalized polynomials concerning s . Besides, the polynomial $\Phi_2(s)$ does not contain any constants; that is, solution responds to conditions of decomposition theorem. Thus, it can be used in solution of initial equation.

The decomposition theorem can be presented as

$$L^{-1} \left[\frac{\Phi_1(s)}{\Phi_2(s)} \right] = \sum_{n=1}^{\infty} \frac{\Phi_1(s_n)}{\Phi_2'(s_n)} e^{s_n t}, \quad (27)$$

where s_n are the roots of polynomial $\Phi_2(s)$.

If $\Phi_2(s) = 0$, then the roots are $s_0 = 0$, double root; $s_n = -a\mu_n^2/r^2$, where $\mu = i\sqrt{s/ar}$ —are the simple roots, defined from characteristic equation:

$$ctg\mu = \frac{\mu}{Bi}, \quad (28)$$

where $Bi = \alpha r/\lambda$, Biot criterion [20].

According to the decomposition theorem,

$$L^{-1} \left[\frac{\Phi_1(0)}{\Phi_2(0)} \right] = gt + \frac{g}{2a} \left[y^2 - r^2 \left(1 + \frac{2\lambda}{\alpha r} \right) \right]. \quad (29)$$

The substitution of other roots s_n into (27) allows for obtaining

$$\begin{aligned} \sum_{n=1}^{\infty} \frac{\Phi_1(s_n)}{\Phi_2'(s_n)} e^{s_n t} &= \frac{gr^2}{a} \sum_{n=1}^{\infty} \frac{2 \sin \mu_n}{(\mu_n + \sin \mu_n \cos \mu_n)} \\ &\cdot \frac{1}{\mu_n^2} \cos \left(\mu_n \frac{y}{r} \right) \exp \left(-\mu_n^2 \frac{at}{r^2} \right). \end{aligned} \quad (30)$$

Thus, the solution can be presented as

$$\begin{aligned} T_m(y, t) - T_o &= gt - \frac{g}{2a} \left[r^2 \left(1 + \frac{2}{Bi} \right) - y^2 \right] \\ &+ \frac{gr^2}{a} \sum_{n=1}^{\infty} \frac{A_n}{\mu_n^2} \cos \left(\mu_n \frac{y}{r} \right) \exp \left(-\mu_n^2 Fo \right), \end{aligned} \quad (31)$$

where $Fo = at/r^2$ is the Fourier criterion [20] and A_n are the initial amplitudes, defined as

$$A_n = \frac{2 \sin \mu_n}{\mu_n + \sin \mu_n \cos \mu_n}. \quad (32)$$

Equation (31) allows for calculating the temperature $T_m(y, t)$ in any point of compact material in thermal deformation zone. The intensity of temperature increasing is characterized by the nondimensional heating rate, which is the Predvoditelev criterion [20]:

$$Pd = \left(\frac{dT}{dFo} \right)_{\max}. \quad (33)$$

If $T(t) = T_o + gt$, then

$$Pd = \frac{gr^2}{a}. \quad (34)$$

Then, the solution can be presented as

$$\begin{aligned} \frac{\Delta T_m}{Pd} &= \frac{T_m(y, t) - T_o}{Pd} \\ &= Fo - 0.5 \left(1 + \frac{2}{Bi} - \frac{y^2}{r^2} \right) \\ &+ \sum_{n=1}^{\infty} \frac{A_n}{\mu_n^2} \cos \left(\mu_n \frac{y}{r} \right) \exp \left(-\mu_n^2 Fo \right). \end{aligned} \quad (35)$$

Thus, the relative temperature in any point of compact material in thermal deformation zone is the function of nondimensional values Fo , Bi , and y/r . At the axes of the compact material, that is, at $y = 0$, (35) can be presented as

$$\frac{\Delta T_m}{Pd} = Fo - 0.5 \left(1 + \frac{2}{Bi} \right) + \sum_{n=1}^{\infty} \frac{A_n}{\mu_n^2} \exp \left(-\mu_n^2 Fo \right). \quad (36)$$

In this point, the temperature of compact material is minimal.

Knowing the distribution of temperature fields along the length of compact material in thermal deformation zone, required current pulse can be calculated as

$$I = \sum_{i=1}^{\infty} \sqrt{\frac{T\pi^2 x_i h_{xi} \lambda c g}{r \delta t_i}}. \quad (37)$$

Presented set of analytical descriptions made the complete algorithm for the numerical one-dimensional mathematical modeling of electric contact surfacing for parts such as bodies of rotation by a compact material. The aggregated block diagram of this solutions algorithm is shown in Figure 3. The software for calculation of the power-energy and thermal operating parameters of the electric contact surfacing is developed using the aggregated block diagram. As an example of the received software resources, the calculated distributions of the local and integral characteristics for electric contact surfacing process are shown in Figures 4–10.

The peculiarity of the proposed mathematical model is the correct consideration of distribution of the thermal characteristics of the compact material along the thermal deformation zone, which significantly affects the forming of welded joint during the surfacing process. The adhesive strength, structural homogeneity, and the geometric parameters of the coating are the quality indicators of the surface

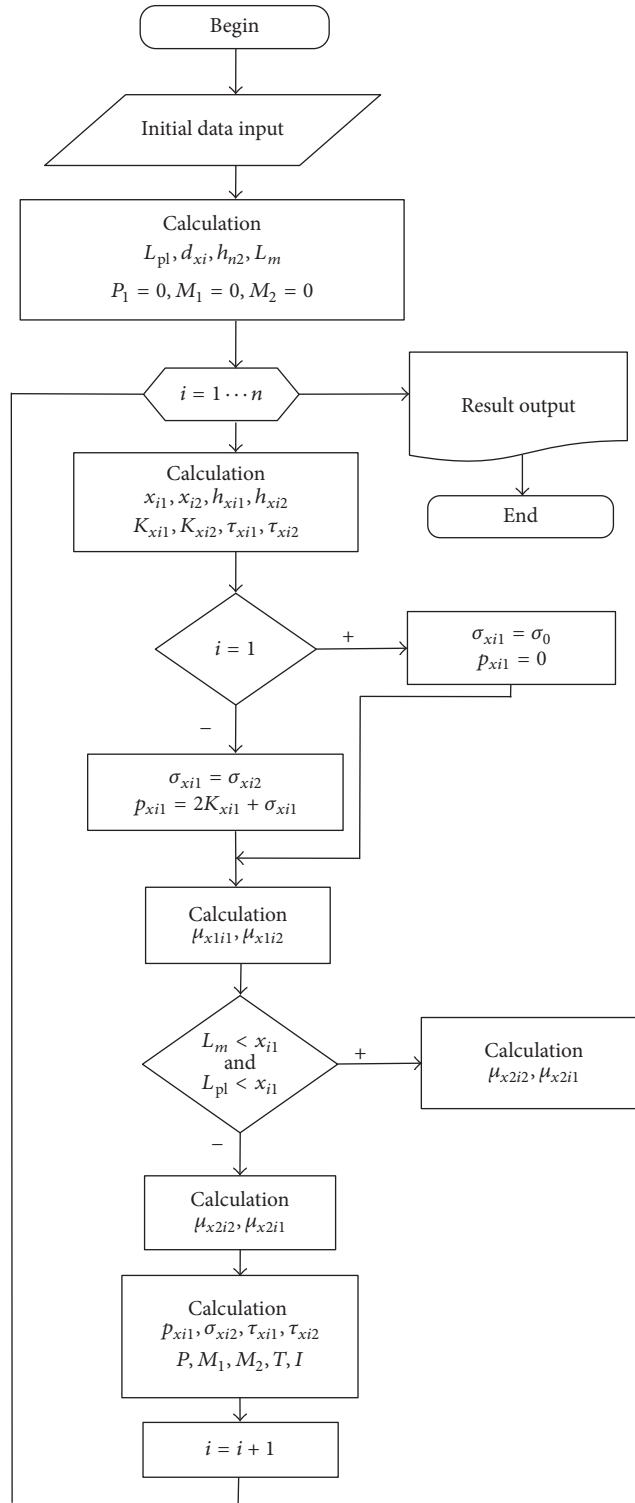


FIGURE 3: The aggregated block diagram of the algorithm for electric contact surfacing by the compact material.

layer. The durability of the restored part directly depends on the adhesive strength of the coating to the part. Because of the low adhesive strength, there is exfoliation of the deposited layer during operation. Therefore, the development of the technological scheme to improve the adhesive strength of the

coating is the actual task, which allows providing the forming of the high quality coating.

The important characteristic of electric contact surfacing is the short duration of the heat process. Therefore, the desired thickness of the deposited layer and the high adhesive

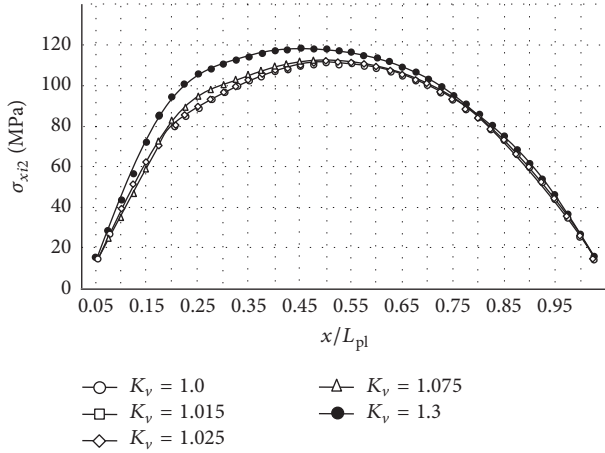


FIGURE 4: The calculated distributions of normal contact stresses along the zone of the surfacing, depending on the speed asymmetry coefficient (the initial thickness of compact material is 0.5 mm).

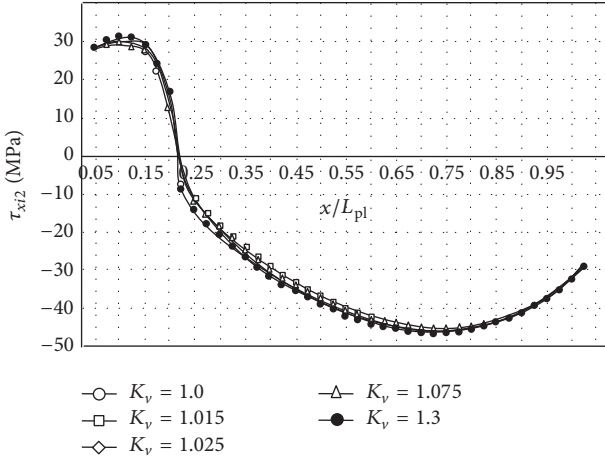


FIGURE 5: The calculated distributions of tangential contact stresses on the roller electrode along the zone of the surfacing, depending on the speed asymmetry coefficient (the initial thickness of the compact material is 0.5 mm).

strength of bond by controlling the technological modes of electric-welding process are very important. One of the widely known methods of the bond strength of the coating improving is intensification of the electric contact surfacing by increasing the friction coefficient in the zone of contact of part with compact material due to creation of opposite torque under a current pulse [21]. There is a significant influence on the friction coefficient changing in the zone of electric contact surfacing of the asymmetry of the process at the expense of the controlled changing of kinematic (the rotation speed of the roller electrode and the part), tribological (changing of the friction coefficient, caused by the differences of the roughness of the surfaces), and physical and mechanical (changing of the temperature along the thermal deformation zone) properties. The ratio of linear speeds between the roller electrode and the detail is the most effective method

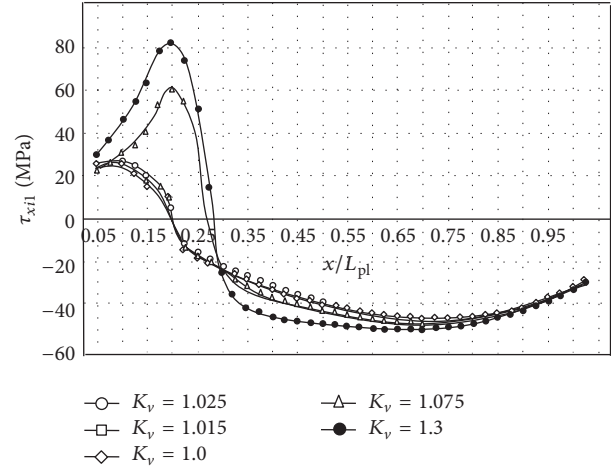


FIGURE 6: The calculated distributions of tangential contact stresses on the detail along the zone of surfacing, depending on the speed asymmetry coefficient (the initial thickness of the compact material is 0.5 mm).

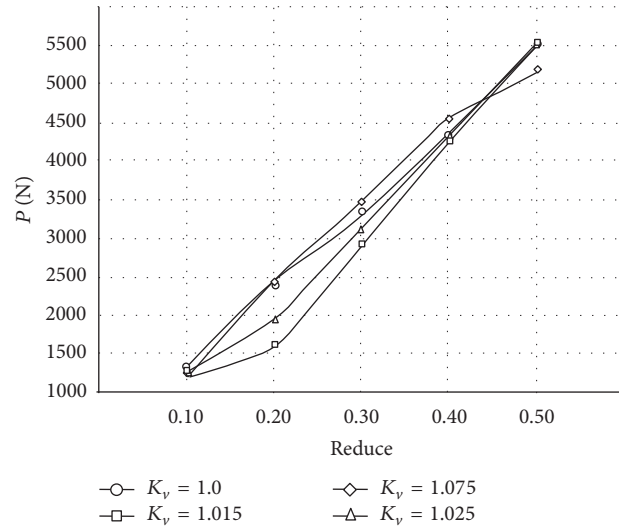


FIGURE 7: The calculated distributions of forces on the roller electrode, depending on the reduce and the speed asymmetry coefficient (the initial thickness of the compact material is 0.5 mm).

to manage the asymmetry factor allowing for increasing the friction coefficient.

The theoretical researches were conducted at various values of the speed asymmetry factor ($K_v = 1.0 \dots 1.075$) and also at various values of reduce ($\varepsilon = 0.10 \dots 0.60$) during the electric contact surfacing. The calculated distributions of the local and integral characteristics of the electric contact surfacing process are received. Presented graphic dependencies (Figures 4–10) show the influence of the asymmetry factor K_v on the coating forming. To ensure the optimal forming of the coating, it is necessary to create the kinematic asymmetry coefficient K_v , for increasing the tangential contact stresses in the zone of contact between the part and compact material.

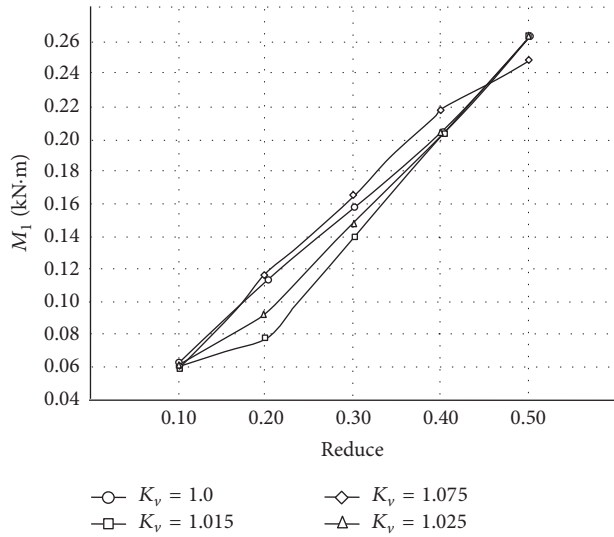


FIGURE 8: The calculated distributions of the moment on the detail, depending on the reduce and the speed asymmetry coefficient (the initial thickness of compact material is 0.5 mm).

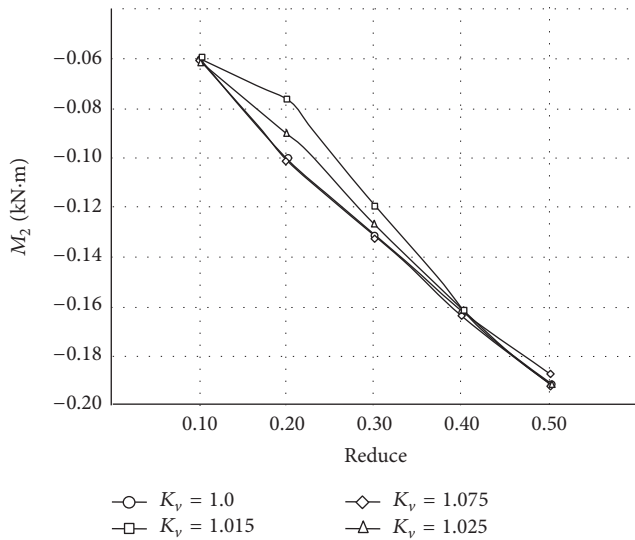


FIGURE 9: The calculated distributions of the moment on the roller electrode, depending on the reduce and the speed asymmetry coefficient (the initial thickness of compact material is 0.5 mm).

From the diagram (Figure 6), it is clear that maximum tangential stresses and hence the maximum friction coefficient in the zone of the electric contact surfacing are observed at $K_v = 1.3$. At equality of the linear rates of roller electrode and cylindrical part, in the absence of asymmetry in the process of electric contact surfacing, tangential stresses on the roller electrode and on the product are equal. Increase of K_v leads to the increase of the tangential contact stresses in surfacing zone. Herewith, the friction coefficient on the roller electrode does not change significantly (Figure 5). Because the tangential contact stresses change their value depending on the metal flow direction, the most favorable conditions for the formation of functional layer are observed in the presence

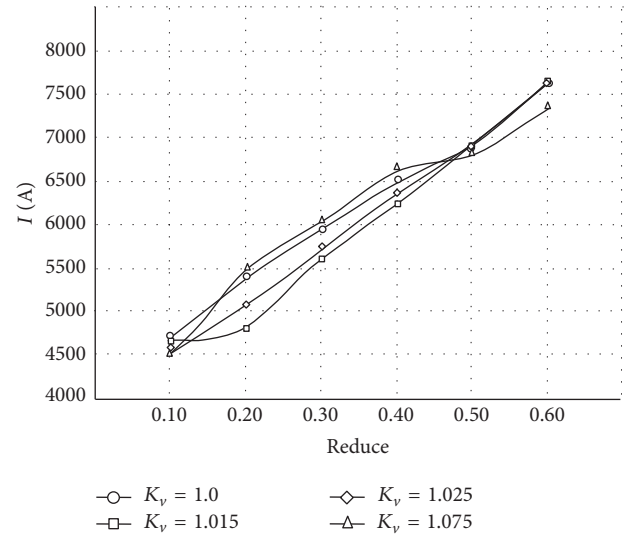


FIGURE 10: The calculated distributions of the current pulse, depending on the reduce and the speed asymmetry coefficient (the initial thickness of compact material is 0.5 mm).

of kinematic asymmetry in the process of electric contact surfacing (Figure 6). The areas with the maximum normal contact stresses (Figure 4) match the zero values of the tangential contact stresses (Figure 6). However, the impact of the asymmetry factor on the technological parameters is ambiguous. Figures 7–9 show that with the increasing of kinematic asymmetry coefficient the force on the roller electrode necessary to form surface layer of a given thickness on the product and the moment on the roller electrode parameters depending on the size of the recoverable parts and on the thickness of the coating are changed. Besides, at the $K_v = 1.015$ – 1.025 , the effort on the roller electrode and moments M_1 and M_2 are decreased, but increasing the value 1.075, there is the rise in energy-power parameters. Such consistent pattern is traced for the all graphic dependencies (Figures 7–9) in the range of values of reduce from 0.15 to 0.45. At reduce of more than 0.45, the asymmetry factor $K_v = 1.015 \dots 1.025$ does not affect the energy-power parameters' changing. Since the impact of the energy-power and operating thermal parameters is simultaneous, the aforesaid consistent pattern is typical also for the dependence of current pulse on the reduce (Figure 10). At the expense of the increasing of asymmetry factor (above $K_v = 1.075$), the values of the energy-power and thermal parameters are decreasing only at value of the reduce of more than 0.45. The application of such values of the reduce during the electric contact surfacing leads to significant structural changes of the compact material and also to forming the burnouts and splashes. Besides, the application of the high reduce provides forming of the indentations on the surface of coating, which significantly impairs the product appearance. The values of the reduce of $0.20 \dots 0.30$ are the most expedient for the conditions of the electric contact surfacing, which provides the forming of the coating with desired performance characteristics. Thus, the application of the speed asymmetry factor above 1.075 is inexpedient for the conditions of electric contact surfacing by compact material

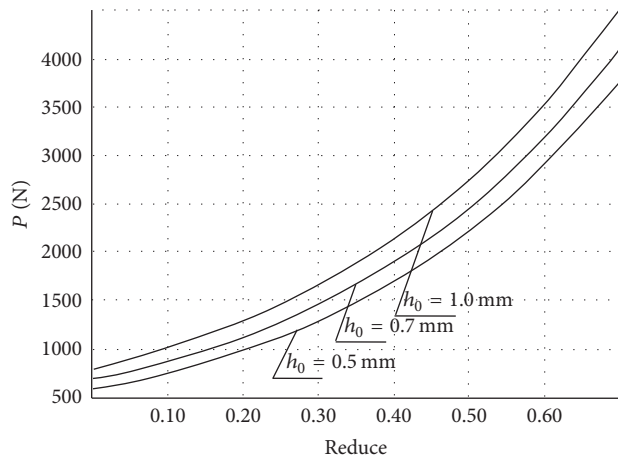


FIGURE 11: The results of automated design of the efforts on the roller electrode, depending on reduce. $R_l = 50$ mm; $a_1 = 0.124$; $a_2 = 0.052$; $a_3 = -3.70$; $\sigma_{r0} = 60.1$ N/mm²; $\lambda = 0.26$.

with reduce of $0.15 \dots 0.30$ because of increasing of the energy intensity of the process.

So, the most rational in terms of the quality of the coating is the asymmetrical electric contact surfacing process with speed asymmetry of not more than 1.015. This allows providing the increase of the friction coefficient in the surfacing zone without the increase of the energy and power parameters. Reduction of the integral characteristics of the process allows repairing big sized parts with the lowest thermal and mechanical impact. This minimizes the structure changes of the functional coating and the surface layer of main metal. On the basis of the developed software, the calculation of the main technological process parameters was made (Figures 11 and 12). From a practical point of view, the results of the automated design of technological modes of electric contact surfacing by the compact material allow identifying all the initial parameters of the process to produce a specified thickness of the coating on the surface of the part.

4. Experimental Studies

The check of the adequacy of the obtained analytical descriptions of electric contact surfacing was done during restoring of the parts of "shaft" type made of steel St45 by continuous ribbon St45 on the electric machine of the seam type welding MSHP-150 with a rated power of the surfacing current 20 kA and a maximum compression force of 8 kN (Figure 13(a)).

Force measurement on the roller electrode was done with the help of load cells; also the measurement of the moments on the roller electrode and the detail was provided with the help of tensiometric sensor of resistance. Using the sliding strings of current collectors, the electrical signal from the rotating universal spindles was read. The calibration of the measuring instruments was performed by simulation of loading with the use of the cantilever arm and a set of cargos. Recording of registered parameters was produced by means of a PC with built-in analog-to-digital converter, providing the measuring ability at 16 differential channels. Input in this case is digitized by 16-bit analog-digital converter with

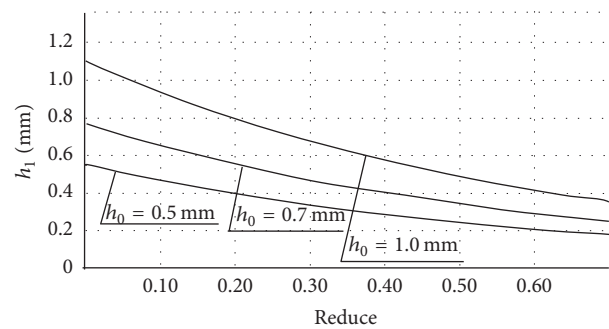


FIGURE 12: The results of automated design of the final thickness of the coating, depending on the reduce. $R_l = 50$ mm; $a_1 = 0.124$; $a_2 = 0.052$; $a_3 = -3.70$; $\sigma_{r0} = 60.1$ N/mm²; $\lambda = 0.26$.

a frequency of 100 kHz and a gain opportunity in the range of 1 to 1000. The oscillograms were recorded by a converter of voltage measuring E14-140 (Figure 13(b)). The converter is designed to perform tasks with feedback signals. Monitoring, recording, and analysis of the recorded data were done by the software Usb Oscilloscope (version 3.1.2.8) at a scale of 1:20; each oscillation is the time period of 0.02 s.

The control of geometric parameters of the initial compact materials and the received coating was carried out by a micrometer and caliper. The results of comparison of the calculated and experimental distributions of the efforts on the roller electrode are presented in the form of graphic dependence (Figures 14 and 15).

The integral characteristics of the process of electric contact surfacing by compact materials are determined in investigation. This allows making conclusion about sufficient convergence of experimental results and theoretical assumptions concerning process laws. The change of speed asymmetry factor is the perspective direction for control of the stress-strained state of compact material, which allows regulating the plastic deformation of the material process. The optimum conditions for forming of wearproof coating without lack of fusion can be obtained by changing the speed asymmetry factor which depends on rotational speed ratio of roller electrode and "shaft" type parts.

5. Discussion

The heavy operating conditions lead to fast deterioration of details durability. Increasing of technical and economic parameters of equipment is inextricably linked with increasing of service life of parts working in conditions of intense abrasive deterioration. Restoration of operability of worn equipment can be achieved by two ways: either changing of worn parts by new ones or building up of metal on worn surface until reaching the nominal sizes. The first way is less profitable from economic point of view because the expenses on spare parts can achieve 80% of initial cost of equipment. The electric contact surfacing by compact materials allows applying on the worn surface a coating of the specified thickness with the required operating characteristics. Use of this method allows solving effectively the problem of prolonging of service term of technological unit. The

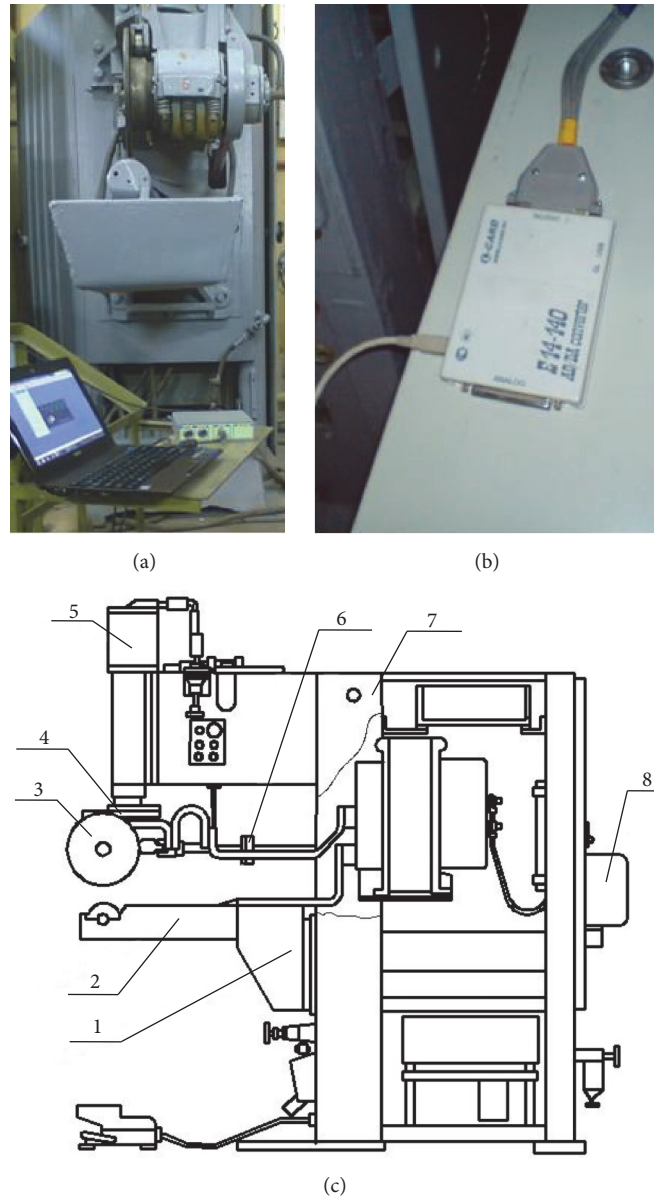


FIGURE 13: General view of the installation for experimental investigation (a, b), the basic scheme of equipment for electric contact surfacing (c) (1: bottom bracket, 2: cantilever, 3: roller electrode, 4: intermediate plate, 5: slider for drive efforts, 6: articulated shaft, 7: casing wall, and 8: the rotary drive).

method of electric contact surfacing is characterized by transience of intensely thermomechanical impact on the surfacing compact material. This allows obtaining coating on the surface of part without significant thermal influence on the base metal of part. This peculiarity of the process allows avoiding the structural changes of the base metal and preventing decreasing of its mechanical properties. However, the transience of current pulse confines the precision of quality prediction of the coating. The adhesive strength of the deposited coating is the most important quality indicator because at the low value of this parameter there is exfoliation of the coating during operation. The intensification of the surfacing process at the expense of increasing of the friction coefficient in zone of contact of part with compact material is an effective

method to improve the adhesive strength of the coating. The speed asymmetry factor has a great influence on increasing of friction coefficient in surfacing zone. The change of this parameter has a significant impact on stress-strain state of compact material in thermal deformation zone.

The influence of speed asymmetry factor on the local and integral characteristics of the process is considered in present work (Figures 4–9). The calculated distributions of normal contact stresses illustrate the behavior of material in a case of symmetric and asymmetric electric contact surfacing.

Increase of the speed asymmetry factor leads to change of stress-strain state of the compact material in thermal deformation zone. Increase of K_v above 1.3 provides also the significant increase of tangential contact stresses (maximum

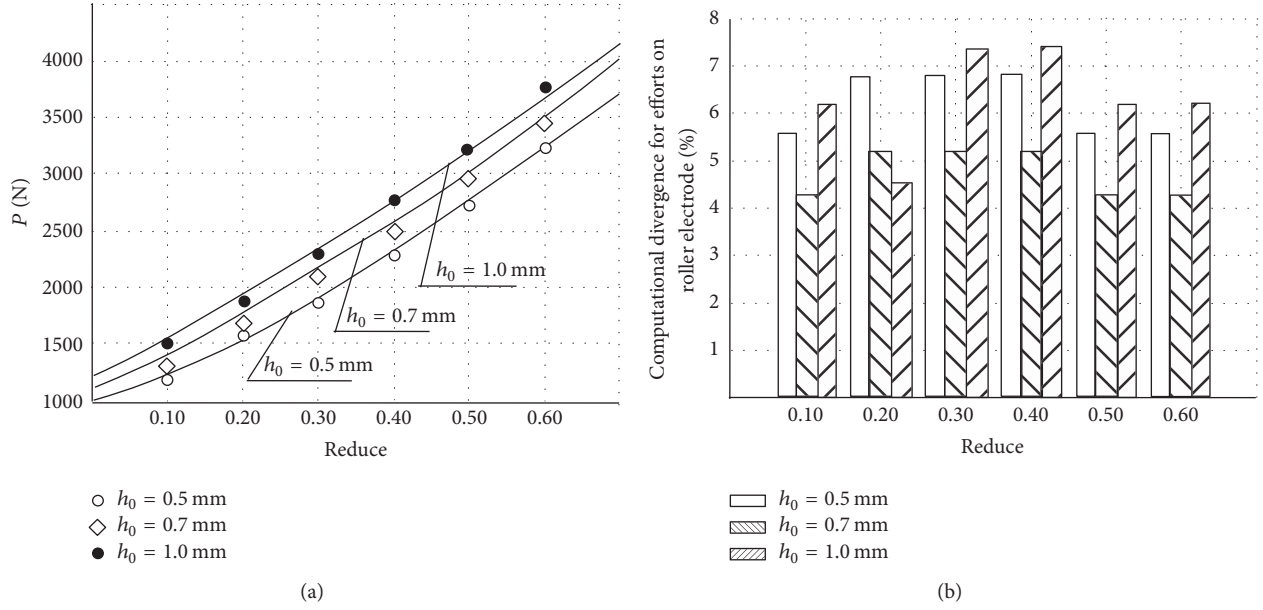


FIGURE 14: The calculated and the experimental distributions of the efforts on the roller electrode during the electric contact surfacing by the compact material. $RI = 50$ mm; $a_1 = 0.124$; $a_2 = 0.052$; $a_3 = -3.70$; $\sigma_{\tau 0} = 60.1$ N/mm²; $\lambda = 0.26$.

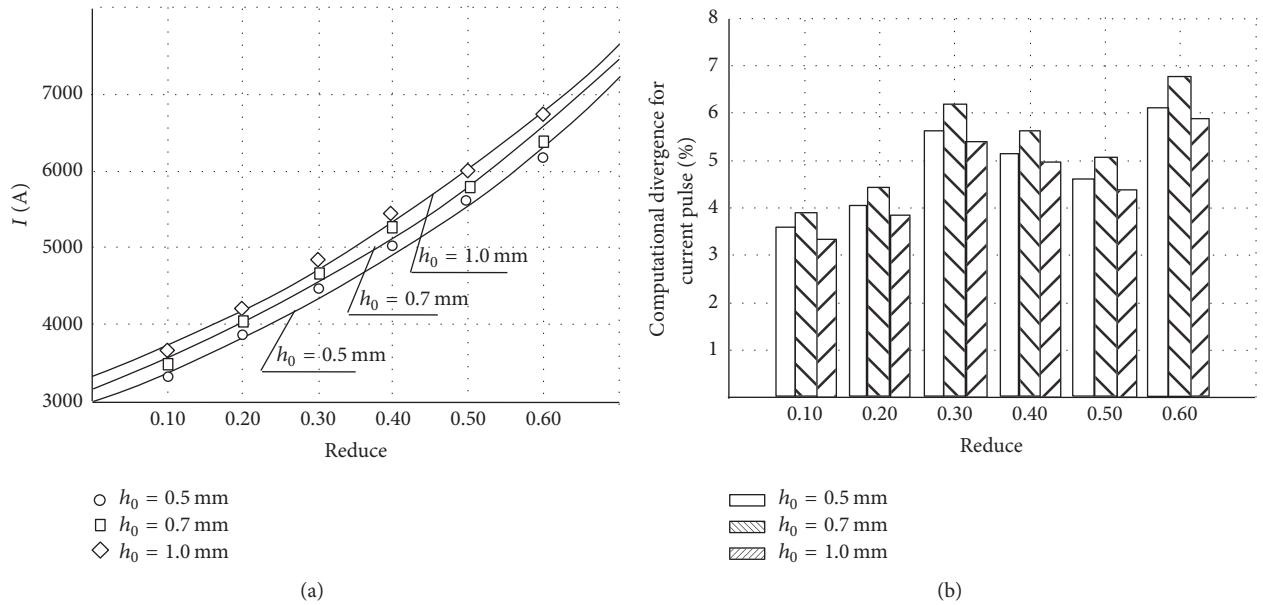


FIGURE 15: The calculated and the experimental distributions of the current pulse during the electric contact surfacing by the compact material. $RI = 50$ mm; $a_1 = 0.124$; $a_2 = 0.052$; $a_3 = -3.70$; $\sigma_{\tau 0} = 60.1$ N/mm²; $\lambda = 0.26$.

values of the tangential contact stresses $\tau_{xi1} = 83.7$ MPa at $K_v = 1.3$ and $\tau_{xi1} = 25.6$ MPa at $K_v = 1.0$). This allows increasing friction coefficient in surfacing zone, which leads to enhancement of the quality of the coating forming. The friction coefficient and the tangential contact stresses on the roller electrode practically do not change. Thus, adhesion between the compact material and the roller electrode does not occur. However, such an increase of the speed asymmetry

factor leads to increase of the energy and power parameters of the process. Increasing of the effort on the roller electrode occurs at $K_v = 1.075$ (for $\varepsilon = 0.30$ at $K_v = 1.0$, the effort on the roller electrode is about 3400 N; at $K_v = 1.015$, 3000 N; at $K_v = 1.075$, 3500 N). The regulation of the speed asymmetry factor allows for expanding the technological capabilities of equipment for electric contact surfacing whose limitations are associated with the size of

recoverable parts and application of high electromechanical powers.

The calculation of the main technological parameters of the process is received with application of developed software. Via developed software, the value of speed asymmetry factor was calculated, which allows increasing friction coefficient in thermal deformation zone. The nomograms for determination of the stress on the roller electrode (Figure 10) and the finite thickness of the coating (Figure 11) depending on the initial thickness of the compact material and deformation degree are presented. The automated design of technological process allows obtaining recommendations for selection of optimal operating parameters. The experimental verification of adequacy of the developed mathematical model which confirms satisfactory agreement of calculated data with experimental is performed.

Generally, the obtained results confirm that the variation of initial parameters of electric contact surfacing process of cylindrical parts is very important during the formation of power parameters, as well as during preparation of measures aimed at ensuring the stability of the surfacing process and improving the quality of the deposited layer with specified geometrical characteristics.

6. Conclusion

A mathematical model, which allows optimizing the technological parameters of electric contact surfacing by compact material of the “shaft” type parts, was developed. As a result of numerical implementation of the developed model, it was found that a significant effect on the change of power parameters of the process was made by the ratio of roller electrode and the “shaft” type parts speeds. It is established that the change of the speed asymmetry factor has a significant influence on the forming of the coating because of the increasing of the friction coefficient. It is proved that the application of the asymmetric process of electric contact surfacing allows decreasing the thermomechanical impact on the compact material in surfacing zone. This considerably expanded the capabilities of the equipment and allows reducing the thermomechanical influence on the base metal of the parts. Obtained graphic dependences allow determining the initial parameters of the process such as the amperage, stress on the roller electrode, and the initial thickness of the compact material, depending on the required characteristics of the coating before the beginning of the process of electric contact surfacing.

Nomenclature

x_{i1}, x_{i2} :	Geometric coordinates of initial and finite boundary section of selected elementary volume
V_2, V_1 :	Rotational speed of roller electrode and part
R_{b2}, R_{b1} :	Radius of roller electrode and part
L_{pl} :	Length of the zone of the plastic deformation
L_m :	Length of the mixed zone

L_{lg2} :	Length of the zone of the lag on the roller electrode
Δx :	The value of the partition step of the plastic deformation zone
$2K_x$:	Current value of the double shift resistance of the compact material along the length of thermal deformation zone defined with considering of the current values of degree, velocity, and temperature of deformation
p_{x1}, p_{x2} :	Normal contact stresses on the roller electrode and on the part
h_{xi1}, h_{xi2} :	Current values of thickness of the coating along the length of selected elementary volume
h_0 :	Initial thickness of the compact material
h_1 :	Final thickness of the coating
h_{n2} :	Thickness of the compact material in the neutral section
a_h :	Exponent indicator of the real convex shape of the roller electrode
b :	Width of the roller electrode
P :	Stress on the roller electrode
M_1, M_2 :	Moment on the part and on the roller electrode
T_o :	The environment temperature
T_m :	The material temperature
a :	Coefficient of temperature conductivity
r :	The half of the thickness of compact material
$a_{\mu1}, a_{\mu2}$:	The exponent characterizing the distribution of the plastic friction coefficients on the contact surfaces of the part and the roller electrode
$Bi = \alpha r / \lambda$:	Biot criterion
$Fo = at / r^2$:	Fourier criterion
Pd :	Predvoditelev criterion
I :	The current pulse.

Greek Letters

τ_{x2}, τ_{x1} :	Tangential contact stresses on the roller electrode and on the part
σ_0 :	Rear tension stress of the compact material
σ_1 :	Normal axial stresses in the outlet of thermal deformation zone
μ_{x1}, μ_{x2} :	Current value of plastic friction coefficient
λ :	Coefficient of thermal conductivity
α :	Heat transfer coefficient.

Index

- i : The current ordinal number of the selected elementary volume along the length of the thermal deformation zone
- n : The number of partitions along the length of thermal deformation zone
- 1: The value at the entrance to the elementary volume of thermal deformation zone
- 2: The value at the output from an elementary volume of thermal deformation zone.

Disclosure

The submission of the authors' paper implies that it has not been previously published, that it is not under consideration for publication elsewhere, and that it will not be published elsewhere in the same form without the written permission of the editors.

Competing Interests

The authors Olena V. Berezshnaya, Eduard P. Gribkov, and Valeriy D. Kuznetsov declare that there is no conflict of interests regarding the publication of this paper.

Authors' Contributions

All authors participated in the design of this work equally. All authors read and approved the final manuscript.

References

- [1] L. Jin-Gui, "Surface hardening technologies and mouldsurvice life," *China Surface Engineering* 1, 2002.
- [2] L. Pawlowski, *The Science and Engineering of Thermal Spray Coatings*, John Wiley & Sons, New York, NY, USA, 2nd edition, 2008.
- [3] J. Winczek, G. Rygał, and T. Skrzypczak, "The model of temporary temperature field during multi-pass arc weld surfacing. Part I: analytical description," *Journal of Applied Mathematics and Computational Mechanics*, vol. 14, no. 2, pp. 123–130, 2015.
- [4] H.-J. Kim and Y. J. Kim, "Wear and corrosion resistance of PTA weld surfaced Ni and CO based alloy layers," *Surface Engineering*, vol. 15, no. 6, pp. 495–501, 1999.
- [5] J. Winczek, "Modelling of heat affected zone in cylindrical steel elements surfaced by welding," *Applied Mathematical Modelling*, vol. 36, no. 4, pp. 1514–1528, 2012.
- [6] C. Wallace, "Submerged arc welding method for steel sheets," Patent EP 2786829 A1, 2012.
- [7] Kh. N. Sagirov, D. Kh. Sagirov, S. D. Khachkinaev, S. K. Slitinskaya, N. G. Dyurgerov, and D. P. Perfil'ev, "Efficient process of automatic submerged-arc surfacing," *Welding International*, vol. 18, no. 2, pp. 121–123, 2004.
- [8] V. L. Kvanin, N. T. Balikhina, V. G. Karabakhin, and A. G. Merzhanov, "Deposition of protective coatings by combined SHS/argon-arc surfacing," *International Journal of Self-Propagating High-Temperature Synthesis*, vol. 20, no. 2, pp. 88–93, 2011.
- [9] V. V. Bulychov and V. V. Zezyulya, "Electrical resistance deposition with a wire and deceleration of the roller electrode," *Welding International*, vol. 25, no. 5, pp. 374–377, 2011.
- [10] R. N. Saifullin and V. S. Natalenko, "A method of production of sintered strips by electric resistance rolling," *Welding International*, vol. 25, no. 3, pp. 205–208, 2011.
- [11] P. I. Burak, A. V. Serov, and R. A. Latypov, "Optimization of the process of electric resistance welding of metallic strips through an amorphous solder," *Welding International*, vol. 26, no. 10, pp. 814–818, 2012.
- [12] M. V. Storozhev and E. A. Popov, *Theory of Metal Forming: A Textbook for High Schools*, Mashinostroenie, 1977.
- [13] E. P. Gribkov, A. V. Perig, and V. A. Danilyuk, "Research into the process of producing powder tapes," *International Journal of Advanced Manufacturing Technology*, vol. 77, no. 5–8, pp. 1087–1104, 2015.
- [14] O. V. Berezshnaya and E. P. Gribkov, "Matematicheskoe modelirovanie formobrazovaniya sloya pri electrokontaktnoi naplavke provolokoi detalei tipa 'val'," *Visnik of the Volodymyr Dahl East Ukrainian National University*, vol. 6, no. 213, pp. 93–96, 2014 (Russian).
- [15] C. Bartuli, T. Valente, and M. Tului, "Plasma spray deposition and high temperature characterization of ZrB₂-SiC protective coatings," *Surface and Coatings Technology*, vol. 155, no. 2-3, pp. 260–273, 2002.
- [16] R. N. Saifullin, "Improvement of performance of machine parts by electrocontact welding of composite materials," *Journal of Friction and Wear*, vol. 28, no. 2, pp. 206–211, 2007.
- [17] A. D. Koval', V. G. Efremenko, M. N. Brykov, M. I. Andrushchenko, R. A. Kulikovskii, and A. V. Efremenko, "Principles for developing grinding media with increased wear resistance. Part I. Abrasive wear resistance of iron-based alloys," *Journal of Friction and Wear*, vol. 33, no. 1, pp. 39–46, 2012.
- [18] R. N. Saifullin, "Improvement of performance of machine parts by electrocontact welding of composite materials," *Journal of Friction and Wear*, vol. 28, no. 2, pp. 206–211, 2007.
- [19] K. D. Voskresenskiy, *Sbornik Raschetov I Zadach Po Teploperedache*, Collection of Calculations and Heat Transfer Problems, Ripol Classic, 2013 (Russian).
- [20] A. I. Veinik, *Priblizhennyj Raschet Protsessov Teploprovodnosti*, Ripol Classic, 2013 (Russian).
- [21] V. V. Zezulia and V. V. Booluchev, "Method of electric contact surfacing," Patent RU 2466000, 2012 (Russian).

Review Article

Inverse Strategies for Identifying the Parameters of Constitutive Laws of Metal Sheets

P. A. Prates, A. F. G. Pereira, N. A. Sakharova, M. C. Oliveira, and J. V. Fernandes

CEMUC, Department of Mechanical Engineering, University of Coimbra, Rua Luís Reis Santos, Pinhal de Marrocos, 3030-788 Coimbra, Portugal

Correspondence should be addressed to P. A. Prates; pedro.prates@dem.uc.pt

Received 1 July 2016; Accepted 16 August 2016

Academic Editor: Sutasn Thipprakmas

Copyright © 2016 P. A. Prates et al. This is an open access article distributed under the Creative Commons Attribution License, which permits unrestricted use, distribution, and reproduction in any medium, provided the original work is properly cited.

This article is a review regarding recently developed inverse strategies coupled with finite element simulations for the identification of the parameters of constitutive laws that describe the plastic behaviour of metal sheets. It highlights that the identification procedure is dictated by the loading conditions, the geometry of the sample, the type of experimental results selected for the analysis, the cost function, and optimization algorithm used. Also, the type of constitutive law (isotropic and/or kinematic hardening laws and/or anisotropic yield criterion), whose parameters are intended to be identified, affects the whole identification procedure.

1. Introduction

Finite Element Analysis (FEA) is now a well-established computational tool in industry for the optimization of sheet metal forming processes. The accurate modelling of these processes is a complex task due to the nonlinearities involved, such as those associated with (i) the kinematics of large deformations, (ii) the contact between the sheet and the tools, and (iii) the plastic behaviour of the metal sheet.

The description of the plastic behaviour of metal sheets is usually performed using phenomenological constitutive models. In this context, the emergence of new steels and aluminium, magnesium, and other alloys, as well as their increasingly widespread use in the automotive and aeronautical industries, has encouraged the development of more reliable models, with increasing flexibility associated with a larger number of parameters to identify [1–14]. In fact, the accuracy of the numerical simulation results of sheet metal forming processes depends on the flexibility of a constitutive material model but also on the procedure adopted to identify its parameters. The complex nature of the plastic behaviour of metal sheets makes their characterization dependent upon factors such as (i) the constitutive model; (ii) the experimental tests performed, comprising the sample geometry, the testing conditions, and the analysis methodologies; (iii) the strategy for identifying the constitutive parameters.

The strategy for identifying the model parameters is generally seen as an optimization problem, where the purpose is to minimise the difference between computed and experimental results of one or more experiments. Two main types of strategies for the identification of the constitutive parameters can be recognised in literature: classical and inverse strategies. The classical identification strategies for the constitutive parameters make use of a large number of standardised mechanical tests, with well-defined geometry and loading conditions, such that homogeneous stress and strain distribution develop in the region of interest (e.g., [15, 16]); nonstandard mechanical tests can also be performed to properly describe other biaxial stress states in the sheet plane (e.g., [17, 18]). However, sheet metal forming processes are carried out under strongly nonhomogeneous stresses and strains fields. Therefore, limiting the characterization of the mechanical behaviour of metal sheets to a restricted number of tests with linear strain paths and homogeneous deformation can lead to a somewhat incomplete characterization of the overall plastic behaviour of the material [19].

Recent developments and accessibility of optical full-field measurement techniques, such as digital image correlation (DIC) technique coupled with FEA, make the inverse identification strategies a common current place. The full-field measurements allow the acquisition of enriched information from mechanical tests, such as displacement and strain fields;

an overview on this topic can be found in [20]. This allows attenuating the constraints on the geometry and loading conditions of the mechanical tests used for the identification of materials parameters, so that nonhomogeneous stress and strain distributions can be developed in the region of interest (e.g., [21–29]). In this sense, the identification of constitutive parameters from nonhomogeneous strain fields and complex loading conditions provides a more reliable description of the material behaviour during real sheet metal forming processes [21]. In such complex mechanical tests, it is no longer possible to identify the constitutive parameters based on simple assumptions on the stress and/or strain states, as in the classical identification strategies. Instead, a finite element model of the mechanical test is established and cost functions are defined to minimise the gap between numerical and experimental results of the mechanical test, which demands efficient optimization algorithms. However, the efficiency of any inverse identification strategy directly depends on the information contained by the objective function. In the context of constitutive parameters identification, this is related to the type of experimental results included (e.g., loads, displacements, and strains) but also to the strain paths and levels of deformation attained by the experimental test. It turns out that there is no consensus about the experimental tests (sample geometry and loading conditions), the cost functions, and the optimization procedure that will lead to accurate constitutive parameters identification. Also, a major obstacle to the widespread use of advanced constitutive models in industrial simulations seems to result from the lack of an efficient strategy for parameters identification. In this sense, the developed strategy must be simple, from an experimental point of view, and allow evaluating to what extent the selected constitutive model allows perfectly describing the behaviour of a given material.

The present paper describes recent inverse strategies coupled with FE simulations for the identification of the parameters of constitutive laws that describe the plastic behaviour of metal sheets, resorting to mechanical tests leading to nonuniform strain and stress states. Following this introduction, the paper addresses general concepts for the constitutive modelling and the optimization problem. Afterwards, an overview of inverse identification strategies for the constitutive parameters is presented, with emphasis on inverse identification strategies resorting to FE simulations.

2. Constitutive Modelling

Constitutive models have been developed to predict the onset and evolution of the plastic deformation of a deformable body undergoing a general state of stress. A phenomenological constitutive model is typically a combination of the following components:

- (i) Yield criterion that describes the yield surface of the material in a multidimensional stress space: The metal sheets are usually assumed to be orthotropic, with invariant anisotropy during plastic deformation. With high incidence in the last decades, the emergence of anisotropic yield criteria with an increasing

number of material parameters has been witnessed. They provide the flexibility required for accurately modelling the plastic behaviour of advanced metallic alloys, which are frequently used in automotive and aeronautical industries. Several approaches have been used for deriving yield criteria, based on

- (1) high-order polynomial functions (e.g., [1, 2]);
- (2) the generalization to anisotropy of the second and third invariants of the deviatoric stress tensor, J_2 and J_3 , respectively (e.g., [3]);
- (3) one or more isotropic yield functions, using the linear Isotropic Plasticity Equivalent (IPE) stress space concept (e.g., [3–9]);
- (4) the construction of weighted sums of anisotropic yield criteria (e.g., [7]);
- (5) the capability to model the tension-compression asymmetry, particularly devoted to specific magnesium and titanium alloys (e.g., [3, 6, 10]);
- (6) the capability to model kinematic hardening [11];
- (7) the interpolation of second-order Bézier curves [12].

- (ii) Hardening laws that express the evolution of the yield surface during plastic deformation, as schematized in Figure 1: The isotropic hardening law refers to the homothetic expansion of the yield surface (see Figure 1(a)) while the kinematic hardening law describes its translation in the stress space (see Figure 1(b)). Kinematic hardening laws are recommended for describing plastic deformation under strain path changes, mainly strain path reversal, in materials that exhibit Bauschinger effect (e.g., [14]). The combination of isotropic and kinematic hardening laws provides a flexible model, for simultaneously describing the change in size and the position of the centre of the yield surface, during plastic deformation. Isotropic hardening laws described by power laws (e.g., [32–37]), saturation laws (e.g., [38, 39]), and weighted combinations of isotropic hardening laws (e.g., [40, 41]) have been proposed. Linear (e.g., [42, 43]) and nonlinear (e.g., [13, 14, 44–47]) kinematic hardening laws were proposed, with the latter being more appropriate to describe the Bauschinger effect.
- (iii) Flow rule, to establish a relationship between the stress state and the plastic strain increment: Typically, an associated flow rule is adopted, that is, using the yield function as plastic potential, although some exceptions can be found in literature (see, e.g., [48]).

The general representation of a constitutive model can be described through a function $\mathcal{F} = \mathcal{F}(\boldsymbol{\sigma}' - \mathbf{X}', \bar{\varepsilon}^p, \alpha, \beta)$:

$$\mathcal{F}(\boldsymbol{\sigma}' - \mathbf{X}', \bar{\varepsilon}^p, \alpha, \beta) = \bar{\sigma}(\boldsymbol{\sigma}' - \mathbf{X}', \alpha) - Y(\bar{\varepsilon}^p, \beta), \quad (1)$$

where $\bar{\sigma}(\boldsymbol{\sigma}' - \mathbf{X}', \alpha)$ is the equivalent stress defined by a given yield criterion and $Y(\bar{\varepsilon}^p, \beta)$ is the hardening law

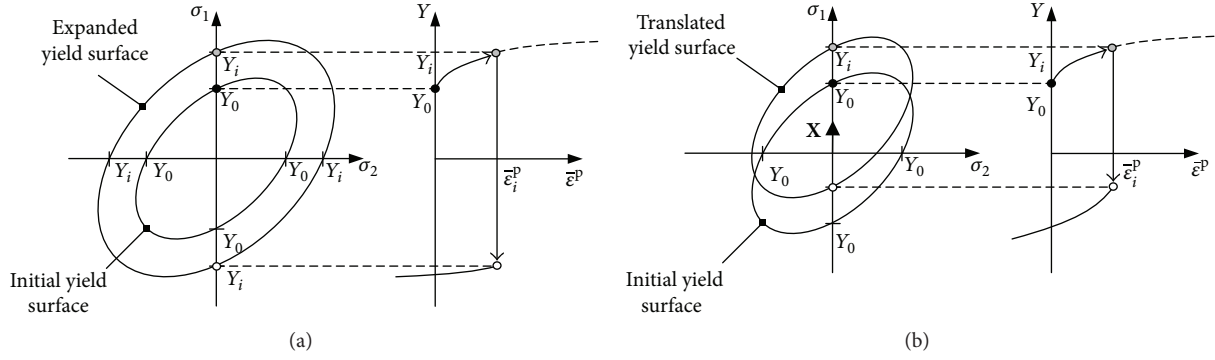


FIGURE 1: Representation of the plastic behaviour of materials in tension-compression. The left side shows generic yield surfaces in the plane $(\sigma_1; \sigma_2)$ and the right side shows the corresponding hardening law: (a) isotropic hardening and (b) kinematic hardening. See text for details. Adapted from [30].

that represents the evolution of the yield stress during the deformation. The equivalent stress, $\bar{\sigma}(\boldsymbol{\sigma}' - \mathbf{X}', \alpha) = \bar{\sigma}$, is a function of the effective stress tensor, $(\boldsymbol{\sigma}' - \mathbf{X}')$, that includes the parameters of the yield criterion, α , for describing the anisotropy ($\boldsymbol{\sigma}'$ and \mathbf{X}' are the deviatoric Cauchy stress and the deviatoric backstress tensors, resp.) and $Y(\bar{\epsilon}^p, \beta) = Y$ is a function of the equivalent plastic strain, $\bar{\epsilon}^p$, in which the parameters are represented by β . The yielding is defined based on the function \mathcal{F} of (1) and can be written as follows:

$$\begin{aligned} \mathcal{F} &= \bar{\sigma} - Y = 0 \implies \\ \bar{\sigma} &= Y. \end{aligned} \quad (2)$$

If $\bar{\sigma} < Y$, the stress state of the material remains inside the yield surface and only elastic deformation occurs. When plastic deformation occurs, the associated flow rule states that the increment of the plastic strain tensor is normal to the yield surface, for a stress state such that $\bar{\sigma} = Y$. The normality condition, defined by the associated flow rule, assumes that the increment of the plastic strain tensor is normal to the yield surface and is expressed by

$$d\boldsymbol{\epsilon}^p = d\lambda \frac{\partial \bar{\sigma}(\boldsymbol{\sigma}' - \mathbf{X}')}{\partial (\boldsymbol{\sigma}' - \mathbf{X}')}, \quad (3)$$

where $d\boldsymbol{\epsilon}^p$ is the increment of the plastic strain tensor, $d\lambda$ is a scalar multiplier, and $\bar{\sigma}(\boldsymbol{\sigma}' - \mathbf{X}') = \bar{\sigma}$ is the equivalent stress function, representing the plastic potential.

Even though a number of advanced constitutive models are available in literature, sheet metal forming simulations are still mostly performed in industry not taking into account kinematic hardening and with the well-known Hill'48 yield criterion [49], whose parameters identification can be easily assessed by uniaxial tensile tests. Mattiasson and Sigvant [50] mentioned some plausible explanations, still valid today, for this reality:

- (i) The relative simplicity of the Hill'48 model that makes it attractive to use
- (ii) The unavailability of industry analysts for understanding to what extent the modelling of the material influences the simulation results

- (iii) The lack of knowledge, time, and money for performing the multiaxial tests required to identify reliable hardening curves and parameters of advanced yield criteria
- (iv) The additional cost in terms of CPU time for using more advanced constitutive models which is considered to be an effort that is not worth it.

Nevertheless, in our view, the major obstacle to the widespread use of advanced constitutive models in industrial simulations comes from the large number of linear strain path tests, including multiaxial tests, required for the parameters identification. To overcome this barrier, a potential approach is to look for new constitutive parameters identification strategies that are alternative to the classical ones. In this sense, an accurate description of the material plastic behaviour could be attained from (i) a minimum number of mechanical tests and experimental data; (ii) flexible and user-friendly constitutive models; and (iii) an accessible identification procedure for the constitutive parameters, coupled with robust optimization algorithms. Therefore, Section 4 will discuss some identification procedures for the constitutive parameters based on inverse analysis, as an alternative to the classical approaches.

3. The Optimization Problem

The inverse identification of constitutive model parameters is generally seen as an optimization problem. The purpose is to minimise the difference between computed and experimental results of one or more experiments. This difference is expressed by a cost function and its minimisation is performed using optimization algorithms, which automatically operate on the values of the constitutive parameters.

3.1. Cost Function. A wide number of cost function formulations for the identification of constitutive parameters have been proposed in literature (e.g., [57, 58]). According to Cao and Lin [57], the cost function should operate as an "efficient guide" of the optimization procedure, in order to search for

the best fit to the experimental results; therefore, the ideal cost function should comprise the following conditions:

- (i) All measured points of a given experiment should be part of the optimization procedure and have equal opportunity to be optimized, provided that experimental errors are eliminated.
- (ii) All experiments should have equal opportunity to be equally optimized, and so the optimization should not depend on the number of points considered in each experiment.
- (iii) Different units of measure in the cost function should not affect the performance of the optimization.
- (iv) The identification procedure should not be dependent of the user, and so the values of the weighting factors should be optimized to achieve the abovementioned conditions.

Cost functions are typically formulated under the concept of weighted least-squares, as follows:

$$F(\mathbf{A}) = \frac{1}{m} \frac{1}{n} \sum_{i=1}^m w_i \sum_{j=1}^n w_j [r_{ij}(\mathbf{A})]^2, \quad (4)$$

where $F(\mathbf{A})$ is the cost function to minimise; \mathbf{A} is the vector of constitutive parameters to optimize; m is the total number of experiments and n is the total number of points, considered in each experiment i ; $r_{ij}(\mathbf{A})$ is the residual between the numerically predicted results and those of the experiment i at point j ; w_i and w_j are the weighting factors for each experiment i and for each point j , respectively. Within the context of inverse parameter identification, $r_{ij}(\mathbf{A})$ can contain variables such as loads, pressures, angular moments, or those arising from full-field measurements (displacements or strains), as will be seen in detail later.

The residuals can be expressed in terms of relative differences,

$$r_{ij}(\mathbf{A}) = \frac{u_{ij}^{\text{Num}}(\mathbf{A}) - u_{ij}^{\text{Exp}}}{u_{ij}^{\text{Exp}}}, \quad (5)$$

with $i = 1, \dots, m$, $j = 1, \dots, n$,

or in terms of absolute differences,

$$r_{ij}(\mathbf{A}) = u_{ij}^{\text{Num}}(\mathbf{A}) - u_{ij}^{\text{Exp}}, \quad (6)$$

where u_{ij}^{Num} and u_{ij}^{Exp} are, respectively, the numerically predicted and the experimental results at point j of experiment i . Residuals are often expressed using relative differences, which allows the use, in the same cost function, of several kinds of quantities exhibiting various orders of magnitude and units of measure [59]. When u_{ij}^{Exp} admits values close to or equal to zero, the residuals should be expressed using absolute differences.

3.2. Optimization Algorithms. The minimization of the least-squares cost function, presented in (4), requires efficient and robust optimization algorithms, due to the strongly nonlinear nature of the least-squares cost function [60]. For this purpose, several optimization algorithms are described in the literature, which are commonly divided into two categories: gradient-free algorithms and gradient-based algorithms. Hybrid optimization strategies using both gradient-free and gradient-based algorithms are also proposed (e.g., [15, 60]).

Gradient-free algorithms, such as evolutionary and SIMPLEX algorithms, have a great probability of achieving a global minimum due to their random search capability. They require a large number of cost function evaluations (i.e., iterations) and therefore the convergence can be very time-consuming. Because of this, gradient-free algorithms are not recommended within the context of inverse identification strategies, since they require a large number of finite element simulations and analyses [61].

Gradient-based algorithms are most popular within inverse identification strategies, as they require far less cost function evaluations than gradient-free algorithms. As local optimizers, these algorithms use information of the gradient to update the vector of constitutive parameters in an adequate search direction [62]. Therefore, there is no guarantee that these algorithms converge to the global minimum, with the possibility of converging to undesirable local minima. This makes the optimization procedure dependent on the initial estimate for the parameters, and therefore the choice of convenient initial estimates for the constitutive parameters can be essential.

Examples of gradient-based algorithms commonly used within the context of inverse identification strategies are the Gauss-Newton and Levenberg-Marquardt algorithms. The Gauss-Newton algorithm is described as follows:

$$\mathbf{A}^{s+1} = \mathbf{A}^s - (\mathbf{J}^T \mathbf{W} \mathbf{J})^{-1} \mathbf{J}^T \mathbf{W} \mathbf{r}(\mathbf{A}^s), \quad (7)$$

where s is the iteration step, \mathbf{A} is the vector of constitutive parameters, \mathbf{W} is the vector of weighting factors, \mathbf{J} is the Jacobian matrix that expresses the sensitivity of the computed results to the constitutive parameters, and $\mathbf{r}(\mathbf{A}^s)$ is the vector of residuals, which can be expressed in terms of relative or absolute differences (see (5) and (6), resp.). The dimension of the vector of residuals depends on the total number of experiments m and the total number of points n , in each experiment, that is, the dimension $n_r = m \times n$. Considering that the total number of constitutive parameters to be identified is n_p , with $n_r \geq n_p$, the Jacobian containing the partial derivatives of the residuals with respect to the constitutive parameters is defined:

$$J_{l,p} = \frac{\partial r_l(A_p)}{\partial A_p}, \quad \text{with } l = 1, \dots, n_r, \quad p = 1, \dots, n_p. \quad (8)$$

An efficient method to compute the Jacobian matrix is finite differentiation. In order to improve convergence, the Jacobian matrix must be updated at each iteration step s . However, the calculation in each step requires high computational cost (at

least one numerical simulation per constitutive parameter). To overcome this inconvenient, Endelt et al. [63, 64] and Cooreman [62] highlighted the possibility of computing the sensitivity matrix analytically, with the latter author having concluded the inability of this approach for computing the sensitivities of strain fields to the material parameters, in mechanical tests involving complex and/or heterogeneous deformation.

In some cases, the Gauss-Newton algorithm can become unstable in the neighbourhood of the minimum, and so a stabilisation procedure is required. The Levenberg-Marquardt algorithm is similar to Gauss-Newton one, but includes a stabilising term, as follows [65]:

$$\mathbf{A}^{s+1} = \mathbf{A}^s - \left(\mathbf{J}^T \mathbf{W} \mathbf{J} + \lambda \text{diag}(\mathbf{J}^T \mathbf{W} \mathbf{J}) \right)^{-1} \mathbf{J}^T \mathbf{W} \mathbf{r}(\mathbf{A}^s), \quad (9)$$

where λ is the stabilising parameter that is updated in each iteration according to the convergence rate [65]. When the Levenberg-Marquardt method shows stability, small values for λ are recommended for fast convergence; otherwise, large values of λ usually allow stable convergence, although slower, towards the minimum. Note that for $\lambda = 0$ the Levenberg-Marquardt algorithm is equal to the Gauss-Newton one.

A different type of optimization technique that has been recently used in the identification of constitutive parameters is the Response Surface Methodology (RSM) (e.g., [54, 66]). RSM is an optimization technique for generating smooth approximations of complex functions in a multidimensional design space. In the context of parameter identification, the design space contains all possible combinations for the constitutive parameters and related values of the cost function. The prohibitive size of the full design space requires a Design of Experiments (DoE), to efficiently construct an approximated design space from a few number of representative points (i.e., sets of constitutive parameters). The responses of the representative points (i.e., the values of the cost function) are used to fit a response surface, which is typically obtained from second-order polynomial regression, for the sake of simplicity. Finally, the minimum of the response surface is calculated using a gradient-based optimization procedure, which leads to an estimate of the optimal set of constitutive parameters. In brief, the RSM technique can be summarised as follows:

- (1) An initial guess for the design space for the material parameters is selected.
- (2) Numerical simulations are performed with the different sets of parameters, representing the experimental design points needed for filling the design space.
- (3) For each simulation, the predicted results are compared with the experimental ones, and the cost function values are calculated according to (4).
- (4) A response surface is constructed to approximate the values of the cost function; typically, least-squares approximations are used to determine second-order polynomials.
- (5) An optimization algorithm is applied to determine the minimum point of the response surface (i.e.,

where $F(\mathbf{A})$ is minimum), providing the optimal set of material parameters.

If a converged solution is not found, the process starts all over again, adding a new region of interest to the design space.

4. Inverse Identification Strategies

While classical strategies make use of global measurements from experiments to infer the values of the constitutive parameters, using simple analytical relations to estimate the material response under the assumption of homogeneous stress and strain fields in the region of interest, the inverse identification strategies are much more flexible [20]. They make use of experiments allowing heterogeneous deformation and/or strain path changes, as close as possible of the conditions usually found during real sheet metal forming processes. In this perspective, some authors even proposed tests involving contact with friction, such as the punch stretch test (e.g., [67]) and the cylindrical cup test (e.g., [68]), for performing the inverse parameter identification. In these latter cases, the adequate description of the local contact with friction is of paramount importance because it can affect the final results of the parameter identification (e.g., see [69]).

The inverse identification strategies make use of global measurements, such as tool loads and tool displacements, which are usually coupled with local measurements, represented as full-field states of displacements and/or strains on the surface of the sample. Then, a numerical analysis of the mechanical test is performed, assuming a constitutive model chosen *a priori* and an initial estimate for its parameters. Finally, the experimental results of the mechanical test are iteratively compared with numerical results by acting on the values of the constitutive parameters until there is an adequate agreement between experimental and numerical results. Figure 2 shows a schematic representation of inverse identification strategies based on the comparison between experimental and numerical measurements using FE simulations.

The advantages of this identification approaches include substantial amount of reliable data extracted from a single mechanical test, using full-field measurements, which enables the accurate identification of large sets of constitutive parameters taking into account a wide range of strain levels and strain paths; therefore, it does not require uniform stress and strain distributions, in the region of interest, and no particular restrictions to the sample geometry and/or loading conditions are imposed.

Nevertheless, due to the design of the sample geometry, loading conditions, and induced strain paths, the inverse identification requires proper computational strategies [20]. The most common strategy uses Finite Element Model Updating (FEMU) and consists of performing successive finite element (FE) simulations of the physical experiment; the set of parameters are obtained by minimising the difference between the experimental and the numerical measurements. This difference is expressed by a cost function and its minimisation is performed using optimization algorithms, which automatically operate on the values of the constitutive

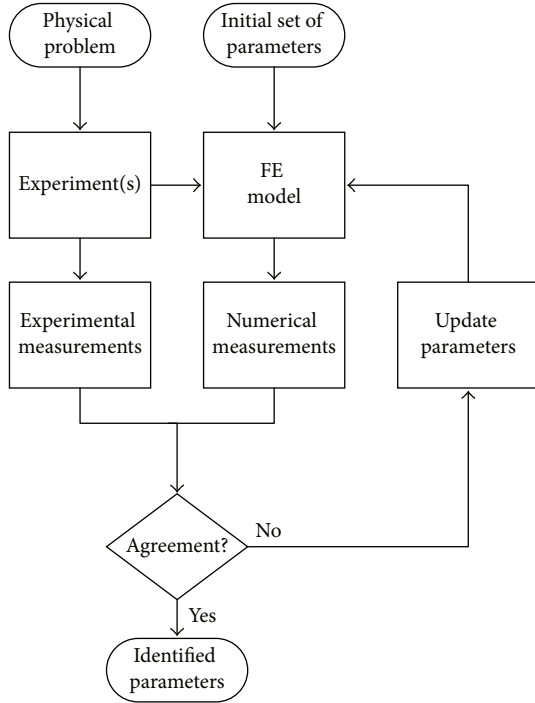


FIGURE 2: Schematic representation of inverse identification strategies. Adapted from [31].

parameters. Usually, cost functions compare the experimental and simulated loads and full-field measurements (e.g., [23, 59, 70–72]); less frequently, some authors propose to use only the load (e.g., [54, 66]), or full-field displacements (e.g., [24]) or strains (e.g., [21, 27–29]), at a given moment of loading.

A promising alternative to the use of FEMU is the Virtual Fields Method (VFM), which is based on the principle of virtual work. This approach does not require using time-consuming FE analysis and therefore avoids potential drawbacks related to the accuracy of FE models, namely, the representation of the geometry and boundary conditions [73]. The VFM was successfully used in the identification of parameters of constitutive laws describing the plastic behaviour of metal sheets [73–76]. However, the accuracy of the parameter identification using VFM depends on the adequate choice of the virtual field, which is currently a challenge for problems involving large heterogeneity of deformation of anisotropic materials, as well as large plastic deformations. In fact, in this type of problems, the optimal virtual field has to be evaluated for each time increment, which makes it less attractive than that for linear problems.

4.1. Overview of FEMU Strategies. This subsection provides an overview of the literature on inverse methodologies for the identification of parameters of constitutive laws based on inverse strategies coupled with FE simulations. These cases highlight that the identification procedure is dictated by the loading conditions, the geometry of the sample, the type of experimental results selected for the analysis, the cost functions, and the optimization algorithm used.

In this context, inverse strategies were developed for the identification of the anisotropy and hardening behaviour of metal sheets, simultaneously or separately. Table 1 shows a comparative outline of these strategies, whose key details are highlighted in the following subsections.

4.1.1. Identification of Isotropic Hardening and/or Yield Criterion Parameters

(1) Strategies Using Cruciform Specimens. There has been a steadily growing interest in developing inverse identification strategies supported by the use of the biaxial tensile test of cruciform specimens, coupled with full-field displacement or strain measurements (e.g., [21, 24–29]). In general, this test allows (i) strain paths ranging from uniaxial tension (in the arms region of the specimen) to balanced biaxial tension (in the centre section of the specimen), (ii) high strain gradients from the centre region of the specimen to the end of the arms region, and (iii) no contact between surfaces and therefore no friction. Also, by changing the load and/or displacement ratio over the two normal loading axes, it is possible to achieve several biaxial stress states in the central region of the specimen. However, this kind of test only permits attaining low values of equivalent plastic strain (close to those obtained in uniaxial tension) before instability occurs and no occurrence of out-of-plane shear stresses is observed (i.e., the test is insensitive to the material parameters associated with these stresses). Figure 3 shows a set of cruciform geometries proposed in the literature for identifying material parameters using FEMU strategies.

In this context, Cooreman et al. [21] proposed the use of the biaxial tensile test on a perforated cruciform specimen (see Figure 3(b)), to simultaneously identify the material parameters of Swift hardening law [34] and Hill’48 yield criterion that describe the plastic behaviour of a 0.8 mm thick DC06 sheet steel. The identification makes use of strain field data measured at the central region of the specimen (see dashed area in Figure 3(b)) taken at 7 distinct load steps and iteratively compared with their numerical counterparts using Gauss-Newton algorithm, using the following cost function:

$$\begin{aligned}
 F(\mathbf{A}) = \frac{1}{3n} \left\{ \sum_{i=1}^n \left[\left((\epsilon_{xx}^{\text{Exp}})_i - (\epsilon_{xx}^{\text{Num}}(\mathbf{A}))_i \right)^2 \right. \right. \\
 + \left. \left((\epsilon_{yy}^{\text{Exp}})_i - (\epsilon_{yy}^{\text{Num}}(\mathbf{A}))_i \right)^2 \right. \\
 \left. \left. + \left((\epsilon_{xy}^{\text{Exp}})_i - (\epsilon_{xy}^{\text{Num}}(\mathbf{A}))_i \right)^2 \right] \right\}^{1/2}, \quad (10)
 \end{aligned}$$

where $(\epsilon^{\text{Exp}})_i$ and $(\epsilon^{\text{Num}}(\mathbf{A}))_i$ are the experimentally determined and numerical values of the strain components ϵ_{xx} , ϵ_{yy} , and ϵ_{xy} at point i , respectively, and n is the total number of measuring points. According to the authors, the results from the inverse strategy are similar to those from classical strategies, except for the parameter ϵ_0 of the Swift law, which leads to clearly different yield stress values. The authors attribute the discrepancy of ϵ_0 results to the use of strain field results from loading steps that neglect the

TABLE I: Comparative overview of inverse identification strategies coupled with FE simulations.

Author	Type of test	Strain paths	Strain path reversal	Constitutive model	Optimization steps	Number of cost functions	Analysed results	Measuring instants
Cooreman et al. [21]	Cruciform biaxial tensile test	Uniaxial tension to biaxial stretching Simple shear to biaxial stretching (but depending on the test geometry)	No	Hill'48 criterion + Swift isotropic law Hill'48 criterion + Hockett-Sherby isotropic law (only 2 of 4 parameters identified)	One	One	Strain field (2D)	Various (7)
Schmaltz and Willner [24]	Cruciform biaxial tensile test		No		Two steps using the same cost function	One	Displacement field (2D)	One
Prates et al. [25]	Cruciform biaxial tensile test	Uniaxial tension to biaxial stretching	No	Hill'48 criterion + Swift isotropic law	Five steps using four cost functions	Four	Load + equivalent strain field (1D) Load + equivalent strain + strain path fields (1D)	During the test One
Prates et al. [26]	Cruciform biaxial tensile test	Uniaxial tension to biaxial stretching	No	Various criteria (4) + Swift and Voce isotropic laws	Two (Hill'48 criterion) or three (other criteria)	Two or three		During the test One
Zhang et al. [28]	Cruciform biaxial tensile test	Uniaxial tension to biaxial stretching	No	Bron and Besson criterion	One	One	Strain field (1D)	One
Liu et al. [29]	Cruciform biaxial tensile test	Uniaxial tension to biaxial stretching	No	Voce-type isotropic law	One	One	Strain field (2D)	During the test
Güner et al. [22]	Uniaxial tensile test on a notched sample	Near uniaxial tension	No	Yld2000 (2D) criterion	One	One	Strain field (2D) + load Load + displacement field (3D)	During the test Various (6)
Pottier et al. [23]	Out-of-plane test	Simple shear to biaxial stretching	No	Hill'48 Criterion + Ludwick isotropic law	One	One		
Chamekh et al. [51]	Circular and elliptical bulge tests	Biaxial stretching	No	Ludwick isotropic law + r_0 , r_{45} , and r_{90}	Two	One	Pressure	During the test
Bambach [52]	Circular bulge test	Biaxial stretching	No	Voce isotropic law	Two	Four	Pressure, pole strain, and pole thickness	During the test
Reis et al. [53]	Circular bulge test	Biaxial stretching	No	Swift isotropic law	Four	One	Pressure	During the test
Eggertsen and Mattiasson [54]	Three-point bending test	Tension-compression	Yes	Various kinematic laws (4)	One	One	Load	During the test

TABLE 1: Continued.

Author	Type of test	Strain paths	Strain path reversal	Constitutive model	Optimization steps	Number of cost functions	Analysed results	Measuring instants
Yin et al. [55]	Twin bridge shear test	Pure shear to uniaxial tension	Yes	Armstrong-Frederick kinematic law	One	One	Angular moment	During the test
				+ Voce isotropic law (only 2 of 3 parameters identified)				
Pereira et al. [56]	Shear test	Shear with reversal	Yes	Lemaître-Chaboche kinematic law	One	One	Load	During the test
				+ Swift isotropic law				

Note: 1D: in one direction in the sheet plane; 2D: on the surface of the sheet plane; 3D: three-dimensional.

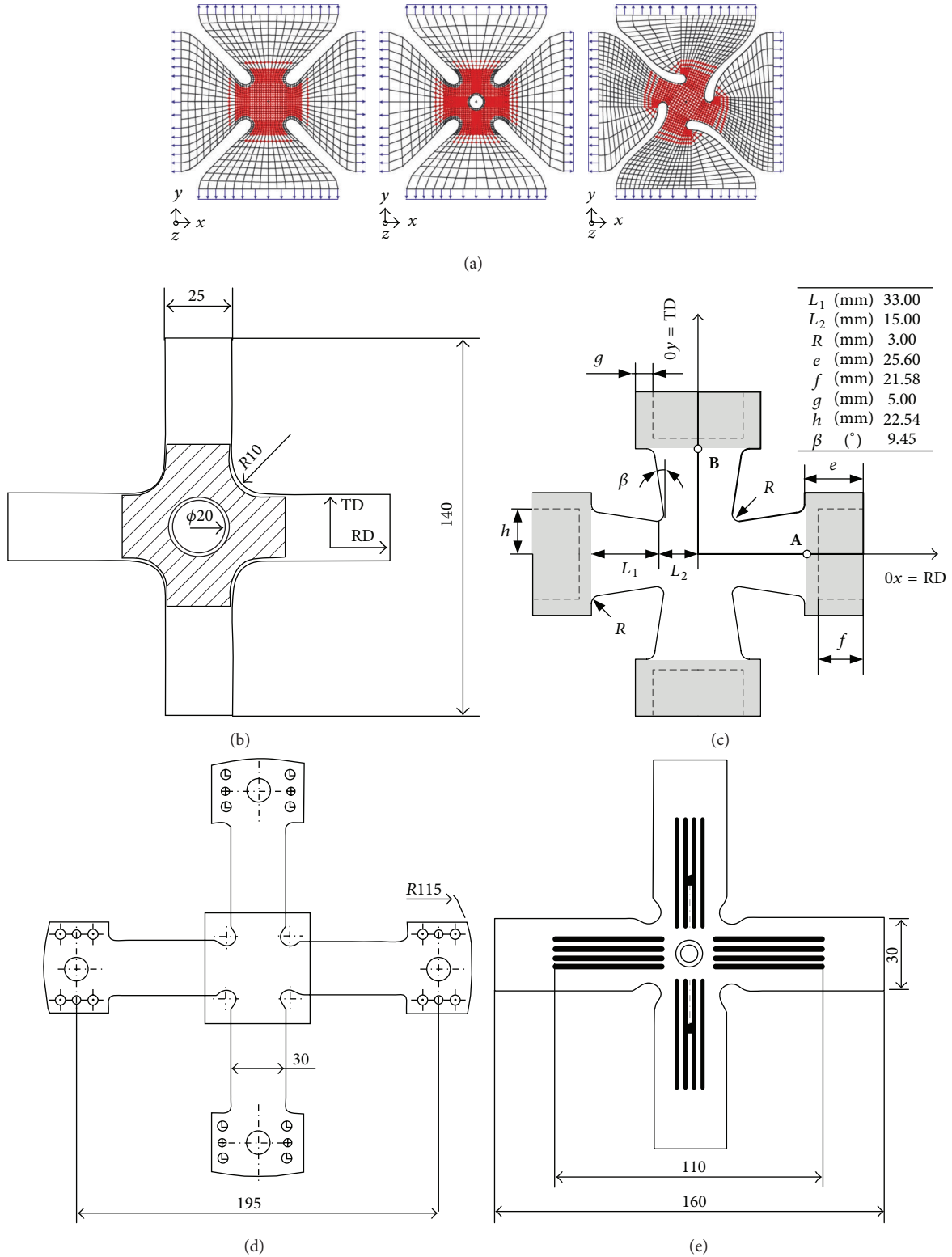


FIGURE 3: Cruciform specimen geometries proposed in the literature for FEMU strategies: (a) Schmalz and Willner [24]; (b) Cooreman et al. [21]; (c) Prates et al. [25, 26]; (d) Zhang et al. [27, 28]; and (e) Liu et al. [29].

beginning of the test. They suggest performing the inverse identification using additional strain fields from loading steps located near the onset of plastic deformation, which in our opinion can lead to high relative errors. A simpler alternative,

from the experimental point of view, would be to include in the identification a cost function considering the load-displacement curves for both axes of the cruciform sample, as adopted in other identification strategies later described.

Schmaltz and Willner [24] explored the usability of the biaxial tensile test on three cruciform specimen geometries, promoting different types of heterogeneous strain fields (see Figure 3(a)), in order to identify the plastic behaviour of a 2.0 mm thick DC04 sheet steel modelled via Hill'48 yield criterion and Hockett-Sherby hardening law [39]. The experimental and numerical displacement fields, in the regions in red (see Figure 3(a)) were compared and their difference was minimised using the Levenberg-Marquardt algorithm, with the following cost function:

$$F(\mathbf{A}) = \sum_{l=1}^2 \sum_{i=1}^n \left[(u_l^{\text{Exp}})_i - (u_l^{\text{Num}}(\mathbf{A}))_i \right]^2, \quad (11)$$

where $(u_l^{\text{Exp}})_i$ and $(u_l^{\text{Num}}(\mathbf{A}))_i$ are the experimentally determined and the numerically predicted values of the displacements at point i , respectively, in the 0x and 0y directions of the sheet plane ($l = 1, 2$), at a given moment of the test.

The optimization procedure starts with three different initial sets of parameters that lead to quite similar optimized values, for each test geometry, suggesting that the global optimum is reached. Moreover, the identification is split in two sequential steps (using the same cost function): (i) the first step identifies two of the Hockett-Sherby hardening law parameters (the yield stress and the saturation stress), under the assumption of isotropic (von Mises) material; the two remaining parameters of this law (contained in the exponent) are obtained by fitting the experimental results determined from the biaxial tensile test and are kept fixed during the identification procedure; (ii) in the second step, the Hill'48 parameters are identified. The cruciform geometry with the central hole (in the middle of Figure 3(a)) allows achieving the best results in terms of convergence of the iterative procedure and accuracy of the identified material parameters, which was assigned to the strong heterogeneity of the kinematic field.

Prates et al. [25, 26] designed a cruciform sample and developed two strategies for simultaneously identifying the parameters of the anisotropic yield criteria and isotropic hardening law of sheet metals. Both strategies use the results of the load evolution during the test and of the major and minor principal strains distributions, along the axes of the sample, at a given moment of the test, preceding the maximum load. Both strategies were numerically tested. The optimization of the design of the cruciform sample (see Figure 3(c)) was performed by means of a numerical study with the purpose of maximising the sensitivity of the test results to the values of the constitutive parameters and for allowing a wide range of strain paths, from uniaxial tension, at the arms of the sample, to near equibiaxial tension, at the centre of the sample.

The work was initially addressed for the identification of the parameters of the Hill'48 yield criterion and the isotropic Swift hardening law [25]. An inverse identification was performed without resorting to the traditional optimization algorithms (e.g., gradient-based algorithms, or others); that is, a specific algorithm was built for this purpose. The inverse analysis algorithm consists of a sequence of five optimization

steps, using the results of load evolution with the sample boundaries displacement during the test, for the axes 0x and 0y (see Figure 3(c)) and the distributions of von Mises equivalent strain along both axes of the sample, for an instant preceding and close to the maximum load. At each step, one or more parameters or a relationship between them is identified. The strategy was tested using numerically generated results of fictitious materials, which proved to be competitive, when compared with classical strategies. This allowed understanding that a sequential optimization, since properly elaborated, is clearly advantageous when compared to most commonly inverse identifications, consisting of using a unique cost function including different types of results.

The inverse analysis strategy mentioned above [25] enabled a good understanding of the issues involved, namely, concerning the delineation of the sequential algorithm leading to upper accuracy. This allowed extending the strategy to more complex constitutive models (yield criteria and isotropic hardening laws). Therefore, a general inverse identification strategy that sequentially uses three distinct cost functions was developed [26]. It resorts to the Levenberg-Marquardt algorithm for sequential optimization of the parameters of the yield criteria and isotropic hardening laws. More importantly, this strategy allows the identification of parameters of several yield criteria and hardening laws. It can be used directly for a given criterion or, sequentially, starting from the Hill'48 yield criterion and then using the Hill'48 criterion solution as an initial estimate for identifying the parameters of other criteria, on the condition that can be converted into the Hill'48 yield criterion for particular values of the parameters. In the last case, this strategy is detached in two stages and has the advantage of enabling the assessment of the adequacy of a number of constitutive models to describe the experimental results, starting from a simple anisotropic criterion, the Hill'48. The first stage consists of the simultaneous identification of the hardening law, Swift and/or Voce [38], in the case, and Hill'48 yield parameters, using the results of the load evolution in function of the displacement of the grips and the equivalent strain distribution at a given moment of the test, along the axes of the sample. The hardening parameters must be separately identified for the Swift and Voce laws and the one (Swift or Voce) that better describes the results of the cruciform test (if it is possible to distinguish) is selected for further optimization. The first stage involves the sequential minimisation of the following cost functions:

$$F_1(\mathbf{A}) = \frac{1}{Q_1} \sum_{i=1}^{Q_1} \left(\frac{P_i^{\text{Num}}(\mathbf{A}) - P_i^{\text{Exp}}}{P_i^{\text{Exp}}} \right)_{0x}^2 + \frac{1}{Q_2} \sum_{i=1}^{Q_2} \left(\frac{P_i^{\text{Num}}(\mathbf{A}) - P_i^{\text{Exp}}}{P_i^{\text{Exp}}} \right)_{0y}^2, \\ F_2(\mathbf{B}) = \frac{1}{R_1} \sum_{i=1}^{R_1} \left(\frac{\bar{\epsilon}_i^{\text{Num}}(\mathbf{B}) - \bar{\epsilon}_i^{\text{Exp}}}{\bar{\epsilon}_i^{\text{Exp}}} \right)_{0x}^2$$

$$+ \frac{1}{R_2} \sum_{i=1}^{R_2} \left(\frac{\bar{\epsilon}_i^{\text{Num}}(\mathbf{B}) - \bar{\epsilon}_i^{\text{Exp}}}{\bar{\epsilon}_i^{\text{Exp}}} \right)_{0y}^2, \quad (12)$$

where $P_i^{\text{Num}}(\mathbf{A})$ and P_i^{Exp} are the experimentally determined and numerical values of the load, respectively, and $\bar{\epsilon}_i^{\text{Num}}(\mathbf{B})$ and $\bar{\epsilon}_i^{\text{Exp}}$ are the experimentally determined and numerical values of the equivalent strain, respectively; Q_1 , Q_2 , R_1 , and R_2 are the total number of measuring points for axes $0x$ and $0y$ of the sample; \mathbf{A} and \mathbf{B} are vectors of isotropic hardening law and yield criteria parameters, respectively.

The second stage allows extending the parameters identification procedure to more complex yield functions, such as Barlat'91 [8], Karafillis and Boyce [9], and Drucker+L [3], the cases studied in the work. This second stage should be performed whenever the identification carried out during the first stage is found to be not enough satisfactory to capture the experimental strain paths results, along the axes of the sample, which are not considered in minimisation during the first stage. The second stage of this inverse strategy involves the minimisation of the following cost function:

$$F_3(\mathbf{C}) = \frac{1}{S_1} \sum_{i=1}^{S_1} (\rho_i^{\text{Num}}(\mathbf{C}) - \rho_i^{\text{Exp}})_{0x}^2 + \frac{1}{S_2} \sum_{i=1}^{S_2} (\rho_i^{\text{Num}}(\mathbf{C}) - \rho_i^{\text{Exp}})_{0y}^2, \quad (13)$$

where $\rho_i^{\text{Num}}(\mathbf{C})$ and ρ_i^{Exp} are the experimentally determined and numerical values of the strain path, respectively, S_1 and S_2 are the total number of measuring points for axes $0x$ and $0y$ of the sample, and \mathbf{C} is the vector of yield criteria parameters. This sequential optimization procedure is a successful alternative to the parameter identification by minimising a single cost function comprising all material parameters and results of different types, as commonly found in the literature. Namely, it is concluded that this last approach can deteriorate the description of the material behaviour, concerning the load versus displacement results, and therefore the parameters and the choice of the hardening law, without apparent improvement of the description of the results of equivalent strain and strain path distributions.

Zhang et al. [28] identified the parameters of Bron and Besson yield criterion [4] for both AA5086 aluminium alloy and DP980 dual-phase steel sheets, using a cruciform sample previously designed by the authors [27] and shown in Figure 3(d). The inverse identification strategy consists of minimising the gap between the experimental and numerical distributions of the major and minor strains along the diagonal direction of the sample central area, at an instant immediately before rupture, using a SIMPLEX optimization algorithm. The cost function used is defined as follows:

$$F(\mathbf{A}) = \sum_{l=1}^2 \frac{\sum_{i=1}^n ((\epsilon_l^{\text{Exp}})_i - (\epsilon_l^{\text{Num}}(\mathbf{A}))_i)^2}{\sum_{i=1}^n ((\epsilon_l^{\text{Exp}})_i)^2}, \quad (14)$$

where $(\epsilon_l^{\text{Exp}})_i$ and $(\epsilon_l^{\text{Num}}(\mathbf{A}))_i$ are the experimentally determined and numerical values of the principal strain components ($l = 1, 2$) at point i , respectively, n is the total number of measuring points along the diagonal path, and \mathbf{A} is the vector of 13 parameters to be identified: four isotropy and eight anisotropy parameters of the Bron and Besson yield model and the yield stress value. The hardening of the material is modelled with isotropic hardening described by the Voce law, in case of AA5086 aluminium, and an equation based on Swift and Voce laws, for DP980 steel. In both cases, the hardening parameters are directly identified from results of the tensile test in the rolling direction and were kept fixed during the inverse identification procedure (except the yield stress).

Liu et al. [29] designed a cruciform sample with a thickness-reduced central zone and four slots at each arm (see Figure 3(e)), to perform the parameters identification of a modified Voce law, describing the hardening behaviour of AA5086 aluminium sheet. The inverse analysis procedure makes use of the SIMPLEX algorithm, to minimise the difference between experimental and numerical strains measured at the centre region of the sample during the test, expressed by the following cost function:

$$F(\mathbf{A}) = \sum_{l=1}^2 \left[\frac{\sum_{i=1}^n ((\epsilon_l^{\text{Exp}})_i - (\epsilon_l^{\text{Num}}(\mathbf{A}))_i)^2}{\sum_{i=1}^n ((\epsilon_l^{\text{Exp}})_i)^2} \right]^{1/2}, \quad (15)$$

where $(\epsilon_l^{\text{Exp}})_i$ and $(\epsilon_l^{\text{Num}}(\mathbf{A}))_i$ are the experimentally determined and numerical values of the principal strain components ($l = 1, 2$) at point i , respectively, at the central point of the sample, n is the total number of the time points of simulation, and \mathbf{A} is the vector of three hardening parameters of the modified Voce law. The experimental force evolution along the two arms of the cruciform specimen was applied to the FE model for the numerical simulations, taking into account the lack of synchronization observed in the two tensile forces on each axis of the sample. In this inverse identification of the modified Voce law parameters, three yield functions were considered: von Mises, Hill'48, and the more advanced Bron and Besson criterion, whose parameters were previously identified [27]. The identified biaxial flow stress curves were then compared with an experimental curve obtained from a uniaxial tensile test, showing that a good agreement can be achieved if an adequate yield function is used in the FE model.

(2) *Strategies Using Bulge Test.* Most of the strain paths observed in deep-drawing components are in the range between simple tension and balanced biaxial tension, which justifies the widespread use of the cruciform specimen in the framework of the methodologies of inverse analysis. Nevertheless, this test has a strong drawback related to low deformation levels achieved, particularly in the central region of the sample, in which the strain and stress paths can be close to equibiaxial, although being dependent on the applied load or displacement ratios along the two axes of the specimen. In contrast, the bulge test allows obtaining relatively high strain values before necking, and so the flow stress curves can be assessed up to large strain values, for several biaxial strain (or

stress) paths depending on the geometry of the die (circular or elliptical). In this context, a few cases of inverse analysis methodologies were developed, with the aim of identifying the parameters of work-hardening laws.

Chamekh et al. [51] describe an inverse approach, based on Artificial Neural Networks (ANN), to identify the material parameters of a stainless steel (AISI 304). They use the results of the evolutions of pressure with the pole height, which are transferred to the neural network. The ANN is trained by means of curves of pressure versus displacement of the central point of the cap, generated by finite element simulations of the circular bulge test. During the training process, the network computes the weight connections, minimising the total mean squared error between the actual output and the desired output. The neural network generates an approximated function for the material parameters depending on the profile of the evolution of pressure with the pole height curve. Then, it was exploited for the identification of material parameters from experimental results. The Ludwick hardening law [33] and the Hill'48 yield criterion were selected. Therefore, the set of parameters to be identified also comprise the Lankford coefficients, r_0 , r_{45} , and r_{90} . The material parameters are identified according to the following two steps: (i) the first step, using the circular bulge test, is to find the Ludwick hardening law parameters (assuming the knowledge of Lankford's coefficients determined from the tensile tests); (ii) the second step, using the elliptical bulge test for an off axis angle of 0° , is to recalculate the Lankford's coefficients. An elliptical die for an off axis angle of 45° is used for the validation of the parameters identification. The authors conclude the following: (i) the ANN methodology can predict acceptable combination of the values of the material parameters; (ii) once the ANN was trained, output results for a given set of input data are available almost instantaneously. Despite these conclusions, it should be noted that the values of the experimental (from the tensile test) and identified hardening coefficients are far away (the experimental and identified values are 0.67 and 0.4, resp.). The remaining identified values of the parameters differ between 20 and 30% when compared with the tensile test except for the yield stress, whose values are approximately equal.

Bambach [52] explored the usability of the circular bulge test to identify the parameters of the Voce law of a fictitious material, which is considered isotropic. Initially, the membrane theory is applied to the results as in experimental cases, in order to obtain a set of parameters of the Voce, by fitting the stress versus strain results. The inverse analysis strategy proposed resorts to a gradient-based optimization algorithm, which is known for being sensitive to the initial solution. Thus, by using an initial solution, the one previously obtained with the membrane theory, it is expected to avoid convergence problems. The work gives special focus on the choice of the cost function to be minimised, making use, separately or simultaneously, of results of pressure versus pole height, pole strain versus pole height, and pole thickness versus pole height, and formulated as follows:

$$F_p(\mathbf{A}) = \int_0^{h_{\max}} [p^{\text{Exp}}(h) - p^{\text{Num}}(h, \mathbf{A})]^2 dh,$$

$$F_\varepsilon(\mathbf{A}) = \int_0^{h_{\max}} [\varepsilon^{\text{Exp}}(h) - \varepsilon^{\text{Num}}(h, \mathbf{A})]^2 dh,$$

$$F_t(\mathbf{A}) = \int_0^{h_{\max}} [t^{\text{Exp}}(h) - t^{\text{Num}}(h, \mathbf{A})]^2 dh,$$

(16)

where $F_p(\mathbf{A})$, $F_\varepsilon(\mathbf{A})$, and $F_t(\mathbf{A})$ are cost functions defined by the pressure, p , strain, ε , and thickness, t , with pole height, h , respectively. The author concluded that the reidentification procedure (so called by the author) is significantly improved when combining the first two types of results. This significantly improves the reidentification, since it will contribute to reducing the search area where the minimum value of the objective function is located. It should be noted that this proposal is a reidentification, which has its starting point in the parameters previously obtained from the use of the membrane theory, such as in the traditional procedure recommended by the ISO standard [77]. Furthermore, it needs to resort to strain results in the pole of the cap during the test, which does not simplify the experimental procedure.

Reis et al. [53] proposed an inverse methodology for determining the hardening law of metal sheets, from the results of pressure versus pole height obtained in the bulge test, involving the identification of the parameters of the Swift law. The starting point of this analysis was to realize that it is possible to achieve a unified description (i.e., overlapping) of the evolution of the pressure with the pole height, for a given value of the hardening parameter of the Swift law, regardless of the yield stress and anisotropy of the material and sheet thickness. To achieve the overlapping of such curves, appropriate multiplying factors must be used for the values of pressure and pole height, depending on the yield stresses and thicknesses ratios of the sheets and also on their anisotropy. Thereafter, an inverse analysis methodology was developed, which consists in the search for the best coincidence between pressure versus pole height experimental and reference curves, with the latter being obtained by numerical simulation assuming isotropic material behaviour with various values of the hardening parameter in the range of the material under study. This methodology, when compared with the classical strategy, proves to be an efficient alternative avoiding the use of complex devices for measuring the radius of curvature and strain at the pole of the cap, during the bulge test. Moreover, the authors claim that it is easy to implement and it is more efficient than classical approach, since (i) a unique set of numerical curves can be used within a relatively wide range of hardening coefficients, that is, covering the values usually found within one or several class of materials, without having to remake the simulations every time an identification is performed; (ii) it is not exposed to experimental errors related to the evaluation of the strain at the pole of the bulge and the use of membrane theory approach for assessment of the stress from the radius of curvature, which is usually the major source of errors.

(3) *Other Specimens.* Güner et al. [22] proposed an inverse analysis procedure for the identification of the Yld2000-2D

yield criterion parameters [7]. This study uses a notched specimen submitted to a tensile test, in order to obtain an inhomogeneous deformation field. Moreover, a layer compression test is used in order to supply additional information, that is, the equibiaxial yield stress. The required data for the inverse identification are the major and minor principal strains in the sheet plane and the load and the equibiaxial yield stress. The cost function is minimised using the Levenberg-Marquardt algorithm and is written as follows:

$$\begin{aligned}
 F(\mathbf{A}) &= \sum_{i=1}^{n_{inc}} \sum_{j=1}^{n_{elem}} \left[(\varepsilon_{1,ij}^{Num}(\mathbf{A}) - \varepsilon_{1,ij}^{Exp})^2 + (\varepsilon_{2,ij}^{Num}(\mathbf{A}) - \varepsilon_{2,ij}^{Exp})^2 \right] \\
 &+ C_1 \sum_{i=1}^{n_{inc}} \left[(P_i^{Num}(\mathbf{A}) - P_i^{Exp})^2 \right] \\
 &+ C_2 (\sigma_b(\mathbf{A}) - \sigma_b^{Exp})^2,
 \end{aligned} \tag{17}$$

where ε_1 and ε_2 are the principal strains measured at each tool displacement increment i , at each element of the optical measurements, j ; P represents the load and σ_b the equibiaxial yield stress; C_1 and C_2 are scale factors. The value of $\sigma_b(\mathbf{A})$ is analytically calculated at each iteration with the values of \mathbf{A} predicted by the optimization algorithm. Different alternative orientations of the specimen with the rolling direction (0° , 45° , and 90°) and configurations of the cost function (setting one of the three terms of the cost function equal to zero) were considered to test the inverse procedure. The authors highlight the importance of including strain information and the equibiaxial stress on the cost function, in order to improve the characterization of the anisotropy coefficients.

Pottier et al. [23] developed an out-of-plane testing procedure for the simultaneous identification of Hill'48 yield criterion and Ludwick hardening law parameters of a rolled titanium sheet. Figure 4 illustrates the experimental setup and the geometry of the sample developed by the authors. A hemispherical punch applies a prescribed displacement normal to the sheet plane, at the centre of the surface of the sample, using a simple uniaxial tensile test machine. Two cameras are located on the opposite side of the sample and the components of the displacement fields along the $0x$, $0y$, and $0z$ axes are captured during the test using stereo digital image correlation. The sample was designed in order to exhibit multiaxial stress states, including shear, tension, and biaxial stretching. The numerical displacements fields along the $0x$, $0y$, and $0z$ axes and the global load are obtained from a numerical model of the test and compared to the experimental ones using a single cost function, formulated as follows:

$$F(\mathbf{A}) = \left[\sum_{i,j=1}^{N_t, n} \left(\frac{u_{x,ij}^{Num}(\mathbf{A}) - u_{x,ij}^{Exp}}{\max_{i,j}(u_x^{Exp})} \right)^2 \right]^{1/2},$$

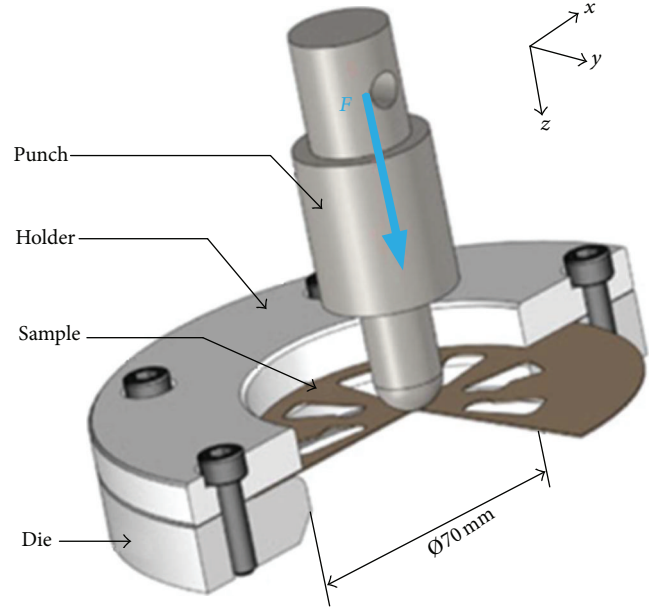


FIGURE 4: Schematic representation of the out-of-plane test developed by Pottier et al. [23].

$$\begin{aligned}
 &+ \sum_{i,j=1}^{N_t, n} \left(\frac{u_{y,ij}^{Num}(\mathbf{A}) - u_{y,ij}^{Exp}}{\max_{i,j}(u_y^{Exp})} \right)^2 \\
 &+ \sum_{i,j=1}^{N_t, n} \left(\frac{u_{z,ij}^{Num}(\mathbf{A}) - u_{z,ij}^{Exp}}{\max_{i,j}(u_z^{Exp})} \right)^2 \\
 &+ n \left(\frac{P_i^{Num}(\mathbf{A}) - P_i^{Exp}}{\max_i(P^{Exp})} \right)^2 \Big]^{1/2},
 \end{aligned} \tag{18}$$

where N_t is the number of time steps considered and n is the number of measured points; u_x , u_y , and u_z are the displacements along the $0x$, $0y$, and $0z$ axes, respectively, P is the global load and \mathbf{A} is the vector of parameters to identify; the subscripts Num and Exp refer to numerical and experimental results and i and j refer to the number of time steps and measured points, respectively. The minimisation of the cost function is performed with the Levenberg-Marquardt algorithm. To assess the quality of the identified set of constitutive parameters, the authors performed deep-drawing tests of a circular cup. Moreover, additional identifications of the constitutive parameters of the material were performed, following two different strategies: a classic strategy, based on three tensile tests cut along three different directions in the sheet plane, and an inverse identification strategy using heterogeneous planar shear-like tests, previously proposed [59]. The experimental results of the earing profile of the circular cup were then compared with the numerically predicted results from the different parameter identification strategies. The authors concluded that the use of the nonplanar sample allows a more accurate

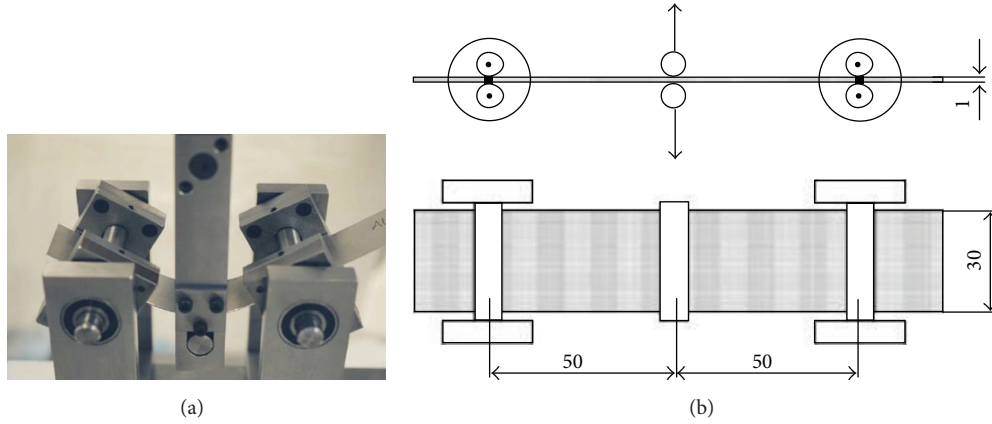


FIGURE 5: Device for three-point bending test [54]: (a) experimental setup and (b) schematic representation of horizontal and vertical views.

prediction of the earing profile than the planar shear-like tests and the three tensile tests, since the nonplanar sample test covers a wider range of strain paths. However, in our opinion, the chosen mechanical test shows a relative degree of complexity and has the inconvenience of presenting contact with friction between the punch and the metal sheet, which always raises questions concerning the impact of contact with friction on the identification of the constitutive parameters.

4.1.2. Identification of Kinematic Hardening. The identification of the kinematic hardening plays a significant role when phenomena such as the Bauschinger effect and permanent softening, due to reverse of strain path and other strain path changes, are relevant for the subsequent plastic deformation behaviour. Depending on the material and the strain path changes occurring in the deep-drawing process, these phenomena can be more or less noticeable and relevant. The Bauschinger effect is also associated with the springback, due to premature yielding after reversal of strain path [14]. Springback is the strain recovery when forming loads are removed, and its magnitude, which depends on the flow stress value [11] and Young's modulus, can also be influenced by the Bauschinger effect [78]. Therefore, the proper modelling and identification of the kinematic hardening are also important in order to efficiently predict the springback.

In this sense, Eggertsen and Mattiasson [54] were focused on the identification of the kinematic hardening law with the main concern of the accurate prediction of springback. The goal was to select the model able to accurately describe kinematic hardening features, such as the early reyielding, transient behaviour, work-hardening stagnation, and permanent softening, taking also into account the complexity on the evaluation of its parameters. Three-point bending tests (see Figure 5) on four typical materials from car manufacturing industry were performed: two dual-phase steels (TKS-DP600HF and SSAB-DP600), from different suppliers and with different thicknesses, a mild steel (Voesst-DX56D), and an interstitial-free steel (TKS-220IF). Five different hardening models were considered: (i) a pure isotropic hardening law, used as comparative reference; (ii) a mixed isotropic-kinematic law [79, 80]; (iii) the Armstrong-Frederick model

[44]; (iv) the Geng-Wagoner hardening law [47]; and (v) the Yoshida-Uemori hardening law [14]. The hardening parameters of all models were determined by inverse analysis, where the difference between the experimentally and numerically generated load-displacement curves of the three-point bending test is minimised. The inverse identification of the material parameters was performed resorting to Response Surface Methodology, using the following cost function:

$$F(\mathbf{A}) = \frac{1}{n} \sum_{i=1}^n w_i \left(\frac{P_i^{\text{Num}}(\mathbf{A}) - P_i^{\text{Exp}}}{s_i} \right)^2, \quad (19)$$

where $P_i^{\text{Num}}(\mathbf{A})$ and P_i^{Exp} represent the calculated and measured values of the punch load as a function of the vector of hardening parameters \mathbf{A} , respectively; s_i is the residual scale factor; and w_i is the weight applied to each component of the cost function. Both s_i and w_i were set equal to 1. The authors conclude that Yoshida-Uemori model provides the best result for all materials, while the isotropic hardening model gives the worst result. However, taking into account the accuracy and the complexity of the hardening model, the authors point out that Geng-Wagoner law corresponds to a better compromise. In fact, they state that about 30 simulations are needed to optimize the parameters of the mixed isotropic-kinematic hardening law, while up to 170 simulations are required to optimize the parameters of Yoshida-Uemori hardening law.

Pereira et al. [56] outline an inverse analysis methodology for simultaneously identifying the parameters of the isotropic Swift law and the Lemaitre-Chaboche kinematic law [13] of metal sheets, using a reverse shear test. The outlined strategy uses a modified shear sample with a cylindrical notch along the axis of the sample, in order to confine the plastic deformation within the entire gauge section, which is not the case for the classical shear samples with constant thickness (see Figure 6). The geometry of the cylindrical notch was defined in order to ensure that all strain values, between the maximum (in the centre of the notch) and the minimum (zero, along the edge of the notch), are as much as possible represented at the moment of the strain path reversing. The geometry of the sample allows that the

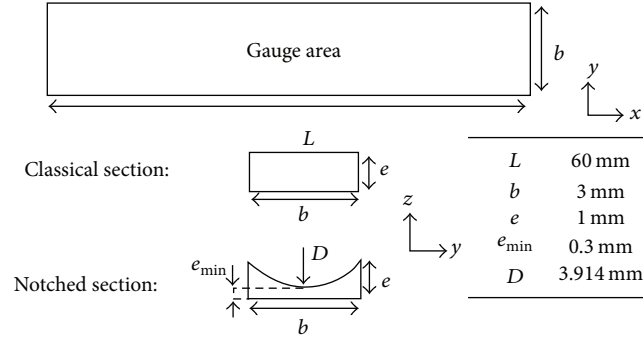


FIGURE 6: Geometry and dimensions of the classical and proposed notched shear specimens used in [56].

boundary conditions of experimental tests are accurately reproduced numerically and avoids the errors in the experimental determination of the stress versus strain curves, used in traditional methodologies, whose accuracy requires homogeneity of the stress and strain fields in the sample. The inverse analysis methodology consists of minimising the gap between experimental and numerical load versus displacement curves by making variations of the constitutive parameters, using the Levenberg-Marquardt algorithm. The following cost function is used:

$$F(\mathbf{A}) = \frac{1}{q} \sum_{i=1}^q \left(\frac{P_i^{\text{Exp}} - P_i^{\text{Num}}(\mathbf{A})}{P_i^{\text{Exp}}} \right)^2 + \frac{1}{p} \sum_{i=1}^p \left(\frac{P_i^{\text{Exp}} - P_i^{\text{Num}}(\mathbf{A})}{P_i^{\text{Exp}}} \right)^2, \quad (20)$$

where P_i^{Exp} and $P_i^{\text{Num}}(\mathbf{A})$ are, respectively, the experimental and numerical values of load for the same tool displacement; q and p are the total number of points in the forward and reverse paths, respectively; and \mathbf{A} is the vector of the parameters to be identified. The parameters of the Hill'48 yield criterion that best describe the anisotropy of the fictitious materials used in this work (described by Drucker+L yield criterion) were identified following the methodology mentioned above, proposed by Prates et al. [25]. This methodology also allows identifying the parameters of the isotropic Swift law, which were used as first estimate in this inverse analysis. If no identification of the Swift law parameters was previously performed, the first estimate of isotropic Swift hardening parameters can be obtained adopting typical values for the material under study. It is appropriate to experimentally test this methodology.

Yin et al. [55] proposed the use of the twin bridge cyclic shear test proposed by Brosius et al. [81] to evaluate the Bauschinger effect on three classes of steel sheets, DC06, DP600, and TRIP700. The twin bridge shear specimen has two gauge areas that are simultaneously deformed when a moment is applied. Due to the moment application, instead of load, no unwanted reaction moment is created, in contrast with the ASTM shear specimen. The inverse identification strategy involves minimising the difference between experimental and numerical angular moment results, resorting

to a Trust Region Reflective Method [82], to identify the parameters of isotropic Voce hardening law and Armstrong-Frederick kinematic hardening law. The cost function is described as follows:

$$F(\mathbf{A}) = \sum_{i=1}^q \left(M_i^{\text{Exp}} - M_i^{\text{Num}}(\mathbf{A}) \right)^2 + \sum_{i=1}^p \left(M_i^{\text{Exp}} - M_i^{\text{Num}}(\mathbf{A}) \right)^2, \quad (21)$$

where M_i^{Exp} and $M_i^{\text{Num}}(\mathbf{A})$ are, respectively, the experimental and numerical values of moment at the same rotation angles; q and p are the total number of points in the forward and backward paths, respectively; and \mathbf{A} is the vector of kinematic hardening parameters of the Lemaitre-Chaboche law and two of the three parameters of the Voce law. The remaining Voce law parameter, the yield stress, is obtained from uniaxial tensile tests in the rolling direction and is kept fixed during the identification procedure.

5. Final Remarks

This review shows that a great investment has been made lately in the development of inverse strategies, namely, in FEMU strategies for the identification of parameters of constitutive laws describing the plastic behaviour of metal sheets. This includes the sample design, loading conditions, and optimization procedure and intends to make the identification of the material parameters easier and more reliable. Currently, some of these strategies allows determining simultaneously the parameters of isotropic hardening law and/or anisotropic yield criteria, using only a single test. Others only allow the evaluation of the parameters of kinematic hardening law. Also, most strategies are limited to specific types of work-hardening laws and plasticity criteria. In this context, the investment in such strategies should be directed towards the simultaneous identification of parameters of any constitutive law, including isotropic and kinematic hardening, and any anisotropic yield criterion. This must be accomplished using the results of the minimum number of mechanical tests and results, for example, from the biaxial test of the cruciform sample and the shear test, and building their own optimization procedure, eventually sequential. In fact, given

that the optimization procedure for parameters identification can influence the solution, it is important to examine the possibility of resorting to sequential optimization procedures, especially when using different types of results.

Competing Interests

The authors declare that there is no conflict of interests regarding the publication of this paper.

Acknowledgments

The authors gratefully acknowledge the financial support of the Portuguese Foundation for Science and Technology (FCT), Portugal, via Projects PTDC/EMS-TEC/0702/2014 (POCI-01-0145-FEDER-016779), PTDC/EMS-TEC/6400/2014 (POCI-01-0145-FEDER-016876), and UID/EMS/00285/2013, by UE/FEDER through Program COMPETE2020. P. A. Prates, A. F. G. Pereira, and N. A. Sakharova were supported by a grant for scientific research from the Portuguese Foundation for Science and Technology (refs. SFRH/BPD/101465/2014, SFRH/BD/102519/2014, and SFRH/BPD/107888/2015, resp.). All supports are gratefully acknowledged.

References

- [1] W. Hu, "An orthotropic yield criterion in a 3-D general stress state," *International Journal of Plasticity*, vol. 21, no. 9, pp. 1771–1796, 2005.
- [2] S. Soare, *On the use of homogeneous polynomials to develop anisotropic yield functions with applications to sheet metal forming [Ph.D. thesis]*, University of Florida, 2007.
- [3] O. Cazacu and F. Barlat, "Generalization of Drucker's yield criterion to orthotropy," *Mathematics and Mechanics of Solids*, vol. 6, no. 6, pp. 613–630, 2001.
- [4] F. Bron and J. Besson, "A yield function for anisotropic materials—application to aluminum alloys," *International Journal of Plasticity*, vol. 20, no. 4-5, pp. 937–963, 2004.
- [5] F. Barlat, H. Aretz, J. W. Yoon, M. E. Karabin, J. C. Brem, and R. E. Dick, "Linear transformation-based anisotropic yield functions," *International Journal of Plasticity*, vol. 21, no. 5, pp. 1009–1039, 2005.
- [6] B. Plunkett, O. Cazacu, and F. Barlat, "Orthotropic yield criteria for description of the anisotropy in tension and compression of sheet metals," *International Journal of Plasticity*, vol. 24, no. 5, pp. 847–866, 2008.
- [7] F. Yoshida, H. Hamasaki, and T. Uemori, "A user-friendly 3D yield function to describe anisotropy of steel sheets," *International Journal of Plasticity*, vol. 45, pp. 119–139, 2013.
- [8] F. Barlat, D. J. Lege, and J. C. Brem, "A six-component yield function for anisotropic materials," *International Journal of Plasticity*, vol. 7, no. 7, pp. 693–712, 1991.
- [9] A. P. Karafillis and M. C. Boyce, "A general anisotropic yield criterion using bounds and a transformation weighting tensor," *Journal of the Mechanics and Physics of Solids*, vol. 41, no. 12, pp. 1859–1886, 1993.
- [10] O. Cazacu, B. Plunkett, and F. Barlat, "Orthotropic yield criterion for hexagonal closed packed metals," *International Journal of Plasticity*, vol. 22, no. 7, pp. 1171–1194, 2006.
- [11] F. Barlat, J. J. Gracio, M.-G. Lee, E. F. Rauch, and G. Vincze, "An alternative to kinematic hardening in classical plasticity," *International Journal of Plasticity*, vol. 27, no. 9, pp. 1309–1327, 2011.
- [12] H. Vegter and A. H. Van Den Boogaard, "A plane stress yield function for anisotropic sheet material by interpolation of biaxial stress states," *International Journal of Plasticity*, vol. 22, no. 3, pp. 557–580, 2006.
- [13] J. L. Chaboche, "A review of some plasticity and viscoplasticity constitutive theories," *International Journal of Plasticity*, vol. 24, no. 10, pp. 1642–1693, 2008.
- [14] F. Yoshida and T. Uemori, "A model of large-strain cyclic plasticity and its application to springback simulation," *International Journal of Mechanical Sciences*, vol. 45, no. 10, pp. 1687–1702, 2003.
- [15] B. M. Chaparro, S. Thuillier, L. F. Menezes, P. Y. Manach, and J. V. Fernandes, "Material parameters identification: gradient-based, genetic and hybrid optimization algorithms," *Computational Materials Science*, vol. 44, no. 2, pp. 339–346, 2008.
- [16] M. Rabahallah, T. Balan, S. Bouvier et al., "Parameter identification of advanced plastic strain rate potentials and impact on plastic anisotropy prediction," *International Journal of Plasticity*, vol. 25, no. 3, pp. 491–512, 2009.
- [17] T. Kuwabara, "Advances in experiments on metal sheets and tubes in support of constitutive modeling and forming simulations," *International Journal of Plasticity*, vol. 23, no. 3, pp. 385–419, 2007.
- [18] N. Deng, T. Kuwabara, and Y. P. Korkolis, "Cruciform specimen design and verification for constitutive identification of anisotropic sheets," *Experimental Mechanics*, vol. 55, no. 6, pp. 1005–1022, 2015.
- [19] I. Zidane, D. Guines, L. Léotoing, and E. Ragneau, "Development of an in-plane biaxial test for forming limit curve (FLC) characterization of metallic sheets," *Measurement Science and Technology*, vol. 21, no. 5, Article ID 055701, pp. 1–11, 2010.
- [20] S. Avril, M. Bonnet, A.-S. Bretelle et al., "Overview of identification methods of mechanical parameters based on full-field measurements," *Experimental Mechanics*, vol. 48, no. 4, pp. 381–402, 2008.
- [21] S. Cooreman, D. Lecompte, H. Sol, J. Vantomme, and D. Debruyne, "Identification of mechanical material behavior through inverse modeling and DIC," *Experimental Mechanics*, vol. 48, no. 4, pp. 421–433, 2008.
- [22] A. Güner, C. Soyarslan, A. Brosius, and A. E. Tekkaya, "Characterization of anisotropy of sheet metals employing inhomogeneous strain fields for Yld2000-2D yield function," *International Journal of Solids and Structures*, vol. 49, no. 25, pp. 3517–3527, 2012.
- [23] T. Pottier, P. Vacher, F. Toussaint, H. Louche, and T. Coudert, "Out-of-plane testing procedure for inverse identification purpose: application in sheet metal plasticity," *Experimental Mechanics*, vol. 52, no. 7, pp. 951–963, 2012.
- [24] S. Schmaltz and K. Willner, "Comparison of different biaxial tests for the inverse identification of sheet steel material parameters," *Strain*, vol. 50, no. 5, pp. 389–403, 2014.
- [25] P. A. Prates, M. C. Oliveira, and J. V. Fernandes, "A new strategy for the simultaneous identification of constitutive laws parameters of metal sheets using a single test," *Computational Materials Science*, vol. 85, pp. 102–120, 2014.
- [26] P. A. Prates, M. C. Oliveira, and J. V. Fernandes, "Identification of material parameters for thin sheets from single biaxial

- tensile test using a sequential inverse identification strategy,” *International Journal of Material Forming*, vol. 9, no. 4, pp. 547–571, 2016.
- [27] S. Zhang, L. Leotoing, D. Guines, S. Thuillier, and S.-L. Zang, “Calibration of anisotropic yield criterion with conventional tests or biaxial test,” *International Journal of Mechanical Sciences*, vol. 85, pp. 142–151, 2014.
- [28] S. Zhang, L. Léotoing, D. Guines, and S. Thuillier, “Potential of the cross biaxial test for anisotropy characterization based on heterogeneous strain field,” *Experimental Mechanics*, vol. 55, no. 5, pp. 817–835, 2015.
- [29] W. Liu, D. Guines, L. Leotoing, and E. Ragneau, “Identification of sheet metal hardening for large strains with an in-plane biaxial tensile test and a dedicated cross specimen,” *International Journal of Mechanical Sciences*, vol. 101–102, pp. 387–398, 2015.
- [30] F. Dunne and N. Petrinic, *Introduction to Computational Plasticity*, Oxford University Press, 2005.
- [31] P. Jemny, A.-S. Caro-Bretelle, and E. Pagnacco, “Identification from measurements of mechanical fields by finite element model updating strategies. A review,” *European Journal of Computational Mechanics*, vol. 18, no. 3–4, pp. 353–376, 2009.
- [32] J. H. Hollomon, “Tensile deformations,” *Transactions of the Metallurgical Society of AIME*, vol. 162, pp. 268–290, 1945.
- [33] P. Ludwick, *Elemente der Technologischen Mechanik*, Springer, Berlin, Germany, 1909.
- [34] H. W. Swift, “Plastic instability under plane stress,” *Journal of the Mechanics and Physics of Solids*, vol. 1, no. 1, pp. 1–18, 1952.
- [35] D. C. Ludwison, “Modified stress–strain relation for FCC metals and alloys,” *Metallurgical Transactions*, vol. 2, no. 10, pp. 2825–2828, 1971.
- [36] A. K. Ghosh, “Tensile instability and necking in materials with strain hardening and strain-rate hardening,” *Acta Metallurgica*, vol. 25, no. 12, pp. 1413–1424, 1977.
- [37] J. V. Fernandes, D. M. Rodrigues, L. F. Menezes, and M. F. Vieira, “A modified Swift law for prestrained materials,” *International Journal of Plasticity*, vol. 14, no. 6, pp. 537–550, 1998.
- [38] E. Voce, “The relationship between stress and strain for homogeneous deformation,” *Journal of the Institute of Metals*, vol. 74, pp. 537–562, 1948.
- [39] J. E. Hockett and O. D. Sherby, “Large strain deformation of polycrystalline metals at low homologous temperatures,” *Journal of the Mechanics and Physics of Solids*, vol. 23, no. 2, pp. 87–98, 1975.
- [40] D. Banabic, *Sheet Metal Forming Processes—Constitutive Modelling and Numerical Simulation*, Springer, 2010.
- [41] P. Larour, *Strain rate sensitivity of automotive sheet steels: influence of plastic strain, strain rate, temperature, microstructure, bake hardening and pre-strain [Ph.D. thesis]*, RWTH Aachen University, 2010.
- [42] W. Prager, “Recent developments in the mathematical theory of plasticity,” *Journal of Applied Physics*, vol. 20, pp. 235–241, 1949.
- [43] H. Ziegler, “A modification of Prager’s hardening rule,” *Quarterly of Applied Mathematics*, vol. 17, pp. 55–65, 1959.
- [44] P. J. Armstrong and C. O. Frederick, “A mathematical representation of the multiaxial Bauschinger effect,” GEGB Report RD/B/N 731, 1966.
- [45] C. Teodosiu and Z. Hu, “Evolution of the intragranular microstructure at moderate and large strains: modelling and computational significance,” in *Proceedings of the 5th International Conference on Numerical Methods in Industrial Forming Processes (NUMIFORM ’95)*, pp. 173–182, Ithaca, NY, USA, 1995.
- [46] C. Teodosiu and Z. Hu, “Microstructure in the continuum modelling of plastic anisotropy,” in *Proceedings of the 19th Riso International Symposium on Materials Science: Modelling of Structure and Mechanics of Materials from Microscale to Products*, pp. 149–168, Riso National Laboratory, 1998.
- [47] L. Geng, Y. Shen, and R. H. Wagoner, “Anisotropic hardening equations derived from reverse-bend testing,” *International Journal of Plasticity*, vol. 18, no. 5–6, pp. 743–767, 2002.
- [48] A. Khalfallah, H. B. H. Salah, and A. Dogui, “Anisotropic parameter identification using inhomogeneous tensile test,” *European Journal of Mechanics, A/Solids*, vol. 21, no. 6, pp. 927–942, 2002.
- [49] R. Hill, “A theory of the yielding and plastic flow of anisotropic metals,” *Proceedings of the Royal Society of A: Mathematical, Physical and Engineering Sciences*, vol. 193, pp. 281–297, 1948.
- [50] K. Mattiasson and M. Sigvant, “An evaluation of some recent yield criteria for industrial simulations of sheet forming processes,” *International Journal of Mechanical Sciences*, vol. 50, no. 4, pp. 774–787, 2008.
- [51] A. Chamekh, H. BelHadjSalah, R. Hambli, and A. Gahbiche, “Inverse identification using the bulge test and artificial neural networks,” *Journal of Materials Processing Technology*, vol. 177, no. 1–3, pp. 307–310, 2006.
- [52] M. Bambach, “Comparison of the identifiability of flow curves from the hydraulic bulge test by membrane theory and inverse analysis,” *Key Engineering Materials*, vol. 473, pp. 360–367, 2011.
- [53] L. C. Reis, P. A. Prates, M. C. Oliveira, A. D. Santos, and J. V. Fernandes, “Inverse identification of the Swift law parameters using the bulge test,” *International Journal of Material Forming*, 2016.
- [54] P.-A. Eggertsen and K. Mattiasson, “On the modelling of the bending-unbending behaviour for accurate springback predictions,” *International Journal of Mechanical Sciences*, vol. 51, no. 7, pp. 547–563, 2009.
- [55] Q. Yin, C. Soyarslan, A. Güner, A. Brosius, and A. E. Tekkaya, “A cyclic twin bridge shear test for the identification of kinematic hardening parameters,” *International Journal of Mechanical Sciences*, vol. 59, no. 1, pp. 31–43, 2012.
- [56] A. F. G. Pereira, P. A. Prates, N. A. Sakharova, M. C. Oliveira, and J. V. Fernandes, “On the identification of kinematic hardening with reverse shear test,” *Engineering with Computers*, vol. 31, no. 4, pp. 681–690, 2015.
- [57] J. Cao and J. Lin, “A study on formulation of objective functions for determining material models,” *International Journal of Mechanical Sciences*, vol. 50, no. 2, pp. 193–204, 2008.
- [58] A. Andrade-Campos, R. De-Carvalho, and R. A. F. Valente, “Novel criteria for determination of material model parameters,” *International Journal of Mechanical Sciences*, vol. 54, no. 1, pp. 294–305, 2012.
- [59] T. Pottier, F. Toussaint, and P. Vacher, “Contribution of heterogeneous strain field measurements and boundary conditions modelling in inverse identification of material parameters,” *European Journal of Mechanics—A/Solids*, vol. 30, no. 3, pp. 373–382, 2011.
- [60] J.-P. Ponthot and J.-P. Kleinermann, “A cascade optimization methodology for automatic parameter identification and shape/process optimization in metal forming simulation,” *Computer Methods in Applied Mechanics and Engineering*, vol. 195, no. 41–43, pp. 5472–5508, 2006.
- [61] M. Meuwissen, *An inverse method for the mechanical characterisation of metals [Ph.D. thesis]*, Technische Universiteit Eindhoven, 1998.

- [62] S. Cooreman, *Identification of the plastic material behaviour through full-field displacement measurements and inverse methods [Ph.D. thesis]*, Vrije Universiteit Brussel, 2008.
- [63] B. Endelt and K. B. Nielsen, "Inverse modeling based on an analytical definition of the Jacobian matrix associated with Hill's 48 yield criterion," in *Proceedings of the 7th Esaform Conference on Material Forming (ESAFORM '04)*, S. Stören, Ed., Trondheim, Norway, April 2004.
- [64] B. Endelt, K. B. Nielsen, and J. Danckert, "Analytic differentiation of Barlat's 2D criteria for inverse modeling," in *Proceedings of the Analytic differentiation of Barlat's 2D criteria for inverse modeling*, vol. 778 of *AIP Conference Proceedings*, pp. 789–794, Detroit, Mich, USA, August 2005.
- [65] D. W. Marquardt, "An algorithm for least-squares estimation of nonlinear parameters," *Journal of the Society for Industrial and Applied Mathematics*, vol. 11, pp. 431–441, 1963.
- [66] P.-A. Eggertsen and K. Mattiasson, "An efficient inverse approach for material hardening parameter identification from a three-point bending test," *Engineering with Computers*, vol. 26, no. 2, pp. 159–170, 2010.
- [67] X.-Q. Li and D.-H. He, "Identification of material parameters from punch stretch test," *Transactions of Nonferrous Metals Society of China*, vol. 23, no. 5, pp. 1435–1441, 2013.
- [68] A. Chamekh, H. Bel Hadj Salah, and R. Hambli, "Inverse technique identification of material parameters using finite element and neural network computation," *International Journal of Advanced Manufacturing Technology*, vol. 44, no. 1-2, pp. 173–179, 2009.
- [69] M. C. Oliveira, J. L. Alves, B. M. Chaparro, and L. F. Menezes, "Study on the influence of work-hardening modeling in springback prediction," *International Journal of Plasticity*, vol. 23, no. 3, pp. 516–543, 2007.
- [70] J. Kajberg and G. Lindkvist, "Characterisation of materials subjected to large strains by inverse modelling based on in-plane displacement fields," *International Journal of Solids and Structures*, vol. 41, no. 13, pp. 3439–3459, 2004.
- [71] L. Robert, V. Velay, N. Decultot, and S. Ramde, "Identification of hardening parameters using finite element models and fullfield measurements: some case studies," *Journal of Strain Analysis for Engineering Design*, vol. 47, no. 1, pp. 3–17, 2012.
- [72] H. Haddadi and S. Belhabib, "Improving the characterization of a hardening law using digital image correlation over an enhanced heterogeneous tensile test," *International Journal of Mechanical Sciences*, vol. 62, no. 1, pp. 47–56, 2012.
- [73] F. Pierron, S. Avril, and V. T. Tran, "Extension of the virtual fields method to elasto-plastic material identification with cyclic loads and kinematic hardening," *International Journal of Solids and Structures*, vol. 47, no. 22-23, pp. 2993–3010, 2010.
- [74] Y. Pannier, S. Avril, R. Rotinat, and F. Pierron, "Identification of elasto-plastic constitutive parameters from statically undetermined tests using the virtual fields method," *Experimental Mechanics*, vol. 46, no. 6, pp. 735–755, 2006.
- [75] J.-H. Kim, F. Barlat, F. Pierron, and M.-G. Lee, "Determination of anisotropic plastic constitutive parameters using the virtual fields method," *Experimental Mechanics*, vol. 54, no. 7, pp. 1189–1204, 2014.
- [76] J. Fu, F. Barlat, and J.-H. Kim, "Parameter identification of the homogeneous anisotropic hardening model using the virtual fields method," *International Journal of Material Forming*, 2015.
- [77] BSI, "Metallic materials—sheet and strip—determination of biaxial stress-strain curve by means of bulge test with optical measuring systems," DIN EN ISO 16808:2014-11 (E), BSI, 2014.
- [78] S. Chatti and N. Hermi, "The effect of non-linear recovery on springback prediction," *Computers and Structures*, vol. 89, no. 13-14, pp. 1367–1377, 2011.
- [79] P. G. Hodge, "A new method of analyzing stresses and strains in work hardening solids," *Journal of Applied Mechanics*, vol. 24, pp. 482–483, 1957.
- [80] M. A. Crisfield, "More plasticity and other material non-linearity-II," in *Nonlinear Finite Element Analysis of Solids and Structures*, vol. 2, pp. 158–164, John Wiley & Sons, Chichester, UK, 2001.
- [81] A. Brosius, Q. Yin, A. Güner, and A. E. Tekkaya, "A new shear test for sheet metal characterization," *Steel Research International*, vol. 82, no. 4, pp. 323–328, 2011.
- [82] T. F. Coleman and Y. Li, "An interior trust region approach for nonlinear minimization subject to bounds," *SIAM Journal on Optimization*, vol. 6, no. 2, pp. 418–445, 1996.

Research Article

Modeling of Flow Stress of 2026 Al Alloy under Hot Compression

Zheng-bing Xiao,^{1,2} Yuan-chun Huang,^{1,3} and Yu Liu³

¹*School of Mechanical and Electrical Engineering, Central South University, Changsha 410083, China*

²*Collaborative Innovation Center of Advanced Nonferrous Structural Materials and Manufacturing, Central South University, Changsha 410083, China*

³*Light Alloy Research Institute, Central South University, Changsha 410012, China*

Correspondence should be addressed to Zheng-bing Xiao; xiaozb@csu.edu.cn

Received 25 February 2016; Accepted 17 July 2016

Academic Editor: Sutasn Thipprakmas

Copyright © 2016 Zheng-bing Xiao et al. This is an open access article distributed under the Creative Commons Attribution License, which permits unrestricted use, distribution, and reproduction in any medium, provided the original work is properly cited.

In order to investigate the workability and to optimize the hot forming parameters for 2026 Al alloy, hot compression tests were performed in the temperature range of 350~450°C with strain rates of 0.01~10 s⁻¹ and 60% deformation degree on a Gleeble-1500 thermosimulation machine. The true stress-strain curves obtained exhibit that the stress increases dramatically at small strains and then moves forward to a steady state, showing dynamic flow softening. Meanwhile, on the basis of Arrhenius equation, a constitutive equation on the flow stress, temperature, and strain rate was proposed. Yet, the values of the predicated stress from the equation and the true stress differ by as much as 50.10%. Given the intricate impact of precipitation of the second phases on the strength of 2026 Al alloy, the introduction of a revised equation with the reinforcement of temperature was carried out, fitting well with the experiment data at peak stresses. What is more, both pictures obtained by scanning electron microscopy (SEM) and transmission electron microscopy (TEM) were compatible with all the inferences.

1. Introduction

Understanding the materials flow behavior during hot deformation is important for materials processing designers, especially for those dealing with metal processes like hot forging, rolling, and extrusion [1–3]. Usually, constitutive equations describing relationships on the strain rate, temperature, and flow stress, which can be used in the finite element simulation, are helpful in selecting the appropriate working parameters for a given metal to process. A great deal of investigation had attempted to set up constitutive equations to predict the flow stress, especially for the frequently used alloys like aluminum alloys, steels, and nickel based super alloys [4–10]. Generally, constitutive models now used can be classified into phenomenological type, physical-based type, and artificial neural network (ANN) type [11]. The Arrhenius equation of phenomenological type was the main one for its simplicity and accuracy [6, 12–16]. Numerous papers have been published based on the equations proposed by Sellars

and Zener [17–19], either the constitutive equations or the modified ones, especially in the hot working of steels, all agreeing well with experiment results, assisting in selecting the hot deformation parameters [12, 20–27].

But, unlike steels, microstructures of aluminum alloys will significantly change due to precipitation in the hot deformation processing, not to mention that those can be strengthened by heat treatment, 2xxx and 7xxx alloys, for example, which usually serve as skins and frames of airplanes. Second phases, like Al₂Cu in 2xxx alloys and MgZn₂ in 7xxx alloys, usually appear in the hot working and heat treatment, which need substantial increase of the stress to continue the hot deformation [15, 28–32]. Prediction of the peak stress for those alloys is hard for their temperature-dependent nature, but the stress-strain relationship, especially the peak stress, is crucial for processing, since it determines the selection of the machines to fulfill the upper compressive stress needed.

As an improved version of 2024 Al alloy, 2026 Al alloy with lower Fe and Si content but minor addition of Zr to

inhibit recrystallization during hot working was established by Alcoa in 1999, satisfying demand for better safety and durability without sacrifice of strength and toughness [33]. As a new alloy of high strength and high damage tolerance, 2026 Al alloy is used as the upholstery skin material for lower aero foil in airplanes like A380 from hot rolling.

Unlike the traditional materials, works about 2026 Al alloy are rare to find, and the most existent investigations on 2026 Al alloy mainly focus on the microstructure evolution during hot processing or the precipitation of the second phases [33, 34]. To the authors' knowledge, there is little information available in the literature about flow behavior of 2026 Al alloy; further study is needed to perform numerical simulation and to select proper process parameters. This paper will put forward and verify a new constitutive equation about the flow behavior of 2026 Al alloy under hot deformation.

2. Experiments

A commercial 2026 Al alloy of chemical composition (wt.%) 1.33Mg-4.20Cu-0.55Mn-0.15Zr-(bal.)Al, with minor elements like Si and Fe below 0.05 and 0.07 (wt.%), respectively, was used in the investigation. Specimens were prepared with diameter of 10 mm and height of 15 mm from the direct cast ingot homogenized for $490^{\circ}\text{C} \times 12\text{ h} + 520^{\circ}\text{C} \times 12\text{ h}$. Friction between the specimens and upsetting dies was minimized by entrapping the lubricant with composition of 75% graphite + 20% machine oil + 5% nitric acid trimethyl benzene grease in a depth of 0.1 mm recessed into both ends of the specimens.

As depicted in Figure 1, the specimens were heated to 480°C at a heating rate of 2°C/s and held for 6 min and then cooled to the deformation temperature at 10°C/s and held for 4 min before test. The hot compression tests were carried out on a Gleeble-1500 thermosimulation machine at four different strain rates (0.01 s^{-1} , 0.1 s^{-1} , 1 s^{-1} , and 10 s^{-1}) and four different temperatures (300°C , 350°C , 400°C , and 450°C), with 60% final reduction in height. After the hot compression, specimens were quenched in water immediately for micrographic observation.

3. Results and Discussion

3.1. True Stress and Strain. The true stress-strain curves obtained from hot compression tests for 2026 Al alloy are shown in Figure 2. For aluminum alloys of high stacking fault energy, dynamic recovery is the main reason for the softening phenomenon [35], which is confirmed by the occurrence of dynamic softening on the curves in this work, for the flow stresses increase monotonically up to an almost steady state (e.g., samples deformed at strain rate of 0.01 s^{-1}). As can be seen from the figures, the strain rate and temperature significantly affect the flow stresses. The true stress level will rise once deformation temperature decreases and strain rate increases.

Under low temperatures, restraint of the number of slip systems reduces the mobility at grain boundaries, thus

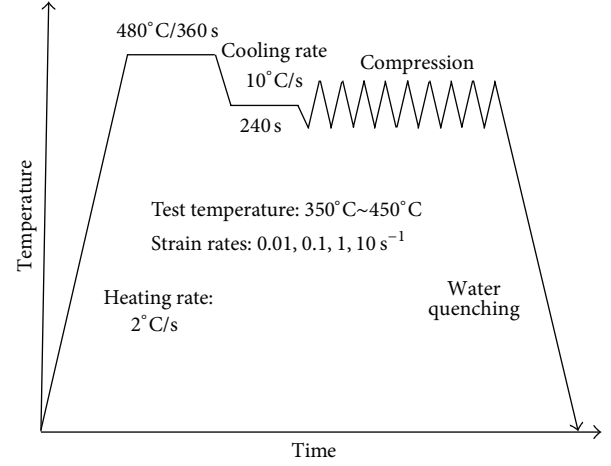


FIGURE 1: Experimental procedure for hot compression tests.

increasing the flow stress. This was approved further by the dislocation walls in Figure 3, for the TEM observation of the sample at $300^{\circ}\text{C}/10\text{ s}^{-1}$, which shows the highest flow stress during compression.

By raising the deformation temperature, dislocation slip, climb, and annihilation correspondingly increase, together with vacancy diffusion rate, resulting in easier activation of dynamic recovery and even dynamic recrystallization to overcome the hardening. Figure 4 shows, for the sample deformed at $0.01\text{ s}^{-1}/450^{\circ}\text{C}$, subgrains formed at grain boundaries, evidence of dynamic recrystallization, which can greatly contribute to the decrease of the flow stress. However, with the increase of strain rate, the time for energy accumulation, dynamic recovery, and recrystallization is shortened, and the true stress would increase.

3.2. Deformation Constitutive Equation. Usually, the relationship regarding flow stress, deformation temperature, and strain rate can be expressed by Arrhenius equation. Zener-Hollomon parameter Z in an exponent-type equation represents the effects of strain rate and temperature on the deformation behaviors. Consequently, Arrhenius equation can be used to connect Z parameter with stress [18, 19]. Hence,

$$Z = \dot{\epsilon} \exp\left(\frac{Q}{RT}\right), \quad (1)$$

$$\dot{\epsilon} = AF(\sigma) \exp\left(-\frac{Q}{RT}\right), \quad (2)$$

where

$$F(\sigma) = \begin{cases} \sigma^{n'} & \alpha\sigma < 0.8 \\ \exp(\beta\sigma) & \alpha\sigma > 1.2 \\ \sinh(\alpha\sigma)^n & \forall \sigma, \end{cases} \quad (3)$$

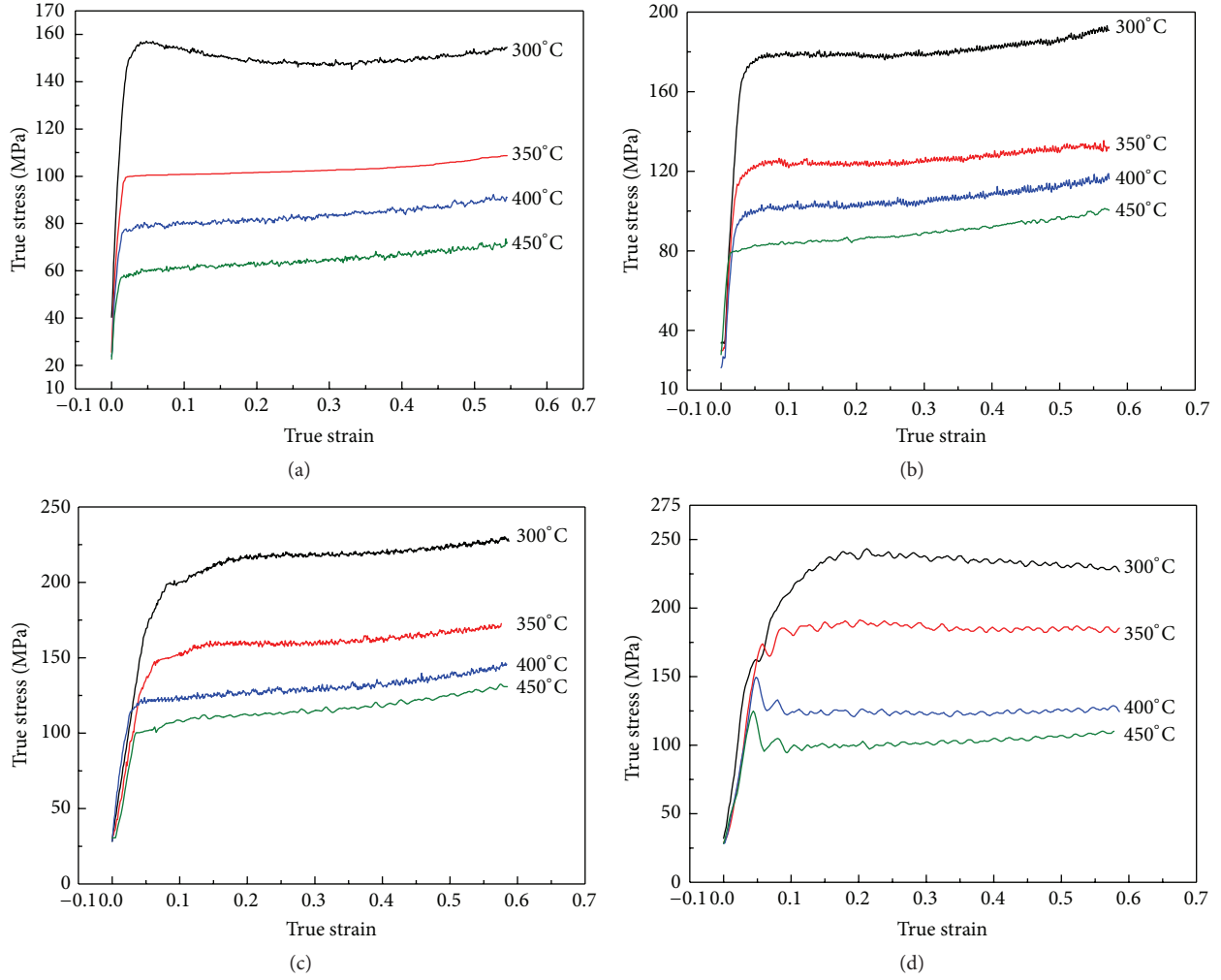


FIGURE 2: Typical true stress-strain curves for 2026 Al alloy under different deformation temperatures with strain rates of (a) 0.01 s^{-1} ; (b) 0.1 s^{-1} ; (c) 1 s^{-1} ; and (d) 10 s^{-1} .

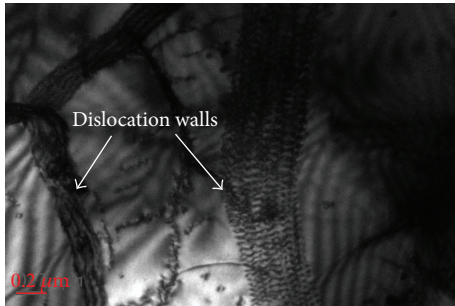


FIGURE 3: TEM micrograph of the sample deformed at temperature of 300°C with the strain rate of 10 s^{-1} with dislocation walls.

in which $\dot{\epsilon}$ is the strain rate (s^{-1}), Q is the activation energy of hot deformation (kJmol^{-1}), R is the universal gas constant ($8.31 \text{ Jmol}^{-1}\text{K}^{-1}$), T is the absolute temperature (K), and σ is the flow stress (MPa) for a given strain, while A , α , and n , n' are the material constants, $\alpha = \beta/n'$.

Equations (4) and (4) are the substitution of the power law and exponential law of $F(\sigma)$ into (1) for the low-stress ($\alpha\sigma < 0.8$) and high-stress level ($\alpha\sigma > 1.2$), respectively:

$$\dot{\epsilon} = B\sigma^{n'}, \quad (4)$$

$$\dot{\epsilon} = B' \exp(\beta\sigma) \frac{1}{2}, \quad (5)$$

where B and B' are the material constants. To find out the material constants in the above equations, deformation strain of peak stress is used here as an example.

Equations (6) and (6) are the logarithm form of (4) and (4), respectively:

$$\ln(\sigma) = \frac{1}{n'} \ln(\dot{\epsilon}) - \frac{1}{n'} \ln(B), \quad (6)$$

$$\sigma = \frac{1}{\beta} \ln(\dot{\epsilon}) - \frac{1}{\beta} \ln(B'). \quad (7)$$

Substituting the values of the peak stress and corresponding strain rate at different deformation temperatures into (6)

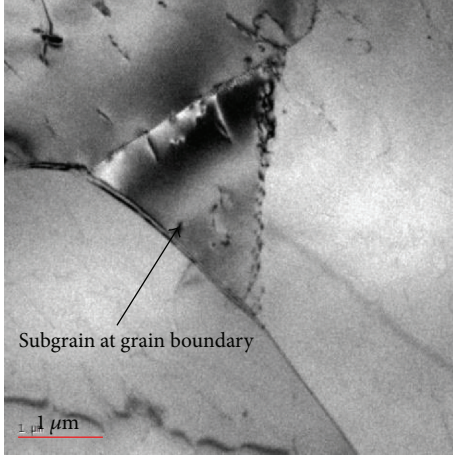


FIGURE 4: TEM micrograph of the sample deformed at temperature of 450°C with the strain rate of 0.01 s⁻¹.

and (6) can obtain the relationship regarding the stress and strain rate (in logarithm form) shown in Figure 5.

As can be seen in Figure 5, a group of straight lines approximated is close to parallel. The slopes of these lines have similar values and values of n' and β at different deformation temperatures can be derived by linear fitting method. As $\alpha = \beta/n'$, each corresponding value of α can be calculated. By average, the mean value of α is 8.0128×10^{-3} .

Equation (1) can be expressed as follows, fit for all the stress level σ :

$$\dot{\epsilon} = A [\sinh(\alpha\sigma)]^n \exp\left(-\frac{Q}{RT}\right). \quad (8)$$

Taking the logarithm of (8) for both sides gives

$$\ln [\sinh(\alpha\sigma)] = \frac{\ln \dot{\epsilon}}{n} + \frac{Q}{nRT} - \frac{\ln A}{n}. \quad (9)$$

Substituting the peak stress and relevant strain rate for all the tested temperatures into (9) gives the relationship shown in Figure 6. It is not hard to obtain the value of n , 9.343.

For a fixed strain rate, derivative of (8) gives

$$Q = Rn \frac{d \{\ln [\sinh(\alpha\sigma)]\}}{d(1/T)}. \quad (10)$$

According to (10), $\ln [\sinh(\alpha\sigma)]$ can be regarded as a function of $1/T$, shown in Figure 7, and the activation energy can be computed as 229.546 kJ/mol by averaging the values of Q at four different strain rates.

On the basis of the value of n and Q known, it is easy to get the value of A , $5.17 \times 10^{22} \text{ s}^{-1}$, $9.53 \times 10^{22} \text{ s}^{-1}$, $8.3 \times 10^{22} \text{ s}^{-1}$, and $3.63 \times 10^{22} \text{ s}^{-1}$ for 300°C, 350°C, 400°C, and 450°C, respectively.

Then, (8) can be expressed below by substituting the values obtained above:

$$\dot{\epsilon} = A \left[\sinh \left(8.0128 \times 10^{-3} \sigma \right) \right]^{9.343} \cdot \exp \left(\frac{-2.29546 \times 10^5}{RT} \right). \quad (11)$$

Finally, Zener-Hollomon parameter Z in (1) can be represented as follows:

$$Z = \dot{\epsilon} \exp \left(\frac{2.29546 \times 10^5}{RT} \right) = A \left[\sinh \left(8.0128 \times 10^{-3} \sigma \right) \right]^{9.343}. \quad (12)$$

According to (8) and (1), relationships between the flow stress σ and Zener-Hollomon parameter Z can be described below:

$$\sigma = \frac{1}{\alpha} \ln \left\{ \left(\frac{Z}{A} \right)^{1/n} + \left[\left(\frac{Z}{A} \right)^{2/n} + 1 \right]^{1/2} \right\}. \quad (13)$$

Or

$$\sigma = 124.8 \ln \left\{ \left(\frac{Z}{A} \right)^{1/9.343} + \left[\left(\frac{Z}{A} \right)^{2/9.343} + 1 \right]^{1/2} \right\}. \quad (14)$$

Depending on the deformation temperature, the constant A in (11) to (14) is $5.17 \times 10^{22} \text{ s}^{-1}$, $9.53 \times 10^{22} \text{ s}^{-1}$, $8.3 \times 10^{22} \text{ s}^{-1}$, and $3.63 \times 10^{22} \text{ s}^{-1}$ for 300°C, 350°C, 400°C, and 450°C, respectively.

3.3. Modification of Zener-Hollomon Parameter. The above-developed constitutive equations for 2026 Al alloy at peak stress state were verified by comparison of the values from experiments and constitutive equation; differences between them are shown in Table 1. In the table, error is defined as

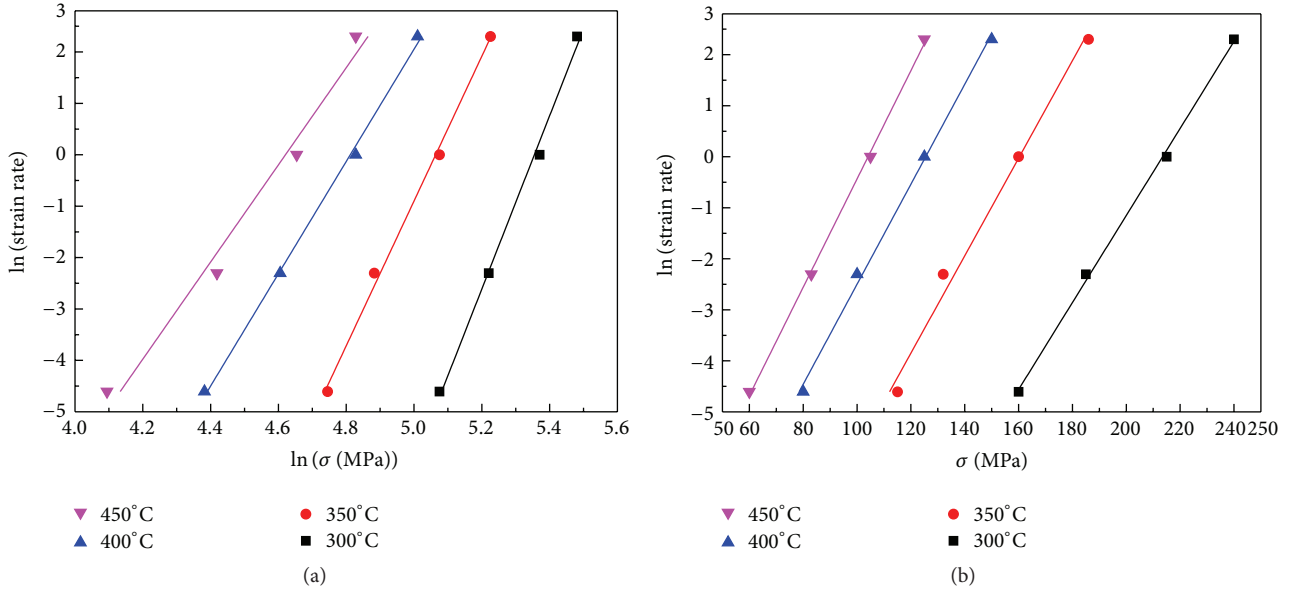
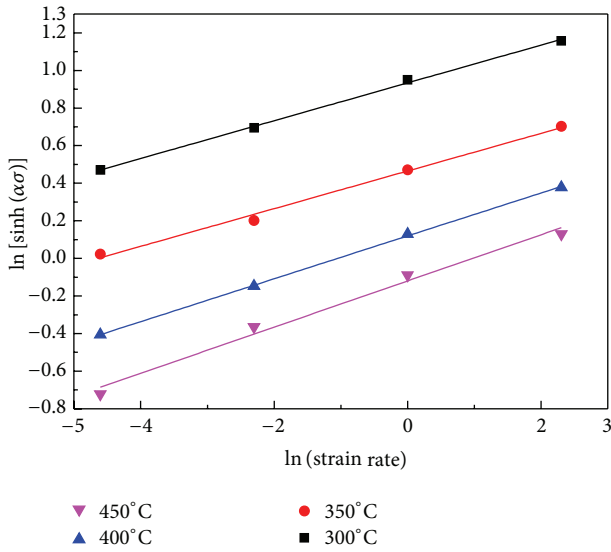
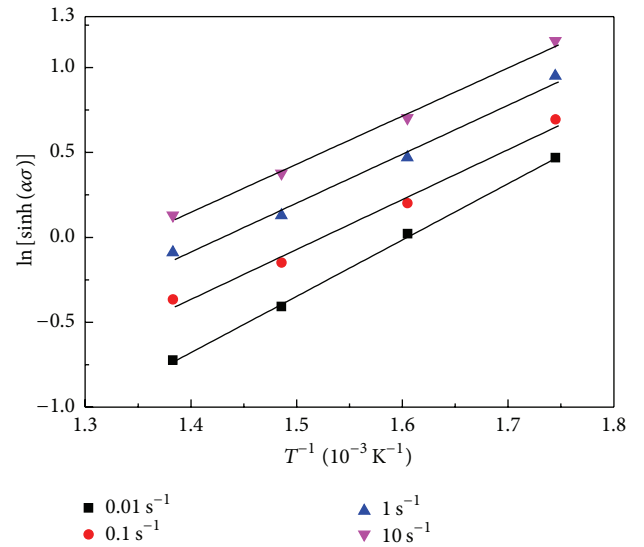
$$\text{Error} = \frac{|\sigma_c - \sigma_m|}{\sigma_m} \times 100\%. \quad (15)$$

σ_c is the stress calculated by the constitutive equation, and σ_m is the peak stress measured by experiments.

Apparently, errors between the experiment and predicated results range from 9.86% to 50.10%, indicating the need to modify the constitutive equation.

Usually, four different stages, namely, work hardening stage (stage 1), stable stage (stage 2), softening stage (stage 3), and steady stage (stage 4), show up on the true strain-true stress curves of typical steels, which can be explained well from the viewpoint of dynamic recovery and dynamic recrystallization under hot deformation [36, 37]. However, for almost all of the Al alloys, precipitation of the second phases inevitably occurs in the hot deformation procedure; 2026 Al alloy is no exception. From Figure 8, the SEM and TEM microstructures of the sample deformed at 350°C with the strain rate of 1 s^{-1} and the final strain of 0.6; the matrix was occupied by numerous tiny white particles (most of them are Al_2Cu), a combining effect of temperature and strain whose influence on flow stress cannot be neglected.

Theoretically, by hindering recrystallization or being coherent with α -Al, precipitation can enhance the material strength to some degree, reflected by the rise of the true stress level on the true stress-true strain curve [33, 34]. Typically speaking, precipitation itself is a complicated factor whose impact on the true stress is relevant to temperature. Therefore,

FIGURE 5: Relationships between strain rate and peak stresses: (a) $\ln \dot{\epsilon}$ and $\ln \sigma$; (b) $\ln \dot{\epsilon}$ and σ .FIGURE 6: Relationship between $\ln[\sinh(\alpha\sigma)]$ and $\ln \dot{\epsilon}$.FIGURE 7: Relationship between $\ln[\sinh(\alpha\sigma)]$ and temperature.

the influence of temperature on the flow stresses should be enforced here for the nature of 2026 Al alloy.

Through numerous repeated calculations and validation, it is found that, to make the Z parameter better conform to the real, (1) should multiply with $\exp(22.93975X - 135.508)$. So, the revised Z' parameter can be expressed as

$$Z' = \exp(22.93975X - 135.508) \dot{\epsilon} \exp\left(\frac{Q}{RT}\right), \quad (16)$$

where factor X represents the deformation temperature in $^{\circ}\text{C}$; it represents the influences of the temperature on the precipitation behavior of the alloy.

Therefore, the flow stress constitutive equation expressed as (13) can be renewed as

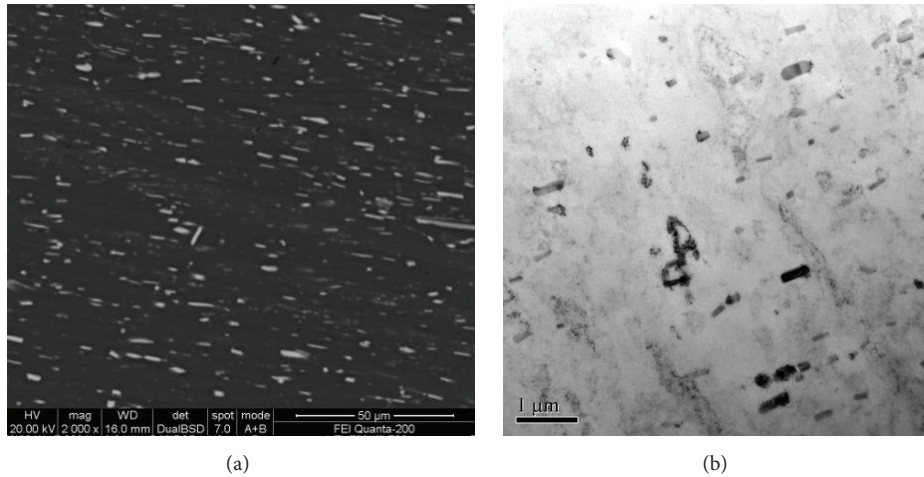
$$\sigma = \frac{1}{\alpha} \ln \left\{ \left(\frac{Z'}{A} \right)^{1/n} + \left[\left(\frac{Z'}{A} \right)^{2/n} + 1 \right]^{1/2} \right\}. \quad (17)$$

Parameters of α , n , and A in the equation are not changed as before, while Z is the modified one from (16).

3.4. Verification of the Revised Constitutive Equation. Table 2 shows the comparisons between the peak stresses calculated from the revised constitutive equation and the experiment data.

TABLE 1: Comparisons of the predicated (σ_p) and measured (σ_E) peak stress (unit: MPa) before the modification of Z parameter.

Strain rate (s^{-1})	Temperature ($^{\circ}C$)	σ_E	σ_p	Error (%)	Error analysis	
					Mean (%)	Standard deviation (%)
0.01	300	160	239.18	49.49	29.20	19.42
	350	115	126.34	9.86		
	400	80	67.53	15.58		
	450	72	41.85	41.87		
0.1	300	191	277.79	45.44	27.49	15.24
	350	132	150.90	14.32		
	400	100	84.64	15.36		
	450	83	54.09	34.83		
1	300	228	318.32	39.61	25.35	13.74
	350	160	177.83	11.14		
	400	125	104.57	16.34		
	450	105	68.99	34.30		
10	300	240	360.24	50.10	26.83	17.67
	350	186	206.67	11.11		
	400	150	127.03	15.31		
	450	125	86.51	30.79		

FIGURE 8: Microstructure after hot deformation at true strain of 0.6 with the deformation temperature of $350^{\circ}C$ and strain rate of $1 s^{-1}$: (a) backscattered electron image and (b) TEM micrograph.

As observed from the values, agreement between the calculated and measured values is good, and the maximum relative error is only 5.87%. The results indicated that the modified Z parameter can give a good estimate of the peak stresses for 2026 Al alloy under different hot compression temperature and strain rate and can be used in guidance of the hot processing of 2026 Al alloy.

4. Conclusions

In this study, the effects of deformation parameters on the true stress-strain behavior of 2026 Al alloy were investigated. According to the experiment data, a constitutive equation incorporating the effects of strain rates and temperatures is obtained, while the errors between the experiment and

predicated results range from 9.86% to 50.10%. So a revised constitutive equation is derived by compensation of temperature considering the impact of the second phase on the true stress; a good agreement between the predicated and the experiment results indicated that the revised constitutive equation can give an accurate prediction of the peak stress for 2026 Al alloy and can be used in the hot processing of the 2026 Al alloy. In addition, pictures about the microstructures were obtained using scanning electron microscopy (SEM) and transmission electron microscopy (TEM) for verification and assistance.

Competing Interests

The authors declare that they have no competing interests.

TABLE 2: Comparisons of the predicated (σ_p) and measured (σ_E) peak stress (unit: MPa) after the modification of Z parameter.

Strain rate (s^{-1})	Temperature ($^{\circ}C$)	σ_E	σ_p	Error (%)	Error analysis	
					Mean (%)	Standard deviation (%)
0.01	300	160	169.37	5.86	3.03	2.4
	350	115	115.28	0.24		
	400	80	81.72	2.15		
	450	72	69.22	3.87		
0.1	300	191	202.22	5.87	4.14	2.03
	350	132	138.54	4.96		
	400	100	101.21	1.21		
	450	83	86.76	4.53		
1	300	228	238.21	4.48	2.53	1.44
	350	160	164.37	2.73		
	400	125	123.29	1.37		
	450	105	106.60	1.52		
10	300	240	246.77	2.82	2.62	0.72
	350	186	192.33	3.40		
	400	150	147.50	1.66		
	450	125	128.22	2.58		

Acknowledgments

This work was supported by the National Program on Key Basic Research Project of China (no. 2012CB619504 and no. 2014CB046702). The authors thank Lin Y. C. and his coworkers in the School of Mechanical and Electrical Engineering, Central South University, Changsha, for their kind and helpful theoretical guidance and discussion.

References

- [1] A. Łukaszek-Solek and J. Krawczyk, "The analysis of the hot deformation behaviour of the Ti-3Al-8V-6Cr-4Zr-4Mo alloy, using processing maps, a map of microstructure and of hardness," *Materials & Design*, vol. 65, pp. 165–173, 2015.
- [2] T.-D. Kil, J.-M. Lee, and Y.-H. Moon, "Quantitative formability estimation of ring rolling process by using deformation processing map," *Journal of Materials Processing Technology*, vol. 220, pp. 224–230, 2015.
- [3] S. Saadatkia, H. Mirzadeh, and J.-M. Cabrera, "Hot deformation behavior, dynamic recrystallization, and physically-based constitutive modeling of plain carbon steels," *Materials Science and Engineering: A*, vol. 636, pp. 196–202, 2015.
- [4] H. Mirzadeh, J. M. Cabrera, and A. Najafizadeh, "Constitutive relationships for hot deformation of austenite," *Acta Materialia*, vol. 59, no. 16, pp. 6441–6448, 2011.
- [5] M. El Mehtedi, F. Gabrielli, and S. Spigarelli, "Hot workability in process modeling of a bearing steel by using combined constitutive equations and dynamic material model," *Materials & Design*, vol. 53, pp. 398–404, 2014.
- [6] M. El Mehtedi, F. Musharavati, and S. Spigarelli, "Modelling of the flow behaviour of wrought aluminium alloys at elevated temperatures by a new constitutive equation," *Materials and Design*, vol. 54, pp. 869–873, 2014.
- [7] T.-H. Pham, J. J. Kim, and S.-E. Kim, "Estimating constitutive equation of structural steel using indentation," *International Journal of Mechanical Sciences*, vol. 90, pp. 151–161, 2015.
- [8] C.-L. Gan, K.-H. Zheng, W.-J. Qi, and M.-J. Wang, "Constitutive equations for high temperature flow stress prediction of 6063 Al alloy considering compensation of strain," *Transactions of Nonferrous Metals Society of China (English Edition)*, vol. 24, no. 11, Article ID 63492, pp. 3486–3491, 2014.
- [9] Y. Liu, Z. Yao, Y. Ning et al., "The flow behavior and constitutive equation in isothermal compression of FGH4096-GH4133B dual alloy," *Materials and Design*, vol. 63, pp. 829–837, 2014.
- [10] X. Peng, H. Guo, Z. Shi, C. Qin, and Z. Zhao, "Constitutive equations for high temperature flow stress of TC4-DT alloy incorporating strain, strain rate and temperature," *Materials and Design*, vol. 50, pp. 198–206, 2013.
- [11] Y. C. Lin and X.-M. Chen, "A critical review of experimental results and constitutive descriptions for metals and alloys in hot working," *Materials & Design*, vol. 32, no. 4, pp. 1733–1759, 2011.
- [12] D. Samantaray, C. Phaniraj, S. Mandal, and A. K. Bhaduri, "Strain dependent rate equation to predict elevated temperature flow behavior of modified 9Cr-1Mo (P91) steel," *Materials Science and Engineering: A*, vol. 528, no. 3, pp. 1071–1077, 2011.
- [13] N. Haghdadi, A. Zarei-Hanzaki, and H. R. Abedi, "The flow behavior modeling of cast A356 aluminum alloy at elevated temperatures considering the effect of strain," *Materials Science and Engineering A*, vol. 535, pp. 252–257, 2012.
- [14] B.-J. Lv, J. Peng, D.-W. Shi, A.-T. Tang, and F.-S. Pan, "Constitutive modeling of dynamic recrystallization kinetics and processing maps of Mg-2.0Zn-0.3Zr alloy based on true stress-strain curves," *Materials Science and Engineering A*, vol. 560, pp. 727–733, 2013.
- [15] M. Zhou, Y. C. Lin, J. Deng, and Y.-Q. Jiang, "Hot tensile deformation behaviors and constitutive model of an Al-Zn-Mg-Cu alloy," *Materials & Design*, vol. 59, pp. 141–150, 2014.
- [16] H. Mirzadeh, "Constitutive modeling and prediction of hot deformation flow stress under dynamic recrystallization conditions," *Mechanics of Materials*, vol. 85, pp. 66–79, 2015.
- [17] C. M. Sellars, "The kinetics of softening processes during hot working of austenite," *Czechoslovak Journal of Physics B*, vol. 35, no. 3, pp. 239–248, 1985.

- [18] C. M. Sellars and W. J. McTegart, "On the mechanism of hot deformation," *Acta Metallurgica*, vol. 14, no. 9, pp. 1136–1138, 1966.
- [19] C. Zener and J. H. Hollomon, "Effect of strain rate upon plastic flow of steel," *Journal of Applied Physics*, vol. 15, no. 1, pp. 22–32, 1944.
- [20] G. Z. Quan, Y. Tong, G. Luo, and J. Zhou, "A characterization for the flow behavior of 42CrMo steel," *Computational Materials Science*, vol. 50, no. 1, pp. 167–171, 2010.
- [21] L.-Z. Wu, X.-S. Li, J. Chen, H.-B. Zhang, and Z.-S. Cui, "Predicting critical conditions and stress-strain curves for dynamic recrystallization in SPHC steel," *Journal of Iron and Steel Research International*, vol. 17, no. 7, pp. 51–57, 2010.
- [22] I. Mejia, A. Bedolla-Jacuinde, C. Maldonado, and J. M. Cabrera, "Determination of the critical conditions for the initiation of dynamic recrystallization in boron microalloyed steels," *Materials Science and Engineering: A*, vol. 528, no. 12, pp. 4133–4140, 2011.
- [23] N. Park, A. Shibata, D. Terada, and N. Tsuji, "Flow stress analysis for determining the critical condition of dynamic ferrite transformation in 6Ni–0.1C steel," *Acta Materialia*, vol. 61, no. 1, pp. 163–173, 2013.
- [24] Y. C. Lin, M.-S. Chen, and J. Zhong, "Constitutive modeling for elevated temperature flow behavior of 42CrMo steel," *Computational Materials Science*, vol. 42, no. 3, pp. 470–477, 2008.
- [25] Y. C. Lin, M.-S. Chen, and J. Zhong, "Microstructural evolution in 42CrMo steel during compression at elevated temperatures," *Materials Letters*, vol. 62, no. 14, pp. 2136–2139, 2008.
- [26] Y.-C. Lin, M.-S. Chen, and J. Zhang, "Modeling of flow stress of 42CrMo steel under hot compression," *Materials Science and Engineering: A*, vol. 499, no. 1–2, pp. 88–92, 2009.
- [27] Y. C. Lin, M.-S. Chen, and J. Zhong, "Numerical simulation for stress/strain distribution and microstructural evolution in 42CrMo steel during hot upsetting process," *Computational Materials Science*, vol. 43, no. 4, pp. 1117–1122, 2008.
- [28] M. I. A. E. Aal, "Influence of the pre-homogenization treatment on the microstructure evolution and the mechanical properties of Al–Cu alloys processed by ECAP," *Materials Science and Engineering: A*, vol. 528, no. 22–23, pp. 6946–6957, 2011.
- [29] J.-H. Jang, D.-G. Nam, Y.-H. Park, and I.-M. Park, "Effect of solution treatment and artificial aging on microstructure and mechanical properties of Al–Cu alloy," *Transactions of Nonferrous Metals Society of China*, vol. 23, no. 3, pp. 631–635, 2013.
- [30] C. Giummarra, G. H. Bray, and D. J. Duquette, "Fretting fatigue in 2XXX series aerospace aluminium alloys," *Tribology International*, vol. 39, no. 10, pp. 1206–1212, 2006.
- [31] Y. Chen, M. Weyland, and C. R. Hutchinson, "The effect of interrupted aging on the yield strength and uniform elongation of precipitation-hardened Al alloys," *Acta Materialia*, vol. 61, no. 15, pp. 5877–5894, 2013.
- [32] H. C. Fang, H. Chao, and K. H. Chen, "Effect of Zr, Er and Cr additions on microstructures and properties of Al–Zn–Mg–Cu alloys," *Materials Science and Engineering A*, vol. 610, pp. 10–16, 2014.
- [33] D. F. Lam, C. C. Menzemer, and T. S. Srivatsan, "A study to evaluate and understand the response of aluminum alloy 2026 subjected to tensile deformation," *Materials & Design*, vol. 31, no. 1, pp. 166–175, 2010.
- [34] X. Huang, H. Zhang, Y. Han, W. Wu, and J. Chen, "Hot deformation behavior of 2026 aluminum alloy during compression at elevated temperature," *Materials Science and Engineering A*, vol. 527, no. 3, pp. 485–490, 2010.
- [35] F. J. Humphreys and M. Hatherly, "The deformed state," in *Recrystallization and Related Annealing Phenomena*, F. J. H. Hatherly, Ed., chapter 2, p. 11, Elsevier, New York, NY, USA, 2004.
- [36] Z. Q. Sheng and R. Shivpuri, "Modeling flow stress of magnesium alloys at elevated temperature," *Materials Science and Engineering A*, vol. 419, no. 1–2, pp. 202–208, 2006.
- [37] R. E. Smallman and R. J. BiShop, "Chapter 7—mechanical behaviour of materials," in *Modern Physical Metallurgy and Materials Engineering*, pp. 197–258, Butterworth-Heinemann, Boston, Mass, USA, 6th edition, 1999.